CHAPTER 4

Growth and Properties of Nanostructured Films Prepared by Cluster Deposition

Pablo Jensen, Laurent Bardotti, Jean-Louis Barrat, Nicolas Combe, Véronique Dupuis, Mathieu Jamet, Patrice Mélinon, Brigitte Prével, Juliette Tuaillon-Combes, Alain Perez

Département de Physique des Matériaux, Université Claude Bernard Lyon-1, 69622 Villeurbanne Cédex, France

CONTENTS

Nanoclusters and Nanocrystals
Edited by H. S. Nalwa
ISBN: 1-58883-017-9 / $35.00

1. INTRODUCTION

The physics and chemistry of nanoscale systems have advanced significantly over the last 10 years and there are attractive prospects for translating these original scientific developments into a new generation of high technology materials and processes [1–7]. Since nanotechnology is a generic technology, it cuts across several industrial sectors, from chemistry to electronics, from sensors to biotechnologies and advanced nanostructured materials. In this general context, the design and fabrication of nanostructured systems and the study of their specific properties are playing increasingly important roles. More generally, growth of new materials with tailored properties is one of the most active research directions for physicists. As pointed out by Silvan Schweber in his brilliant analysis of the evolution of physics after World War II: "An important transformation has taken place in physics: As had previously happened in chemistry, an ever larger fraction of the efforts in the field [is] being devoted to the study of novelty [creation of new structures, new objects and new phenomena] rather than to the elucidation of fundamental laws and interactions [. . .]. Condensed matter physics has indeed become the study of systems that have never before existed" [8].

There are different ways to build up nanostructured systems [7]: atomic deposition [9], mechanical milling [10], chemical methods [6, 11], gas-aggregation techniques [4, 12–14]. Each of these techniques has its own advantages, but, as happens with atomic deposition techniques, the requisites of *control* (in terms of characterization and flexibility) and *efficiency* (in terms of quantity of matter obtained per second) are generally incompatible. For example, chemical syntheses generally offer the unique advantage of preparing large quantities of nanostructured matter while the physical ones mentioned above (except the mechanical synthesis) are very often limited to the preparation of thin films. However, these last methods still seem promising in terms of specificity of the nanoparticle structures and properties related to their nonequilibrium preparation conditions generally characterized by relatively high cooling rates. As *physicists* wishing to understand the details of the processes involved in the building of these nanostructures, we will focus in this chapter on a carefully *controlled* method: low energy cluster deposition [13]. Clusters are large "molecules" containing typically from a few tens to a few thousand atoms, and they have been studied for their specific physical properties (mostly due to their large surface to volume ratio) which are *size dependent* and different from both the constituting atoms and the bulk material [3, 15–18]. By depositing *preformed* clusters on a substrate, one can build nanostructures of two types: in the submonolayer range, separated (and hopefully ordered) nanoislands, and for higher thicknesses, thin films or cluster assembled materials. The main advantage of the cluster deposition technique is that one can carefully control the building block (i.e., the cluster) and characterize the growth mechanisms. By changing the *size* of the incident clusters one can change the growth mechanisms [19, 20] and the characteristics of the materials. For example, it has been shown that by changing the mean size of the incident carbon clusters, one can modify the properties of the carbon film, from graphitic to diamondlike [21].

This chapter is organized as follows. First, we present briefly the interest of nanostructures, both in the domain of nanoislands arranged on a substrate and as nanostructured, continuous films. We also review the different strategies employed to deposit *clusters* on a substrate: by accelerating them or by achieving their soft-landing. The scope of this section is to convince the reader that cluster deposition is a promising technique for nanostructure growth in a variety of domains and therefore deserves a careful study. In Section 3, models for cluster deposition are introduced. These models can also be useful for *atomic* deposition in some simple cases, namely when aggregation is irreversible. The models are adapted here to the physics of *cluster* deposition. In this case, reevaporation from the substrate can be important (as opposed to the usual conditions of molecular beam epitaxy), cluster–cluster aggregation is always irreversible (as opposed to the possibility of bond breaking for atoms [22]), and particle–particle *coalescence* is possible. After a brief presentation of kinetic Monte Carlo simulations, we show how the submonolayer regime can be studied in a wide variety of experimental situations: complete condensation, growth with reevaporation, nucleation on defects, formation of two- and three-dimensional islands. . . . Since we want these models to be useful for experimentalists, Section 5 is entirely devoted to the presentation of a strategy on how to analyze experimental data and extract microscopic parameters such as diffusion and evaporation rates. We remind the reader that a simple software simulating all these situations is available at no cost on simple request to the author. Section 6 analyzes in detail several experiments of cluster deposition. These studies serve as examples of the recipes given in Section 5 to analyze the data and also to demonstrate that clusters can have surprisingly large mobilities (comparable to atomic mobilities) on some substrates. A first interpretation of these intriguing results at the atomic level is given in Section 7, where the kinetics of cluster–cluster coalescence is also studied. The main results of this section are

that high cluster mobilities can be achieved provided the cluster does not find an epitaxial arrangement on the substrate and that cluster–cluster coalescence can be much slower than predicted by macroscopic theories. Finally, Section 8 gives some examples of the original properties which can be obtained with this original technique. We will present the original electronic structures and properties of covalent semiconducting nanostructured systems based on pure silicon or mixed silicon–carbon cagelike clusters (fullerenes and heterofullerenes). Also, nanostructured systems from metallic clusters for applications to magnetic (i.e., Co or $SmCo_5$ clusters) or optical nanostructures (i.e., Ag, Au, Au_xAg_{1-x} clusters) are described.

A note on terminology: The structures formed on the surface by aggregation of the clusters are called islands. This is to avoid possible confusion with the terms usually employed for atomic deposition where the clusters are the islands formed by aggregation of atoms on the surface. Here, the clusters are *preformed* in the gas phase *before* deposition. We use *coverage* for the actual portion of the surface covered by the islands and *thickness* for the total amount of matter deposited on the surface (see also Table 1).

Table 1. Principal symbols and terms used in this chapter. The natural length unit in the model corresponds to the mean diameter of an incident cluster or to the distance between jump sites for atoms.

Symbols and terms	Units, remarks
Particle	adatom or incident cluster
Island	structure formed on the surface by aggregation of particles
ML	monolayer: the amount of matter needed to cover uniformly the substrate with one layer of particles
F	impinging flux expressed in monolayers (or particles per site) per second
Site	area occupied by a cluster on the surface site = $\pi d^2/4$ (cluster deposition) or by an atomic site (atomic case)
τ	diffusion time: mean time needed for a particle to make a jump between two sites (in seconds)
τ_e	evaporation time: mean time before a monomer evaporates from the surface
n	number of atoms of the cluster
d	cluster diameter in nm, $d = d_0 n^{1/3}$ where d_0 depends on the element
ϕ	normalized flux ($\phi = F\tau$) expressed in clusters per site
D	diffusion coefficient expressed in $cm^2\,s^{-1}$ ($D =$ site/4τ)
e	mean thickness of the film, $e = Ft$ where t is the deposition time
θ	coverage; fraction of the substrate covered by the particles
N_t	island density on the surface, expressed per site
N_{sat}	saturation (maximum) island density on the surface, expressed per site
C_{sat}	condensation coefficient (ratio of matter actually present on the substrate over the thickness) at saturation
ρ	particle density on the surface, expressed per site
l_S	mean distance between two islands at saturation $l_S \sim N_{\text{sat}}^{-1/2}$
X_S	mean diffusion length on the substrate before desorption: $X_S = \sqrt{D\tau_e}$
ℓ_{CC}	the island–island distance at saturation when there is no evaporation

2. DIFFERENT TYPES OF NANOSTRUCTURES

There are two distinct (though related) domains where nanostructures can be interesting for applications. The first stems from the desire for miniaturization of electronic devices. Specifically, one would like to grow organized nanometer size islands with specific electronic properties. As a consequence, an impressive quantity of deposition techniques has been developed to grow carefully controlled thin films and nanostructures from atomic deposition [9]. While most of these techniques are complex and keyed to specific applications, molecular beam epitaxy (MBE) [28] has received much attention from the physicists [29], mainly because of its (relative) simplicity. The second subfield is that of nanostructured materials [7], as thin or thick films, which show (mechanical, catalytic, optical) properties different from their microcrystalline counterparts [4, 5, 11, 30, 31].

We will now briefly review the two subfields since cluster deposition can be used to build both types of nanostructures. Moreover, some of the physical processes studied below (such as cluster–cluster coalescence) are of interest for both types of structure.

2.1. Organized Nanoislands

There has been a growing interest for the fabrication of organized islands of nanometer dimensions. One of the reasons is the obvious advantage of miniaturizing the electronic devices both for device speed and density on a chip (for a simple and enjoyable introduction to the progressive miniaturization of electronics devices, see [32]). But it should be noted that at these scales, shrinking the size of the devices does also change their properties, due to quantun confinement effects. Specifically, semiconductor islands smaller than the Bohr diameter of the bulk material (from several nm to several tens of nm) show interesting properties: as their size decreases, their effective bandgap increases. The possibility to tailor the electronic properties of a given material by playing on its size has generated a high level of interest in the field of these *quantum dots* [33]. But quantum dots are not the only driving force for obtaining organized nanoislands. Isolated nanoparticles are also interesting as model catalysts (see [34, 35] and Chapter 12 of [7]). Clearly, using small particles increases the specific catalytic area for a given volume. More interesting, particles smaller than 4–5 nm in diameter might show specific catalytic properties, different from the bulk [35, 36], although the precise

mechanisms are not always well identified (Chapter 12 of [7]). One possibility is the increase, for small particle sizes, of the proportion of low coordination atoms (corners, kinks) whose electronic (and therefore catalytic) properties are expected to be different from bulk atoms. For even smaller particles (1–2 nm), the interaction with the substrate can significantly alter their electronic properties [37]. Recently, there have been attempts at *organizing* the isolated islands to test the consequences on the catalytic properties [38]. Obtaining isolated clusters on a surface can also be interesting to study their properties. For example, Schaefer et al. [39] have obtained isolated gold clusters onto a variety of substrates to investigate the elastic properties of *single* nanoparticles by atomic force microscopy (AFM).

Let me now briefly turn to the possible ways of obtaining such organized nanoislands. Deposition of atoms on carefully controlled substrates is the main technique used presently by physicists to try to obtain a periodic array of nanometer islands of well-defined sizes. A striking example of organized nanoislands is given in [40]. The triangular islands have been grown on the dislocation network formed by the second Ag atomic layer on Pt(111). Beautiful as these triangles are, they have to be formed by nucleation and growth on the substrate, and therefore the process is highly dependent on the interaction of the adatoms with the substrate (energy barriers for diffusion, possibility of exchange of adatoms and substrate atoms, ...). This drastically limits the range of possible materials that can be grown by this method. However, the growth of strained islands by heteroepitaxy is under active study, since stress is a force which can lead to order, and even a tunable order, as observed for example in the system PbSe/$Pb_{1-x}Eu_xTe$ [41] (see [42, 43] for further details on stress).

In this chapter, we will focus on an alternative approach to form nanoislands on substrates: instead of growing them by atom–atom aggregation *on* the substrate, a process which dramatically depends on the idiosyncrasies of the substrate and its interaction with the deposited atoms, one can prepare the islands (as free clusters) *before* deposition and then deposit them. It should be noted that the cluster structure can be extensively characterized *prior to* deposition by several in-flight techniques such as time-of-flight mass spectrometry, photoionization, or fragmentation [44]. Moreover, the properties of these building blocks can be adjusted by changing their *size*, which also affects the growth mechanisms and therefore the film morphology [19, 20]. A clear example of the possibility to change the film morphology by varying only the mean cluster size was given a few years ago by Fuchs et al. [19] and this study has been extended recently by Brechignac's group for larger cluster sizes [20]. Figure 1 shows an example of how thin film morphology can be changed by changing the mean cluster size. There are several additional interests for depositing clusters. First, these can be grown in extreme nonequilibrium conditions, especially with the laser vaporization technique, which allows one to obtain metastable structures or alloys. It is true that no islands grown on a substrate are generally in equilibrium, but the quenching rate is very high in a beam, and the method is more flexible since one avoids the effects of nucleation and growth on a specific substrate. For example, PdPt alloy clusters—which are known to have interesting catalytic properties—can be prepared with a precise composition (corresponding to the composition of the target rod used in the cluster source;) and variable size and then deposited on a surface [45]. The same is true

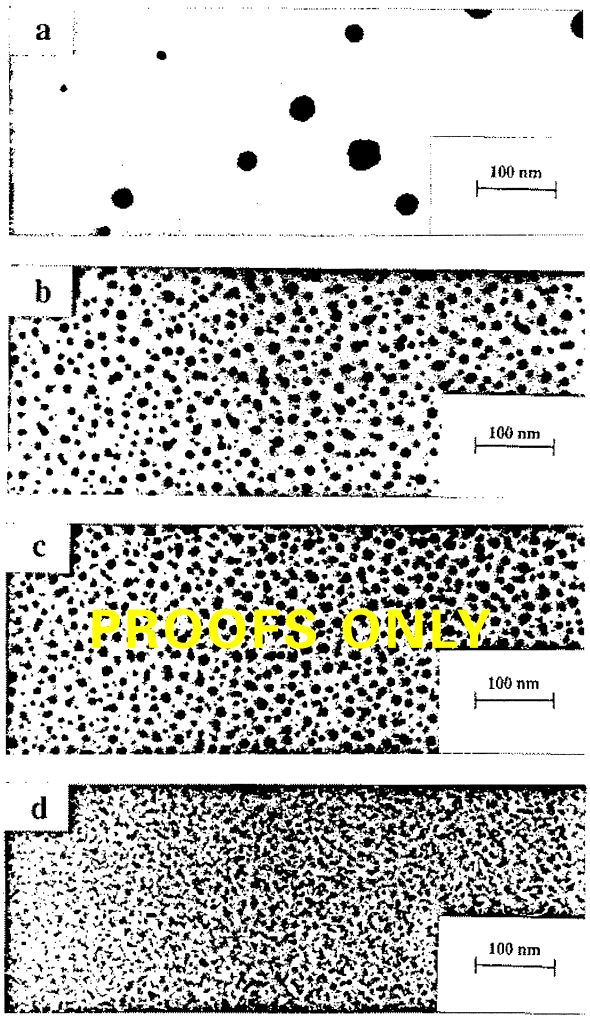

Figure 1. By changing the mean size of the incident antimony clusters, one can dramatically change the morphology of the submonolayer film. The four micrographs have been obtained for the same thickness (1 nm) and deposition rate (5×10^{-3} nm s^{-1}). The mean sizes are: (a) Sb_4, (b) Sb_16, (a) Sb_36, (a) Sb_240. The changes in morphology are interpreted by the different mobilities of the clusters as a function of their size, as well as their different coalescence dynamics and sensitivity to surface defects.

for SiC clusters where one can modify the electronic properties of the famous C_{60} clusters by introducing in a controlled way Si atoms before deposition [46]. This allows one to tune within a certain range the properties of the films by choosing the preparation conditions of the preformed clusters. It might also be anticipated that cluster nucleation is less sensitive to impurities than atomic nucleation. Atomic island growth can be dramatically affected by them, as exemplified by the celebrated case of the different morphologies of Pt islands grown on Pt(111) [47] which were actually the result of CO contamination at an incredibly low level: 10^{-10} mbar [48]. Instead, clusters, being larger entities, might interact less specifically with the substrate and its impurities. There is still no systematic way of organizing the clusters on a surface. One could try to pin them on selected sites such as defects or to encapsulate the clusters with organic molecules before deposition in order to obtain ordered arrays on a substrate [49].

2.2. Nanostructured Materials

Although the main focus in this chapter is the understanding of the first stages of growth, it is worth pointing out the interest in thicker nanostructured films (for a recent review of this field, see [7]). It is known [4, 5, 30] that the (magnetic, optical, and mechanical) properties of these films can be intrinsically different from their macrocrystalline counterparts. The precise reasons for this are currently being investigated, but one can cite the presence of a significant fraction (more than 10%) of atoms in configurations different from the bulk configuration, for example in grain boundaries [1]. It is reasonable to suppose that both dislocation generation and mobility may become significantly difficult in nanostructured films [4]. For example, recent studies of the mechanical deformation properties of nanocrystalline copper [50] have shown that high strain can be reached before the appearance of plastic deformation. A review of the effects of nanostructuration on the mechanical response of solids is given by Weertman and Averback in Chapter 13 of [7]. Another interesting property of these materials is that their crystalline order is intermediate between that of the amorphous materials (first neighbor order) and of crystalline materials (long range order). It is given by the size of the crystalline cluster, which can be tuned. For example, magnetic nanostructured materials can be modelled using the random anisotropy model developed for amorphous materials [51], just by adjusting the size of the local magnetic order to the size of the crystalline nanodomains (i.e., the size of the clusters) [52].

2.3. How Can One Deposit Clusters on Surfaces?

After detailing the potential interests of nanostructures, we now address the practical preparation methods by *cluster* deposition. Two main variants have been explored. Historically, the first idea has been to produce beams of *accelerated* (ionized) clusters and take advantage of the incident kinetic energy to enhance atomic mobility even at low substrate temperatures. This method does not lead in general to nanostructured materials but to films similar to those obtained by atomic deposition, with sometimes better properties. A more recent approach is to deposit neutral clusters, with *low energy* to preserve their peculiar properties when they reach the surface. The limit between the two methods is roughly at a kinetic energy of 0.1 to 1 eV/atom.

2.3.1. Accelerated Clusters

The group at Kyoto University was the first to explore the idea of depositing clusters with high kinetic energies (typically a few keV) to form thin films [53]. The basic idea of the ionized cluster beam (ICB) technique is that the cluster breaks upon arrival and its kinetic energy is transferred to the adatoms which then have high lateral (i.e., parallel to the substrate) mobilities on the surface. This allows one in principle to achieve epitaxy at low substrate temperatures, which is interesting to avoid diffusion at interfaces or other activated processes. Several examples of good epitaxy by ICB have been obtained by the Kyoto group: Al/Si [54] which has a large mismatch and many other couples of metals and ceramics on various crystalline substrates such as Si(100), Si(111), etc. Molecular dynamics (MD) simulations have supported this idea of epitaxy by cluster spreading [55]. The reader is referred to Yamada's reviews [53] for an exhaustive list of ICB applications, which also includes high energy cluster bombardment of surfaces to achieve sputter yields significantly higher than those obtained from atomic bombardment [56].

However, the physics behind these technological successes is not clear. In fact, the very presence of a significant fraction of large clusters in the beam seems dubious [57, 58]. There is some experimental evidence [53] offered by the Kyoto group to support the effective presence of a significant fraction of large clusters in the beam, but the evidence is not conclusive. In short, it is difficult to make a definite judgement about the ICB technique. There is no clear proof of the presence of clusters in the beam and the high energy of the incident particles renders difficult any attempt of modelling. The Kyoto group has clearly shown that ICB does lead to good quality films in many cases but it is not clear how systematic the improvement is when compared to atomic deposition techniques.

Haberland's group in Freiburg has developed recently a different technique called energetic cluster impact (ECI) where a better controlled beam of energetic clusters is deposited on surfaces [59]. Freiburg's group has shown that accelerating the clusters leads to improvements in some properties of the films: depositing slow clusters (energy per atom 0.1 eV) produces metal films

which can be wiped off easily, but accelerating them before deposition (up to 10 eV per atom) results in strongly adhering films [60]. MD simulations of cluster deposition [60] have explained qualitatively this behavior: while low energetic clusters tend to pile up on the substrate, leaving large cavities, energetic clusters lead to a compact film. It is interesting to note that, even for the highest energies explored in the MD simulations (10 eV per atom), no atoms were ejected from the cluster upon impact. The effect of film smoothening is only due to the flattening of the cluster when it touches the substrate. Some caution on the interpretation of these simulations is needed because of the very short time scales which can be simulated (some ps). Similar MD simulations of the impact of a cluster with a surface at higher energies have also been performed [61]. Recently, Palmer's group [62] has studied the interaction of Ag clusters on graphite for various incident kinetic energies (between 15 and 1500 eV). They have shown that, for *small* (Ag_3) clusters, the probability of a cluster penetrating the substrate critically depends on its orientation relative to the substrate.

2.3.2. Low Energy Clusters

Another strategy to grow nanostructures with cluster beams consists of depositing *low energy* particles [13, 14, 20, 49, 63–67], as pioneered in the 1980s at Lyon University [13], termed low energy cluster beam deposition (LECBD). Ideally, by depositing the clusters with low kinetic energies, one would like to conserve the memory of the free cluster phase [13] to form thin films with original properties. Since the kinetic energy is of the order of 10 eV per cluster [68] (i.e. a few meV per atom which, is negligible compared to the binding energy of an atom in the cluster), no fragmentation of the clusters is expected upon impact on the substrate. Low energy cluster films are generally porous [60, 69], which is interesting in noting one of the peculiarities of the clusters: their high surface/volume ratio which affects all the physical (structural, electronic) properties as well as the chemical reactivity (catalysis). Concerning deposition of carbon clusters, experiments [13, 21] as well as simulations [70] have shown that the carbon clusters preserve their identity in the thick film. Another interesting type of nanostructured film grown by cluster deposition is the growth of cermets by combining a cluster beam with an atomic beam of the encapsulating material [71]. The point is that the size of the metallic particles is determined by the incident cluster size and the concentration by the ratio of the two fluxes. Then, these two crucial parameters can be varied independently, in contrast to the cermets grown from atomic beams and precipitation upon annealing.

Cluster beams are generated by different techniques: multiple expansion cluster source (MECS) [39], gas aggregation [12, 13, 63, 72, 73], etc. All these techniques produce a beam of clusters with a distribution of sizes, with a dispersion of about half the mean size. For simplicity, we will always refer to this mean size. In gas-aggregation techniques, an atomic vapor obtained from a heated crucible is mixed with an inert gas (usually Ar or He) and the two are cooled by adiabatic expansion, resulting in supersaturation and cluster formation. The mean cluster size can be monitored by the different source parameters (such as the inert gas pressure) and can be measured by a time of flight mass spectrometer. For further experimental details on this technique, see [13, 74]. To produce clusters of refractory materials, a different evaporation technique is needed: laser vaporization [13, 74, 75]. A plasma created by the impact of a laser beam focused on a rod is thermalized by injection of a high pressure He pulse (typically 3–5 bars during 150 to 300 μs), which permits the cluster growth. The mean cluster size is governed by several parameters such as the helium flow, the laser power, and the delay time between the laser shot and the helium pulse. As a consequence of the pulsed laser shot, the cluster flux reaching the surface is not continuous but *chopped*. Typical values for the chopping parameters are: active portion of the period $\simeq 100$ μs and chopping frequency $f = 10$ Hz.

The experimental systems described in this chapter have been obtained from intense supersonic jets of nanoclusters with sizes ranging from a few tens to a few thousands of atoms (diameter 1 to a few nm). Our group has developed a cluster generator based on a combined laser vaporization–gas condensation source [44]. Briefly, a YAG laser (=532 nm, pulse duration a few ns, frequency 30 Hz) or a Ti–Sapphire laser (=790 nm, pulse duration a few μs, frequency 30 Hz) is used to vaporize the target rod mounted in the source chamber (Fig. 2). Combined with the laser pulse, a high pressure gas pulse (He, 3 to 6 bars, pulse duration 200 to 500 s) is injected in the source chamber to rapidly cool the plasma generated at the target surface and to nucleate clusters which are subsequently completely cooled and stabilized in the supersonic expansion taking place at the exit nozzle of the source. The main feature of this type of cluster source compared to other ones currently used (thermal, sputtering) is the very high cooling rate up to about 10^{10} K/s which governs the formation of original nanoscale systems in nonequilibrium conditions. From the key parameters of the source (laser pulses, gas pulses/continuous gas flow, delay between both pulses, and geometries of the nucleation chamber in the source and the nozzle), it is possible to control the cluster size distributions measured in the high resolution time of flight (TOF) mass spectrometer mounted immediately after the skimmer (Fig. 2). For that purpose, neutral clusters are photoionized using a tunable excimer-dye laser and then deviated and accelerated at the entrance of the TOF

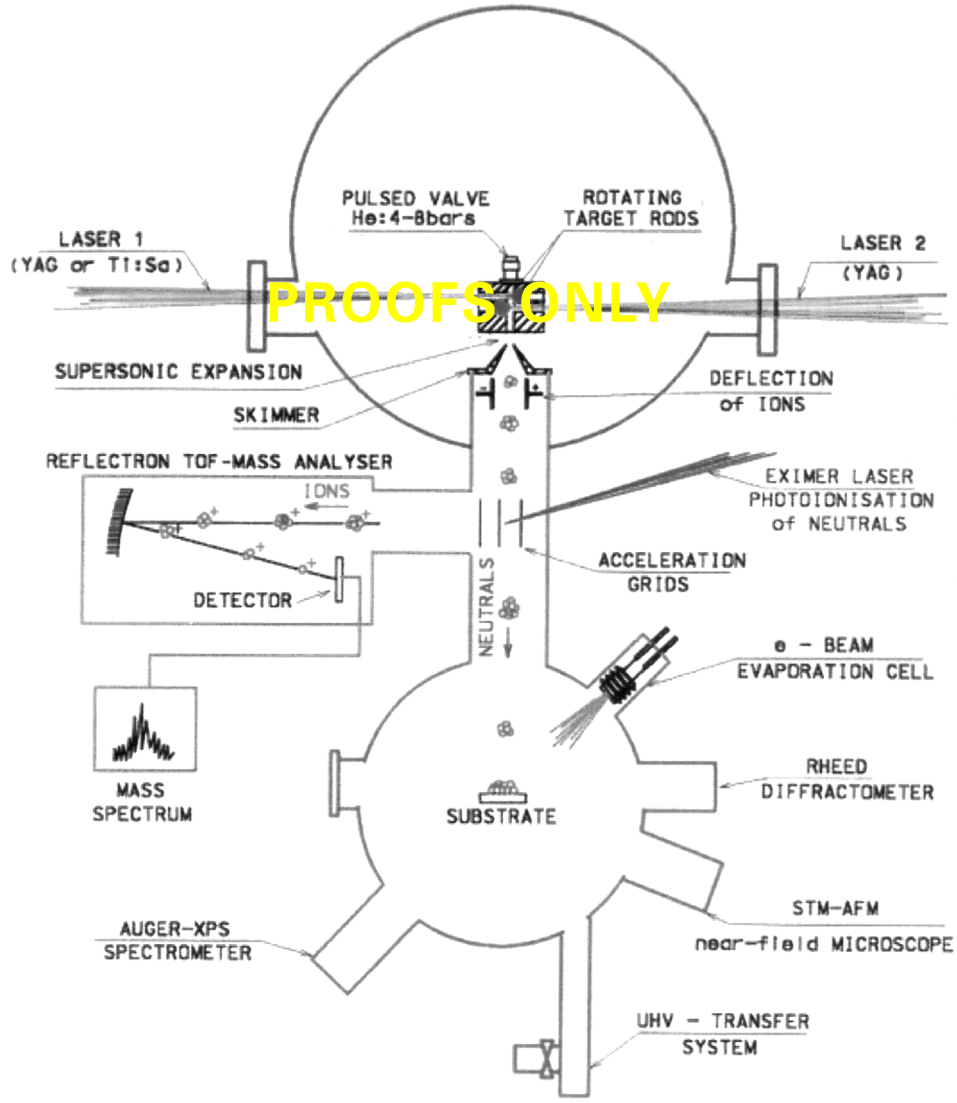

Figure 2. Schematic view of the cluster generator based on a combined laser vaporization/inert gas condensation source, associated with a high resolution time of flight mass spectrometer (reflectron) for the studies of free clusters and an ultrahigh vacuum (UHV) deposition chamber for cluster assembled film preparations. The source can operate with one or two independent laser/target arrangements for the production of pure clusters as well as mixed clusters. Some characterization techniques of the films are available *in situ* in UHV: reflection high energy electron diffractometry, scanning tunneling–atomic force near field microscopy, and Auger–X-ray photoelectron spectrometry. A UHV transfer system is used for sample transfers to *ex situ* equipment. An electron-beam evaporator *in situ* in UHV is used for co-deposition experiments to produce films of clusters embedded in various media.

line. At this stage, photoionization near threshold and photofragmentation experiments are performed on free clusters to characterize their structures and properties.

For mixed cluster production (bimetallic, Si–C), both methods have been developed based on the use of a compound target directly mounted in the source or a special source with two independent targets simultaneously vaporized by two independent lasers (Fig. 2). When using the technique with a compound target, it has been verified for all bimetallic systems studied [i.e., Pt–Pd (29), Au–Ni (30), Au–Ag (26), Co–Sm (22)] that the clusters exhibit the same composition as the target rod. However, depending on some specific effects such as segregation, atoms can be inhomogeneously distributed in the cluster.

In the particular case of LECBD experiments, only neutral clusters having the very low energy gained in the supersonic expansion at the exit of the source (a few 10^{-2} eV per atom) are deposited on various substrates in the UHV deposition chamber mounted on line with the cluster generator–TOF arrangement (Fig. 2). In our experiments, the complete distributions of neutral clusters (nearly Gaussian in shape and rather narrow from our laser vaporization generator) are directly deposited on the substrates to grow films, which allows one to

reach relatively high deposition rates (0.1 nm/minute to 0.1 nm/second) for all kinds of clusters. Moreover, by co-depositing on the same substrate an atomic beam emitted by the e-beam evaporator mounted in the deposition chamber (Fig. 2), it is possible to produce films of clusters embedded in various matrices (metallic, transparent oxides). Since both cluster and atomic beams are independent, this last technique allows one to produce any kind of cluster-matrix system, even with miscible elements, in a wide range of cluster concentration.

2.3.3. Other Approaches

Alternatively, one can deposit accelerated clusters onto a buffer layer which acts as a "mattress" to dissipate the kinetic energy. This layer is then evaporated, which leads to clusters soft-landing onto the substrate [76, 77]. The advantage of this method is that it is possible to select the mass of the ionized clusters before deposition. However, it is difficult with this technique to reach high enough deposition rates to grow films in reasonable times. Vitomirov et al. [78] deposited *atoms* onto a rare-gas buffer layer: the atoms first clustered on top and within the layer which was afterwards evaporated, allowing the clusters to reach the substrate. Finally, deposition of clusters from a scanning tunneling microscope (STM) tip has been shown to be possible, both theoretically [79] and experimentally [80].

3. MODELS OF PARTICLE DEPOSITION

We describe in this section some models which allow one to understand the first stages of film growth by low energy cluster deposition (for a thorough review, see also [14]). These models can also be useful for understanding the growth of islands from *atomic* beams in the submonolayer regime in *simple* cases, namely (almost) perfect substrates, irreversible aggregation, etc., and they allow one to understand and quantify many aspects of the growth: for a review of analysis of atomic deposition with this kind of model, see [29, 40, 81, 82]. The models described below are similar to previous models of diffusing particles that aggregate, but such "cluster–cluster aggregation" models [83] do not incorporate the possibility of continual injection of new particles via deposition, an essential ingredient for thin film growth.

Given an experimental system (substrate and cluster chemical nature), how can one predict the growth characteristics for a given set of parameters (substrate temperature, incoming flux of clusters, ...)?

A first idea—the "brute-force" approach—would be to run an MD simulation with ab initio potentials for the particular system one wants to study. It should be clear that such an approach is bound to fail since the calculation time is far too large for present-day computers. Even using empirical potentials (such as Lennard-Jones, embedded atom, or tight-binding) will not do because there is an intrinsically large time scale in the growth problem: the mean time needed to fill a significant fraction of the substrate with the incident particles. An estimate of this time is fixed by t_{ML}, the time needed to fill a monolayer: $t_{\mathrm{ML}} \simeq 1/F$ where F is the particle flux expressed in monolayers per second (ML/s). Typically, the experimental values of the flux are lower than 1 ML/s, leading to $t_{\mathrm{ML}} \geq 1$s. Therefore, there is a time span of about 13 decades between the typical vibration time (10^{-13} s, the lower time scale for the simulations) and t_{ML}, rendering hopeless any "brute-force" approach.

There is a rigorous way [84] of circumventing this time span problem: the idea is to "coarsen" the description by defining *elementary processes*, an approach somewhat reminiscent of the usual (length, energy) renormalization of particle physics [8]. One "sums up" all the short time processes (typically, atomic thermal vibrations) in effective parameters (transition rates) valid for a higher level (longer time) description. We will now briefly describe this rigorous approach and then proceed to show how it can be adapted to cluster deposition.

3.1. Choosing the Elementary Processes

Voter [84] showed that the interatomic potential for any system can be translated into a finite set of parameters, which then provides the exact dynamic evolution of the system. Recently, the same idea has been applied to Lennard–Jones potentials [85] by using only *two* parameters. The point is that this coarse-grained, lattice-gas approach needs orders of magnitude less computer power than the MD dynamics described above. One can understand the basic idea by the following simple example: for the MD description of the diffusion of an atom by hopping, one has to follow in detail its motion at the picosecond scale, where the atom mainly oscillates in the bottom of its potential well. Only rarely at this time scale will the atom jump from site to site, which is what one is interested on. Voter showed that, provided some conditions are met concerning the separation of these two time scales, and restricting the motion to a regular (discrete) lattice (see [84] for more details), one could replace this "useless" information by an effective parameter taking into account all the detailed motion of the atom within the well (including the correlations between the motions of the atom and its neighbors) and allowing a rapid evaluation of its diffusion rate.

Unfortunately, this rigorous approach is not useful for *cluster* deposition, because the number of atomic degrees of freedom (configurations) is too high. Instead, one chooses—from physical intuition—a "reasonable" set of elementary processes, whose magnitudes are used as *free parameters*. This allows one to understand the role of each of these elementary processes during the growth and then to fit their value from experiments (Fig. 3). These are the models which we will study in this chapter,

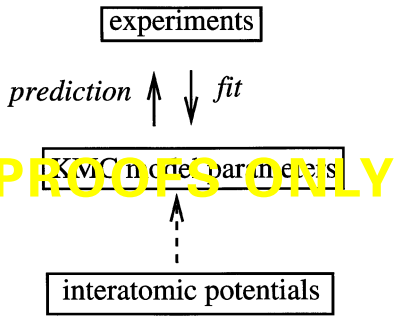

Figure 3. Principle of a kinetic Monte Carlo simulation (see text).

with precise examples of parameter fit (see Section 6). Examples of such fits from experimental data for *atomic* deposition include homoepitaxial growth of GaAs(001) [86], Pt(100) [87], or several metal(100) surfaces [88]. Of course, fitting is not very reliable when there are too many (almost free) parameters. Interesting alternatives are intermediate cases, where parameters are determined from known potentials but with a simplified fitting procedure taking into account what is known experimentally of the system under study: see [89] for a clear example of such a possibility.

3.2. Predicting the Growth from the Selected Elementary Processes

To be able to adjust the values of the elementary processes from experiments, one must first predict the growth from these processes. The oldest way is to write "rate equations" which describe in a mean-field way the effect of these processes on the number of isolated particles moving on the substrate (called monomers) and islands of a given size. The first author to attempt such an approach for growth was Zinsmeister [90] in 1966, but the general approach is similar to the rate equations first used by Smoluchovsky for particle aggregation [91]. In the 1970s, many papers dealing with better mean-field approximations and applications of these equations to interpret experimental systems were published. The reader is referred to the classical reviews by Venables and co-workers [92, 93] and Stoyanov and Kaschiev [94] for more details on this approach. More recently, there have been two interesting improvements. The first is by Villain and co-workers which has simplified enormously the mathematical treatment of the rate equations, allowing one to understand easily the results obtained in a variety of cases [95, 96]. Pimpinelli et al. have recently published a summary of the application of this simplified treatment to many practical situations using a unified approach [97]. The second improvement is due to Bales and Chrzan [98] who have developed a more sophisticated self-consistent rate-equations approach which gives better results and allows one to justify many of the approximations made in the past. However, these analytical approaches are mean field in nature and cannot reproduce all the characteristics of the growth. Two known examples are the island morphology and the island size distribution [98].

The alternative approach to predict the growth are kinetic Monte Carlo (KMC) simulations. KMC simulations are an extension of the usual Monte Carlo [99–101] algorithm and provide a rigorous way of calculating the dynamical evolution of a complicated system where a large but *finite* number of random processes occur at given rates. KMC simulations are useful when one chooses to deal with only the slowest degrees of freedom of a system, these variables being only weakly coupled to the fast ones, which act as a heat bath [101]. The "coarsened" description of film growth (basically, diffusion) given above is a good example [84, 98, 102–105], but other applications [101] of KMC simulations include interdiffusion in alloys, slow phase separations, etc. The principle of KMC simulations is straightforward: one uses a list of all the possible processes together with their respective rates ν_{pro} and generates the time evolution of the system from these processes taking into account the random character of the evolution. For the simple models of film growth described below, systems containing up to 4000×4000 lattice sites can be simulated in a reasonable time (a few hours), which limits the finite size effects usually observed in this kind of simulation. Let us now discuss in some detail the way KMC simulations are implemented to reproduce the growth, once a set of processes has been defined, with their respective ν_{pro} taking arbitrary values or being derived from known potentials.

There are two main points to discuss here: the physical correctness of the dynamics and the calculation speed. Concerning the first point, it should be noted that, originally [99], Monte Carlo simulations aimed at the description of the *equations of state* of a system. Then, "the MC method performs a 'time' averaging of a model with (often artificial) stochastic kinetics [...]: time plays the role of a label characterizing the sequential order of states, and need not be related to the physical times" [106]. One should be cautious therefore of the precise Monte Carlo scheme used for the simulation when attempting to describe the kinetics of a system, as in KMC simulations. For example, there are doubts [107, 108] about some simulation work [109, 110] carried out using Kawasaki dynamics. This point is discussed in great detail in [108].

Let me address now the important problem of the calculation speed. One could naively think of choosing a time interval Δt smaller than all the relevant times in the problem, and then repeat the following procedure:

(1) Choose one particle randomly.
(2) Choose randomly one of the possible processes for this particle.

(3) Calculate the probability p_{pro} of this process happening during the time interval Δt ($p_{pro} = \nu_{pro}\Delta t$).
(4) Throw a random number p_r and compare it with p_{pro}: if $p_{pro} < p$ perform the process; if not go to the next step.
(5) Increase the time by Δt and goto (1).

This procedure leads to the correct kinetic evolution of the system but might be extremely slow if there is a large range of probabilities p_{pro} for the different processes (and therefore some $p_{pro} \ll 1$). The reason is that a significant fraction of the loops leads to rejected moves, (i.e., to no evolution at all of the system).

Instead, Bortz et al. [111] have proposed a clever approach to eliminate *all* the rejected moves and thus reduce dramatically the computational times. The point is to choose not the particles but the *processes*, according to their respective rate and the number of possible ways of performing this process (called Ω_{pro}). This procedure can be represented schematically as follows:

(1) Update the list of the possible ways of performing the processes Ω_{pro}.
(2) Randomly select one of the process, *weighting* the probability of selection by the process rate ν_{pro} and Ω_{pro}: $p_{pro} = (\nu_{pro}\Omega_{pro})/(\sum_{processes} \Omega_{pro}\nu_{pro})$.
(3) Randomly select a particle for performing this process.
(4) Move the particle.
(5) Increase the time by $dt = \left(\sum_{processes} \Omega_{pro}\nu_{pro}\right)^{-1}$
(6) Goto (1).

A specific example of such a scheme for cluster deposition is given below (Section 3.3). Note that the new procedure implies a less intuitive increment of time and that one has to create (and update) a list of all the Ω_{pro} constantly, but the acceleration of the calculations is worth the effort.

A serious limitation of KMC approaches is that one has to assume a finite number of local environments (to obtain a finite number of parameters): this confines KMC approaches to regular lattices, thus preventing a rigorous consideration of elastic relaxation, stress effects, etc., everything that affects not only the *number* of first or second nearest neighbors but also their precise position. Indeed, considering the precise position as in MD simulations introduces a *continuous* variable and leads to an infinite number of possible configurations or processes. Stress effects can be introduced approximately in KMC simulations, for example [112] by allowing a variation of the bonding energy of an atom to an island as a function of the island size (the stress depending on the size), but it is unclear how meaningful these approaches are (see also [113]). We should quote here a recent proposition [114] inspired by the old Frenkel–Kontorova model [115] which allows one to incorporate some misfit effects in rapid simulations. It remains to explore whether such an approach could be adapted to the KMC scheme.

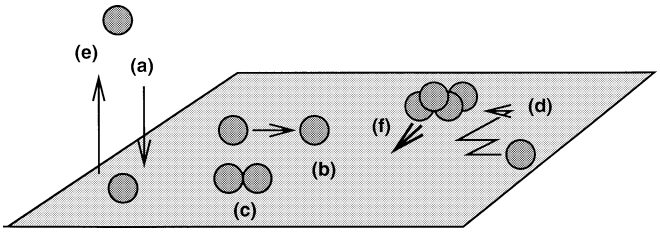

Figure 4. Main elementary processes considered in this chapter for the growth of films by cluster deposition. (a) Adsorption of a cluster by deposition; (b) and (d) diffusion of the isolated clusters on the substrate; (c) formation of an island of two monomers by juxtaposition of two monomers (nucleation); (d) growth of a supported island by incorporation of a diffusing cluster; (e) evaporation of an adsorbed cluster. We also briefly consider the influence of island diffusion (f).

3.3. Basic Elementary Processes for Cluster Growth

What is likely to occur when clusters are deposited on a surface? We will present here the elementary processes which will be used in cluster deposition models: deposition, diffusion, and evaporation of the clusters and their interaction on the surface (Figs. 4 and 5). The influence of surface defects which could act as traps for the particles is also addressed.

A simple physical rationale for choosing only a limited set of parameters is the following (see Fig. 6). For any given system, there will be a "hierarchy" of time scales, and the relevant ones for a growth experiment are those much lower than $t_{ML} \simeq 1/F$. The others are too slow to act and can be neglected. The hierarchy of time scales (and therefore the relevant processes) depends of course on the precise system under study. It should be noted that for *cluster* deposition the situation is somewhat simpler than for atom deposition [116] since many elementary processes are very slow. For example, diffusion of clusters on top of an already formed island is very low [117], cluster detachment from the islands is insignificant, and edge diffusion is not an elementary process at all since the cluster cannot move as an entity over the island edge (as we will discuss in Section 7.2, the equivalent process is cluster–cluster coalescence by atomic motion). Let us now discuss in detail each of the elementary processes useful for cluster deposition.

The first ingredient of the growth, *deposition*, is quantified by the flux F (i.e., the number of clusters that are deposited on the surface per unit area and unit time). The flux is usually uniform in time, but in some

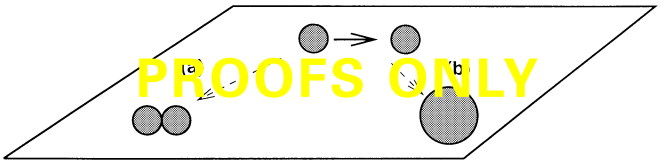

Figure 5. Possible interaction of two clusters touching on the surface: (a) pure juxtaposition and (b) total coalescence. Intermediate cases (partial coalescence) are possible and will be described later.

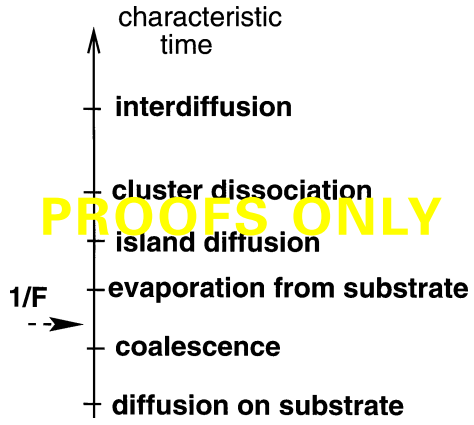

Figure 6. Time scales of some elementary processes considered in this chapter for the growth of films by cluster deposition. The relevant processes are those whose time scales are smaller than the deposition time scale shown by the arrow in the left. In this case, models including only cluster diffusion on the substrate and cluster–cluster coalescence are appropriate. "Island diffusion" refers to the motion of islands of clusters as a whole, "cluster dissociation" to the evaporation of atoms from the cluster, and "interdiffusion" to the exchange of atoms in the cluster with substrate atoms.

experimental situations it can be pulsed, (i.e., changed from a constant value to 0 over a given period). Chopping the flux can affect the growth of the film significantly [118], and we will take this into account when needed (Section 6.2.2).

The second ingredient is the *diffusion* of the clusters which have reached the substrate. We assume that the diffusion is Brownian (i.e., the particle undergoes a random walk on the substrate). To quantify the diffusion, one can use both the usual diffusion coefficient D or the diffusion time τ (i.e. the time needed by a cluster to move by one diameter). These two quantities are connected by $D = d^2/(4\tau)$ where d is the diameter of the cluster. Experiments show that the diffusion coefficient of a cluster can be surprisingly large, comparable to the atomic diffusion coefficients. The diffusion is here supposed to occur on a perfect substrate. Real surfaces always present some defects such as steps, vacancies, or adsorbed chemical impurities. The presence of these defects on the surface could significantly alter the diffusion of the particles and therefore the growth of the film. We will include here one simple kind of defect, a perfect trap for the clusters which definitively prevents them from moving.

A third process which could be present in growth is *reevaporation* of the clusters from the substrate after a time τ_e. It is useful to define $X_S = \sqrt{D\tau_e}$, the mean diffusion length on the substrate before desorption.

The last simple process we will consider is the *interaction* between the clusters. The simplest case is when aggregation is irreversible and particles simply remain juxtaposed upon contact. This occurs at low temperatures. At higher temperatures, cluster–cluster coalescence will be active (Fig. 5). Thermodynamics teaches us that coalescence should always happen but without specifying the kinetics. Since many clusters are deposited on the surface per unit time, kinetics is here crucial to determine the shape of the islands formed on the substrate. A total comprehension of the kinetics is still lacking, for reasons that we will discuss later (Section 7.2). We note that the shape of the clusters and the islands on the surface need not be perfectly spherical, even in the case of total coalescence. Their interaction with the substrate can lead to half spheres or even flatter shapes depending on the contact angle. Contrary to what happens for atomic deposition, a cluster touching an island forms a huge number of atom–atom bonds and will not detach from it. Thus, models including *reversible* particle–particle aggregation [22] are not useful for cluster deposition.

The specific procedure to perform a rapid KMC simulation of a system (linear size L) when deposition, diffusion, and evaporation of the monomers are included is the following. The processes are: deposition of a particle [$\nu_{\text{depo}} = F$, $\Omega_{\text{depo}} = L^2$ (it is possible to deposit a particle on each site of the lattice)], diffusion of a monomer ($\nu_{\text{diff}} = 1/\tau$, $\Omega_{\text{diff}} = \rho L^2$ where ρ is the monomer density on the surface), and evaporation of a monomer ($\nu_{\text{evap}} = 1/\tau_e$, $\Omega_{\text{evap}} = \rho L^2$). For each loop, one calculates two quantities $p_{\text{drop}} = F/(F + \rho(1/\tau_e + 1/\tau))$ and $p_{\text{dif}} = (\rho/\tau)/(F + \rho(1/\tau_e + 1/\tau))$. Then, one throws a random number $p(0 < p < 1)$ and compares it to p_{drop} and p_{dif}. If $p < p_{\text{drop}}$, a particle is deposited in a random position; if $p > p_{\text{drop}} + p_{\text{dif}}$, a monomer (randomly selected) is removed; otherwise we just move a randomly chosen monomer. After each of these possibilities, one checks whether an aggregation has taken place (which modifies the number of monomers on the surface, and therefore the number of possible diffusion or evaporation moves), increases the time by $dt = 1/(FL^2 + \rho L^2(1/\tau_e + 1/\tau))$, and goes to the next loop.

The usual game for theoreticians is to combine these elementary processes and predict the growth of the film. However, experimentalists are interested in the reverse strategy: from (a set of) experimental results, they wish to understand which elementary processes are actually present in their growth experiments and the magnitudes of each of them, what physicists call understanding a phenomenon. The problem, of course, is that with so many processes, many combinations will reproduce the same experiments (see specific examples below). Then, some clever guesses are needed to first identify which processes are present. For example, if the saturation island density does not change when flux (or substrate temperature) is changed, one can guess that nucleation is mostly occurring on defects of the surface.

In view of these difficulties, next section is devoted to predict the growth when the microscopic processes (and their values) are known. Later, in Section 5, we propose a detailed procedure to identify and quantify the

microscopic process from the experiments. Finally, Section 6 reviews the experimental results obtained for cluster deposition.

4. PREDICTING GROWTH WITH COMPUTER SIMULATIONS

The scope of this section is to find formulas or graphs to deduce the values of the microscopic processes (diffusion, evaporation, ...) from the observed experimental quantities (island density, island size histograms, ...). The "classical" studies [92–94] have focused on the evolution of the concentration of islands on the surface as a function of time, and especially on the saturation island density (i.e., the maximum of the island density observed before reaching a continuous film). The reason is of course the double possibility of calculating it from rate equations and measuring it experimentally by conventional microscopy. We will show other interesting quantities such as island size distributions which are measurable experimentally and have been recently calculated by computer simulations [119–124].

We will study the two limiting cases of pure juxtaposition and total coalescence (which are similar to two- and three-dimensional growth in atomic deposition terminology) separately. Experimentally, the distinction between the two cases can be made by looking at the shape of the supported islands: if they are circular (and larger than the incident clusters) they have been formed by total coalescence; if they are ramified they have been formed by pure juxtaposition (see several examples below, Section 6).

In both cases, we analyze how the growth proceeds when different processes are at work: diffusion, evaporation, defects acting as traps, island mobility, etc. In the simulations, we often take the diffusion time τ to be the unit time: in this case, the flux is equivalent to the normalized flux ϕ (see Table 1) and the evaporation time corresponds to τ_e/τ. The growth is characterized by the kinetics of island formation, the value of the island concentration at saturation N_{sat} (i.e., the maximum value reached before island–island coalescence becomes important), and the corresponding values of the thickness e_{sat} and condensation coefficient C_{sat}, useful when evaporation is important (the condensation coefficient is the ratio of matter actually present on the substrate over the total number of particles sent on the surface, also called the thickness $e = Ft$; see Table 1).

We also give the island size distributions corresponding to each growth hypothesis. These have proven useful as a tool for experimentalists to distinguish between different growth mechanisms [117, 123, 124]. By *size* of an island, we mean the surface it occupies on the substrate. For "two-dimensional" islands (i.e., formed by pure juxtaposition), this is the same as the island mass (i.e., its number of monomers). For "three-dimensional" islands (formed by total coalescence), their projected surface is the easiest quantity to measure by microscopy. It should be noted that for three-dimensional (30) islands, their projected surface for a given mass depends on their shape, which is assumed here to be pyramidal (close to a half-sphere). It has been shown [88, 103] that by normalizing the size histograms, one obtains a "universal" size distribution independent of the coverage, the flux, or the substrate temperature for a large range of their values.

4.1. Pure Juxtaposition: Growth of One Cluster Thick Islands

We first study the formation of the islands in the limiting case of pure juxtaposition. This is done for several growth hypotheses. The rate-equations treatment is given in [14].

4.1.1. Complete Condensation

Let me start with the simplest case where only diffusion takes place on a perfect substrate (no evaporation). Figure 7a shows the evolution of the monomer (i.e., isolated clusters) and island densities as a function of deposition time.

We see that the monomer density rapidly grows, leading to a rapid increase of island density by monomer–monomer encounter on the surface. This goes on until the islands occupy a small fraction of the surface, roughly 0.1% (Fig. 8a). Then, islands capture efficiently the monomers, whose density decreases. As a consequence, it becomes less probable to create more islands, and their number increases more slowly. When the coverage reaches a value close to 15% (Fig. 8b), coalescence will start to decrease the number of islands. The maximum number of islands at saturation N_{sat} is thus reached for coverages around 15%. Concerning the dependence of N_{sat} as a function of the model parameters, it has been shown that the maximum number of islands per unit area formed on the surface scales as $N_{\text{sat}} \simeq (F/D)^{1/3}$ [92, 94]. Recent simulations [98, 117] and theoretical analysis [95] have shown that the precise relation is $N_{\text{sat}} = 0.53(F\tau)^{0.36}$ for the *ramified* islands produced by pure juxtaposition (Fig. 9).

It should be noted that if cluster diffusion is vanishingly small, the above relation does not hold: instead, film growth proceeds as in the percolation model [125], by random paving of the substrate. An experimental example of such a situation has been given in [126].

4.1.2. Evaporation

What happens when evaporation is also included? Figure 7b shows that now the monomer density becomes roughly a *constant*, since it is now mainly determined by the balancing of deposition and evaporation. As expected, the constant concentration equals $F\tau_e$ (solid line). Then the number of islands increases linearly with time (the island creation rate is roughly proportional to

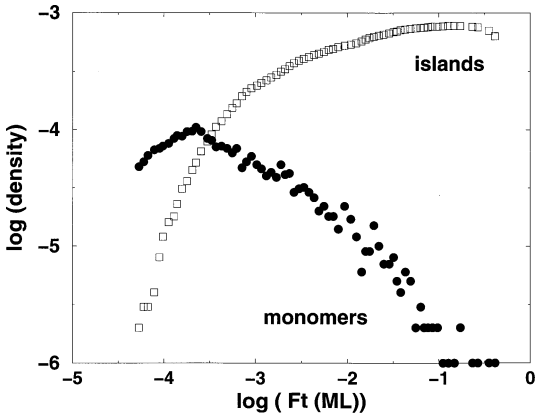

(a)

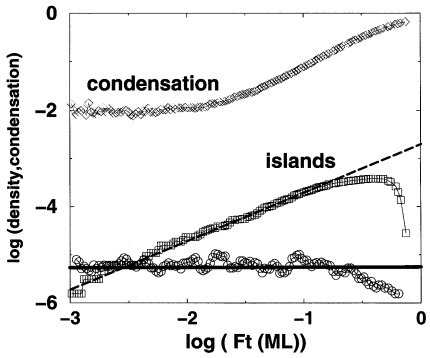

(b)

Figure 7. Evolution of the monomer and island densities as a function of the thickness (in monolayers), for islands formed by pure juxtaposition: (a) complete condensation, $F = 10^{-8}$, $\tau_e = 10^{10}(\tau = 1)$ (these values mean $X_S = 10^5$ and $\ell_{CC} = 22$) and (b) important evaporation, $F = 10^{-8}$, $\tau_e = 600(\tau = 1)$ ($X_S = 25$ and $\ell_{CC} = 22$). ℓ_{CC} represents the mean island separation at saturation for the given fluxes when there is no evaporation [119]. The length units correspond to the incident cluster (monomer) diameter. In (b) the "condensation" curve represents the total number of particles actually present on the surface divided by the total number of particles sent on the surface (F/t). It would be 1 for the complete condensation case, neglecting the monomers that are deposited on top of the islands. The solid line represents the constant value expected for the monomer concentration, while the dashed line corresponds to the linear increase of the island density (see text).

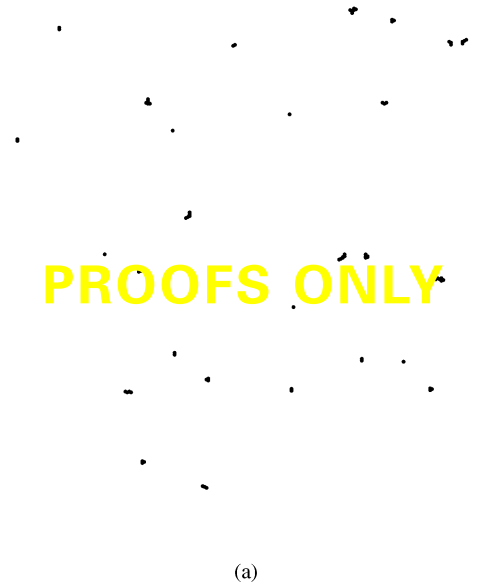

(a)

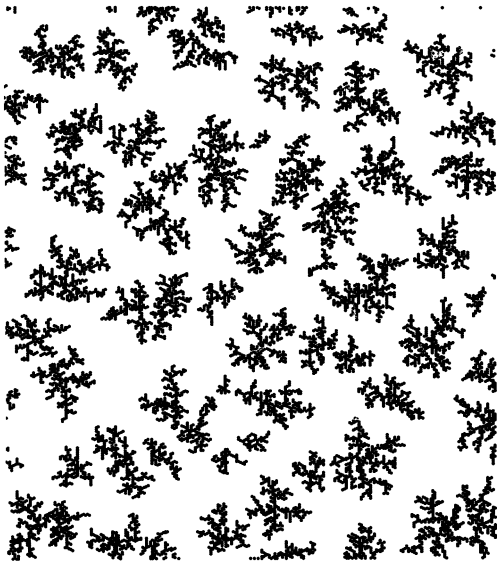

(b)

Figure 8. Morphology of a submonolayer deposit in the case of growth with complete condensation and pure juxtaposition: (a) $\theta = 0.1\%$; (b) $\theta = 15\%$. The values of the parameters are $F = 10^{-8}$ ML/s, $\tau = 1$, and $L = 300$.

the square monomer concentration [14]). One can also notice that only a small fraction (1/100) of the monomers effectively remains on the substrate, as shown by the low condensation coefficient value at early times. This can be understood by noting that the islands grow by capturing only the monomers that are deposited within their "capture zone" (comprised between two circles of radius R and $R + X_S$). The other monomers evaporate before reaching the islands. When the islands occupy a significant fraction of the surface, they capture rapidly the monomers. This has two effects: the monomer density starts to decrease, and the condensation coefficient starts to increase. Shortly after, the island density saturates and starts to decrease because of island–island coalescence.

Figure 9 shows the evolution of the maximum island density in the presence of evaporation. A detailed analysis of the effect of monomer evaporation on the growth is given in [119], where the regime of "direct impingement" which arises when $X_S \leq 1$ is also discussed: islands are formed by *direct impingement* of incident clusters as first neighbors of previously adsorbed clusters and grow by direct impingement of clusters on the island boundary. A summary of the results obtained in the various regimes spanned as the evaporation time τ_e decreases is given in [14].

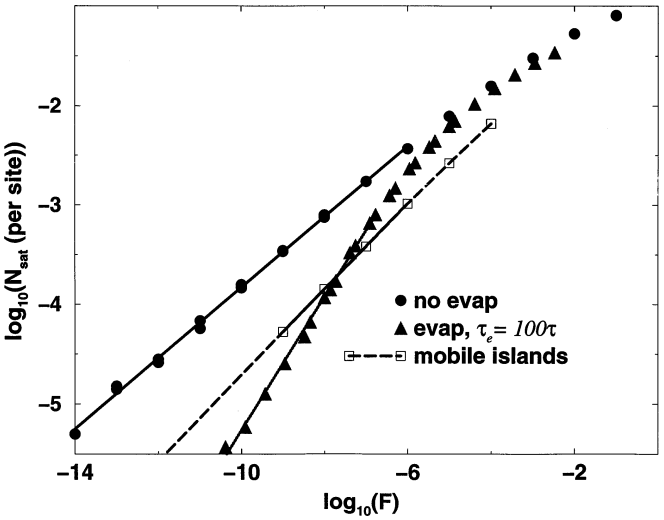

Figure 9. Saturation island density as a function of the normalized flux ($\tau = 1$) for different growth hypotheses indicated on the figure, always in the case of island growth by pure juxtaposition. "No evap" (circles) means complete condensation. Triangles show the densities obtained if there is evaporation, for $\tau_e = 100$. In the preceding cases, islands are supposed to be immobile. This hypothesis is relaxed for the last set of data, *mobile islands* (squares), where island mobility is supposed to decrease as the inverse island size [104] (there is no evaporation). The dashed line is an extrapolation of the data for the low normalized fluxes. Fits of the different curves in the low-flux region give "no evap" (solid line): $N_{sat} = 0.53(F\tau)^{0.36}$, "evap" (dotted line): $N_{sat} = 0.26F^{0.67}\tau^{-1/3}\tau_e$ (for the τ and τ_e exponents, see [119]), and "mobile islands" (dashed line): $N_{sat} = 0.33(F\tau)^{0.42}$.

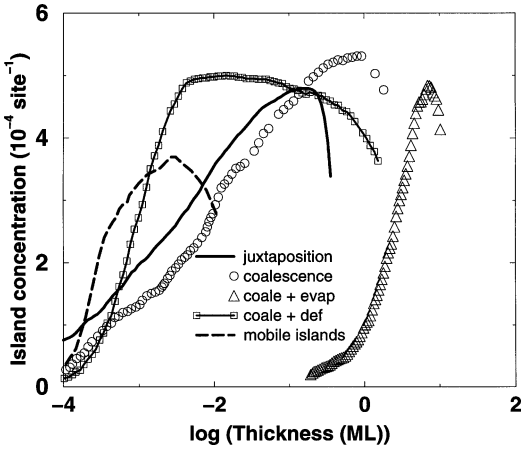

Figure 10. Evolution of the island density as a function of the thickness for different growth hypotheses. This figure shows that the *same* saturation density can be obtained for films grown in very different conditions. The different sets of data represent: *triangles*—growth with coalescence and evaporation, $\tau_e = 100\tau$ and $F\tau = 1.2 \times 10^{-8}$; *circles*—growth with coalescence but without evaporation ($F\tau = 3 \times 10^{-10}$); *solid line*—growth with pure juxtaposition without evaporation ($F\tau = 2.5 \times 10^{-9}$); *squares*—growth with coalescence on defects (defect concentration : 5×10^{-4} per site) and $F\tau = 10^{-14}$ (no evaporation); *dashed line*—growth with pure juxtaposition without evaporation but with mobile islands, $F\tau = 10^{-8}$.

4.2. Total Coalescence: Growth of Three-Dimensional Islands

If clusters coalesce when touching, the results are slightly different from those given in the preceding section, mainly because the islands occupy a smaller portion of the substrate at a given thickness. Therefore, in the case of complete condensation for example, saturation arises at a higher thickness (Fig. 10) even if the *coverage* is approximately the same (matter is "wasted" in the dimension perpendicular to the substrate). However, the main qualitative characteristics of the growth correspond to those detailed in the preceding section. Figure 11 shows the evolution of the maximum island density in that case, where the three-dimensional islands are assumed to be roughly half-spheres (actually, pyramids were used in these simulations which were originally intended for atomic deposition [131]). The analytical results obtained from a rate-equations treatment are given in [14]. If the islands are more spherical (i.e., the contact angle is higher), a simple way to adapt these results to the kinetic evolution of island concentration (Fig. 10) is to multiply the thickness by the appropriate form factor, 2 for a sphere for example. Indeed, if islands are spherical, the same coverage is obtained for a thickness double that obtained for the case of half-spheres (there are two identical half-spheres). This is a slight approximation since one has to assume that the capture cross section (which governs the growth) is identical for the two shapes: this is not exactly true [119] but is a very good approximation.

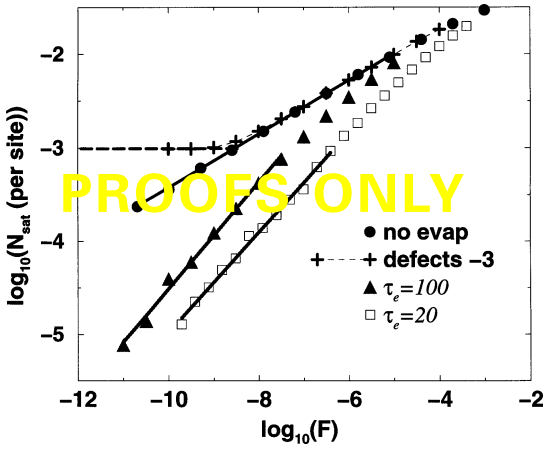

Figure 11. Saturation island density as a function of the normalized flux ($\tau = 1$) for different growth hypotheses in the case of growth by total coalescence (3D islands). We show the densities obtained for the complete condensation case (filled circles) and for two different evaporation times: $\tau_e = 100$ (triangles) and $\tau_e = 20$ (squares). The label *defects* means growth in presence of defects which act as nucleation centers. Their concentration is 10^{-3} per site. The dashed line is an extrapolation of the defect data for the low normalized fluxes. Fitting the simulation data leads to the following numerical relations: $N_{sat} = 0.27(F\tau)^{0.286}$ when there is no evaporation (solid line); $N_{sat} \sim 0.039F^{0.55}\tau^{-2/3}\tau_e^{4/3}$ when evaporation is significant (from an approximation for the two dotted curves). The exponents for τ and τ_e have been derived from a rate-equations treatment (see [14]).

5. HOW TO ANALYZE EXPERIMENTAL DATA

Figures 9 and 11 constitute in some sense "abacuses" from which one can determine the value of the microscopic parameters (diffusion, evaporation) if the saturation island density is known. The problem is: does the measured island density correspond to the defect concentration of the surface or to homogeneous nucleation? If the latter is true, which curve should be used to interpret the data? In other words, is evaporation present in the experiments and what is the magnitude of τ_e? We will now give some tricks to first find out which processes are relevant and then how they can be quantified.

Let us concentrate first on the presence of defects. One possibility is to look at the evolution of N_{sat} with the flux. As already explained, if this leaves unaffected the saturation density, nucleation is occurring on defects. A similar test can be performed by changing the substrate temperature, but there is the nagging possibility that this changes the defect concentration on the surface. It is also possible to study the kinetics of island nucleation, (i.e., look at the island concentration as a function of thickness or coverage). The presence of defects can be detected by the fact that the maximum island density is reached at very low coverages (typically less than 1%; see Fig. 10) and/or by the fact that the nucleation rate (i.e., the derivative of the island density) scales as the flux and not as the square flux: see Section 3 of [94] for more details. One should be careful, however, to check that all the islands, even those containing a few particles, are visible in the microscope images. This is a delicate point for atomic deposition [135] but should be less restrictive for clusters since each cluster has already a diameter typically larger than a nanometer. Of course all this discussion assumes that the defects are of the "ideal" kind studied here (i.e., perfect traps). If atoms can escape from the defects after some time, the situation is changed but we are unaware of studies on this question.

The question of evaporation is more delicate. First, one should check whether particle reevaporation is important. In principle, this can be done by measuring the condensation coefficient (i.e., the amount of matter present on the surface as a function of the amount of matter brought by the beam). If possible, this measure leaves no ambiguity. Otherwise, the kinetics of island creation is helpful. If the saturation is reached at low thicknesses ($e_{\text{sat}} \leq 0.5$ML), this means that evaporation is not important. Another way of detecting particle evaporation is by studying the evolution of the saturation island density with the flux: in the case of 2D growth (Fig. 9), the exponent is 0.36 when evaporation is negligible but roughly 0.66 when evaporation significantly affects the growth [119]. There are similar differences for 3D islands: the exponent changes from 0.29 to 0.66 [136] (Fig. 11). Suppose now that one finds that evaporation is indeed important: before being able to use Figure 9 or 11, one has to know the precise value of τ_e. One way to find out is to make a precise fit of the kinetic evolution of the island density or the condensation coefficient (see Section 6.2.1 for an example). In next paragraph, we show how to find τ_e if one knows only the *saturation* values of the island density and the thickness.

As a summary, here is a possible experimental strategy to analyze the growth. First, get a series of micrographs of submonolayer films as a function of the thickness. The distinction between the pure juxtaposition and total coalescence cases can be easily made by comparing the size of the supported islands to the (supposedly known) size of the incident clusters. Also, if the islands are spherical, this means that coalescence has taken place, if they are ramified that clusters only juxtapose upon contact. Of course, all the intermediate cases are possible (see the case of gold clusters below). One can calculate the ratio of deposited thickness over the coverage: if this ratio is close to 1, islands are flat (i.e., one cluster thick); otherwise they are three dimensional (unless there is evaporation).

From these micrographs, it is possible to measure the island density as a function of the thickness. Figure 10 should be now helpful to distinguish between the different growth mechanisms. For example, if the saturation island density is obtained for large thicknesses (typically more than 1 ML), then evaporation is certainly relevant and trying to measure the condensation coefficient is important to confirm this point. It is clear from Figures 9 and 11 that the knowledge of N_{sat} alone cannot determine τ_e since many values of τ and τ_e can lead to the same N_{sat}. In the 2D case, the values of the microscopic parameters can be obtained by noting that the higher the evaporation rate, the higher the amount of matter "wasted" for film growth (i.e., reevaporated). One therefore expects that the smaller τ_e, the higher e_{sat}, which is confirmed by Figure 12a. Therefore, from the (known) value of e_{sat}, one can determine the value of the evaporation parameter $\eta = F\tau X_S^6$ (Fig. 12a). Once η is known, X_S is determined from Figure 12b since N_{sat} is known. $F\tau$ can afterward be determined (from X_S and η). This is only valid for $X_S \gg 1$ [119], a condition always fulfilled in experiments.

The 3D case is more difficult since the same strategy (measuring N_{sat} and e_{sat}) fails. The reason is that in the limit of high evaporation, e_{sat} goes as $e_{\text{sat}} \sim N_{\text{sat}}^{-1/2}$, thus bringing no independent information on the parameters [136]. The same is true for the condensation coefficient at saturation C_{sat}, which is a *constant* (i.e., independent of the value of τ_e or the normalized flux; see Fig. 13b). This counterintuitive result (one would think that the higher the evaporation rate, the smaller the condensation coefficient at saturation) can be understood by noting that *in this limit*, islands only grow by direct impingement of particles within them [136] and therefore X_S (or τ_e) has no effect on the growth. Fortunately, in

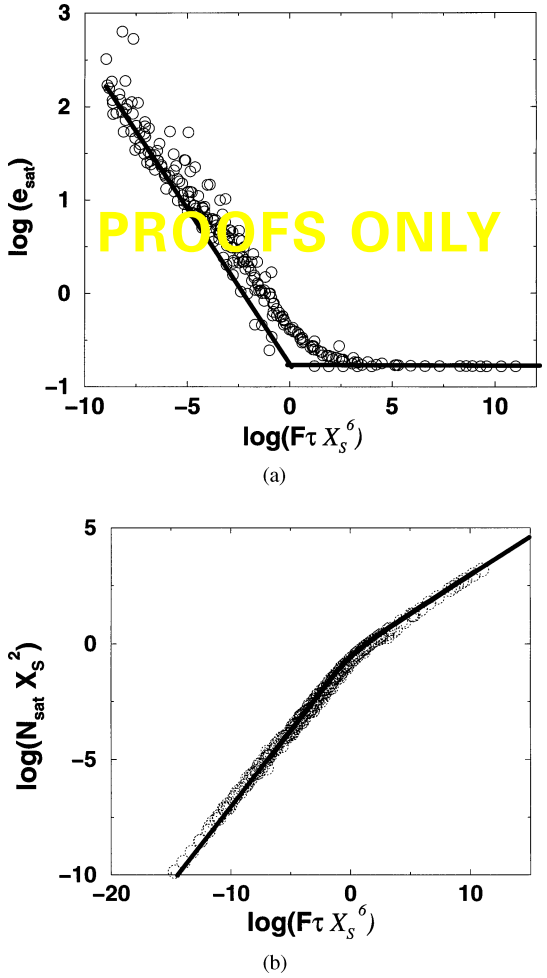

Figure 12. Values of (a) the thickness e_{sat} and (b) island density N_{sat} at the saturation of island density as a function of the evaporation parameter $\eta = F\tau X_S^6$ for growth with pure juxtaposition [119]. The solid lines represent theoretical predictions [119].

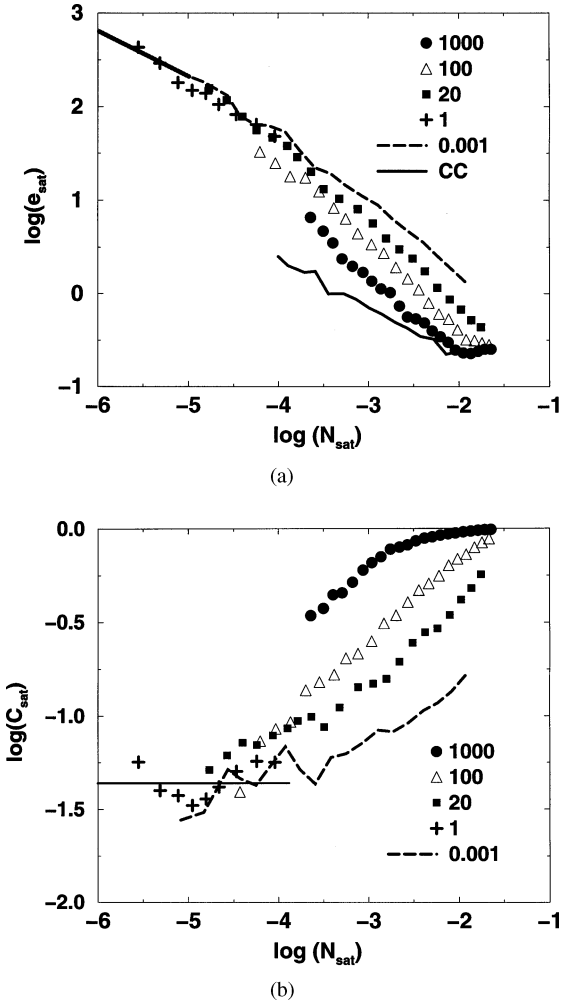

Figure 13. Values of the thickness e_{sat} (a) and the condensation coefficient C_{sat} (b) at the saturation of island density in the total coalescence limit (3D growth for atomic deposition). In the limit of low island densities (i.e., high evaporation rates), C_{sat} is a constant (see [136]; this regime is indicated by the solid line). However, there are crossover regimes which depend on the precise τ_e and which are shown here. Then, from a measure of C_{sat} and N_{sat} one can get an estimate for τ_e for the not too low island densities which correspond to many experimental cases. In the same spirit, (a) shows the evolution of e_{sat} as a function of N_{sat} in the crossover regime. The numbers correspond to the different τ_e/τ used for the simulations and CC refers to the case of complete condensation (no evaporation). The dotted line in the upper left shows the limiting regime $e_{sat} \sim N_{sat}^{-1/2}$.

many experimental situations, the limit of high evaporation is not reached and one "benefits" from (mathematical) crossover regimes where these quantities do depend on the precise values of τ_e. Figure 13 gives the evolutions of C_{sat} and e_{sat} as a function of N_{sat} for different values of τ_e and F. Then, knowing e_{sat} and N_{sat} leads to an estimation of τ_e from Figure 13a which can be confirmed with Figure 13b provided C_{sat} is known.

To conclude, let me note that a saturation thickness much smaller than 1 ML can also be attributed to island mobility. This is a subtle process and it is difficult to obtain any information on its importance. We note that interpreting data as not affected by island diffusion when it is actually present leads to errors on diffusion coefficients of one order of magnitude or more depending on the value of $F\tau$ (see Fig. 9). Finally, one should be careful in interpreting the N_t vs. thickness curves since most observations are not made in real time (as in the computer simulations) and there can be postdeposition evolutions (see for example [137] for such complications in the case of atomic deposition).

6. EXPERIMENTAL RESULTS

We review in this section the experimental results obtained these last years for low energy cluster deposition, mainly in the submonolayer regime. The scope is double: first, we want to give some examples on how to analyze experiments (as indicated in Section 5) and, second, we will show that from a comparison of experiments and models one can deduce important physical

quantities characterizing the interaction of a cluster with a surface (cluster diffusivity) and with another cluster (coalescence). The following can be read with profit by those interested only in atomic deposition as examples of interpretation since these elementary processes are relevant for some cases of atomic deposition. One should be careful that some mechanisms which are specific to atomic deposition (transient mobility, funnelling, ...) are not discussed here (see [138]). Also, growth without cluster diffusion has to be interpreted in the framework of the percolation model as indicated above [126].

Before analyzing experimental data, it is important to know how to make the connection between the units used in the programs and the experimental ones (see also Table 1). In the program, the unit length is the diameter of a cluster. In the experiments, it is therefore convenient to use as a surface unit the *site*, which is the projected surface of a cluster $\pi d^2/4$ where d is the mean *incident* cluster diameter. The flux is then expressed as the number of clusters reaching the surface per second per site (which is the same as ML/s) and the island density is given per site. The thickness is usually computed in cluster monolayers, obtained by multiplying the flux by the deposition time. The coverage—the ratio of the area covered by the supported islands over the total area—has to be measured on the micrographs.

6.1. A Simple Case: Sb_{2300} Clusters on Highly Oriented Pyrolitic Graphite

We start with the case of antimony clusters containing 2300 ($\pm$600) atoms deposited on highly oriented pyrolitic graphite (HOPG) since here the growth has been thoroughly investigated [117]. We first briefly present the experimental procedure and then the results and their interpretation in terms of elementary processes.

6.1.1. Experimental Procedure

As suggested in the preceding section, various samples are prepared for several film thicknesses, incident fluxes, and substrate temperatures. For films grown on HOPG, before deposition at room temperature, freshly cleaved graphite samples are annealed at 500 °C for 5 hours in the deposition chamber (where the pressure is $\simeq 10^{-7}$ Torr) in order to clean the surface. The main advantage of HOPG conveniently annealed is that its surface consists mainly of defect-free large terraces ($\simeq 1\,\mu$m) between steps. It is also relatively easy to observe these surfaces by electron or tunneling microscopy [117]. Therefore, deposition on HOPG is a good choice to illustrate the interplay between the different elementary processes which combine to lead to the growth. After transfer in air, the films are observed by transmission electron microscopy (TEM) (with JEOL 200CX or TOP CON electron microscopes operating at 100 kV in order to improve the contrast of the micrographs).

6.1.2. Results

Figure 14a shows a general view of the morphology of the antimony submonolayer film for $e = 0.14$ ML and $T_s = 353$ K. A detailed analysis [117] of this kind of micrograph shows that the ramified islands are formed by the juxtaposition of particles which have the same size distribution as the free clusters of the beam. From this, we can infer two important results. First, in the low energy deposition regime, clusters do not fragment upon landing on the substrate as indicated in the Introduction. Second, antimony clusters remain juxtaposed upon contact and do not coalesce to form larger particles (option (a) of Fig. 5).

From a qualitative point of view, Figure 14a also shows that the clusters are able to *move* on the surface. Indeed, since the free clusters are deposited at random positions on the substrate, it is clear that, in order to explain the aggregation of the clusters in those ramified islands, one has to admit that the clusters move on the surface. How can this motion be quantified? Can we admit that diffusion and pure juxtaposition are the only important physical phenomena at work here?

Figure 15a shows the evolution of the island density as a function of the deposited thickness. We see that the saturation island density N_{sat} is reached for $e \simeq 0.15$ ML. This indicates that evaporation or island diffusion is not important in this case. Therefore, we guess that the growth should be described by a simple combination of deposition, diffusion of the incident clusters, and juxtaposition. This has been confirmed in several ways. We only give three different confirmations, directing the reader to [117] for further details. First, a comparison of the experimental morphology and that predicted by models including only deposition, diffusion, and pure juxtaposition shows a very good agreement (Fig. 14b). Second, Figure 15b shows that the saturation island density accurately follows the prediction of the model when the flux

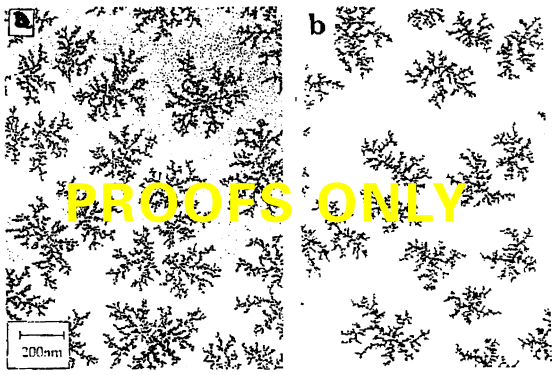

Figure 14. Typical island morphologies obtained experimentally by TEM (a) and from the computer simulations (b) at the same coverage. (a) Sb_{2300} deposition on graphite HOPG at $T_s = 353$ K and $f = 610^{-3}$ nm s^{-1}, corresponding to $F = 1.710^{-3}$ ML/s. The deposited thickness is 0.5 nm or $e = 0.14$ ML. (b) Model including only deposition, diffusion, and pure juxtaposition of the incident clusters, $F\tau = 9 \times 10^{-11}$.

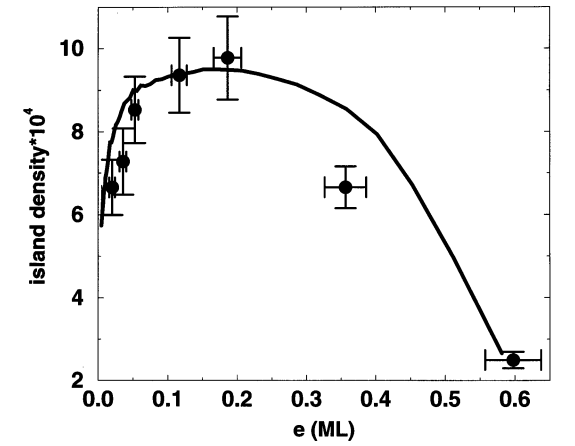

(a)

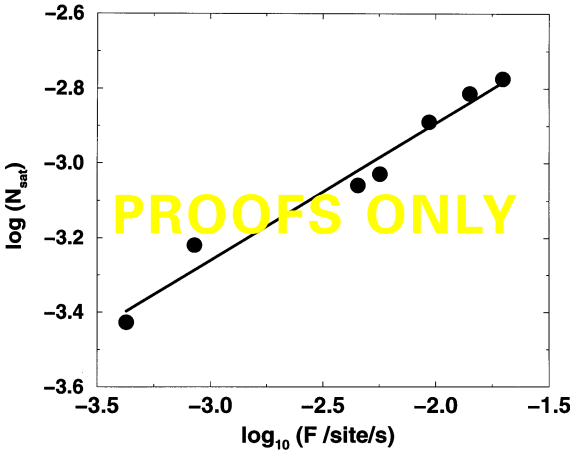

(b)

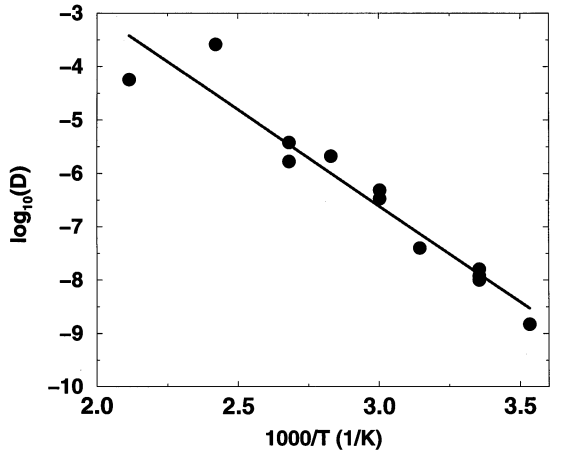

(c)

Figure 15. (a) Evolution of the island density as a function of the deposited thickness. The solid line is a fit to the experimental data with $F\tau = 1.75 \times 10^{-8}$. (b) Evolution of the maximum island density (N_{sat}) as a function of the incident flux F at room temperature. The solid line is a fit to the experimental data: we find $N_{sat} = af^{0.37\pm0.03}$. (c) Dependence of the diffusion coefficient on the temperature. From a fit on the experimental data (solid line), one finds $D = D_0 \exp(-E_a/kT)$, with $E_a = 0.7 \pm 0.1$ eV and $D_0 = 10^4$ cm^2 s^{-1}. The island densities are expressed *per site*, a site occupying the projected surface of a cluster, equivalent to 2.08×10^{-13} cm^2.

is varied. We recall that if the islands were nucleated on defects of the surface, the density would not be significantly affected by the flux.

Having carefully checked that the experiments are well described by the simple DDA model, we can confidently use Figure 9 to quantify the diffusion of the clusters. As detailed in [117], one first measures the saturation island density for different substrate temperatures. The normalized fluxes ($F\tau$) are obtained from Figure 9. Knowing the experimental fluxes, one can derive the diffusion times and coefficients. The result is a surprisingly high mobility of Sb_{2300} on graphite, with diffusion coefficients of the same order of magnitude as the atomic ones, that is, 10^{-8} cm^2 s^{-1} (Fig. 15c).

The magnitude of the diffusion coefficient is so high that we wondered whether there was any problem in the interpretation of the data, in spite of the very good agreement between experiments and growth models described above. For example, one could think of a linear diffusion of the incoming clusters, induced by the incident kinetic energy of the cluster in the beam (the cluster could "slide" on the graphite surface). This seems unrealistic for two reasons: first, in order to explain the low island density obtained in the experiments (see above), it should be assumed that the cluster, which has a low kinetic energy (less than 10 eV), can travel at least several thousand nanometers before being stopped by friction with the substrate. This would imply that the diffusion is just barely influenced by the substrate, which only slows down the cluster. In this case, it is difficult to explain the large changes observed in the island density when the substrate temperature varies. Second, we have deposited antimony clusters on a graphite substrate tilted 30° from its usual position (i.e., perpendicular to the beam axis). Then, a linear diffusion of the antimony clusters arising from their incident kinetic energy would lead to anisotropic islands (they would grow differently in the direction of tilt and its perpendicular). Experiments [117] show that there is no difference between usual and tilted deposits. Therefore we can confidently believe that Sb_{2300} clusters perform a very rapid Brownian motion on graphite surfaces. A similar study has been carried out for Sb_{250} on graphite, showing the same order of magnitude for the mobility of the clusters [117]. The microscopic mechanisms that could explain such a motion will be presented in Section 7.

6.2. Other Experiments

In this section, we try to analyze data obtained in previous studies [64, 139]. We provide *possible* (i.e., not in contradiction with any of the data) explanations, with the respective values of the microscopic processes. We stress that the scope here is not to make precise fits of the data but rather to identify the microscopic processes at work and obtain good guesses about their respective values.

6.2.1. Sb_{36} on a-C

Small antimony clusters are able to move on amorphous carbon, as demonstrated by Figure 16 and by the fact that the films are dramatically affected by changing the incident flux [139].

Figure 16a shows that these small clusters gather in large islands and coalesce upon contact. The island density is shown in Figure 16b. The maximum is reached for a very high thickness ($e \simeq 1.8$ ML), which can only be explained by supposing that there is significant reevaporation of Sb_{36} clusters from the surface. Evaporation of small antimony clusters (Sb_n with $n \leq 100$) from *a*-C substrates has also been suggested by other authors [20]. A fit using $\tau_e = 20$ deduced from Figure 13a gives $F\tau = 10^{-5}$ for $F = 6 \times 10^{-3}$ clusters site^{-1} s^{-1}, leading to $\tau \sim 2 \times 10^{-3}$ s, $D = 2 \times 10^{-12}$ cm^2/s, $\tau_e = 0.04$ s, and $X_S \sim 6$ nm before evaporation, and a condensation coefficient of 0.2 when the maximum island density is reached. However, some authors have argued [19] that the condensation coefficient is not so low. It is interesting to try a different fit of the data—in better agreement with this indication—to give an idea of the uncertainties of the fits. For this, we assume that the deposited islands are spherical (solid line of Fig. 16b) by the procedure described in Section 4. Here we have taken $F\tau = 3 \times 10^{-6}$ for $f = 6 \times 10^{-3}$ clusters/site^{-1} s^{-1}, leading to $\tau \sim 5 \times 10^{-4}$ s, $\tau_e =$ 0.04 s corresponding to $D = 8 \times 10^{-12}$cm^2/s, and $X_S \sim 11$ nm before evaporation, and a condensation coefficient of 0.5 when the maximum island density is reached. Note that the condensation coefficient is, as expected, higher than in the previous fit and that the agreement with the experimental island densities for the lowest thicknesses is better. Comparing the two fits, it can be seen that the difference in the diffusion coefficient is a factor of 4, and a factor 2 in the X_S. This means that the orders of magnitude of the values for the microscopic mechanisms can be trusted despite the lack of comprehensive experimental investigation.

Similar studies [204] have allowed one to obtain the diffusion and evaporation characteristic times for other clusters deposited on amorphous carbon. For Bi_{90}, one finds $D \sim 3 \times 10^{-13}$cm^2 s^{-1} and $X_S \sim 8$ nm and for In_{100}, $D \simeq 4 \times 10^{-15}$ cm^2 s^{-1} and strong coalescence (the incident clusters are liquid).

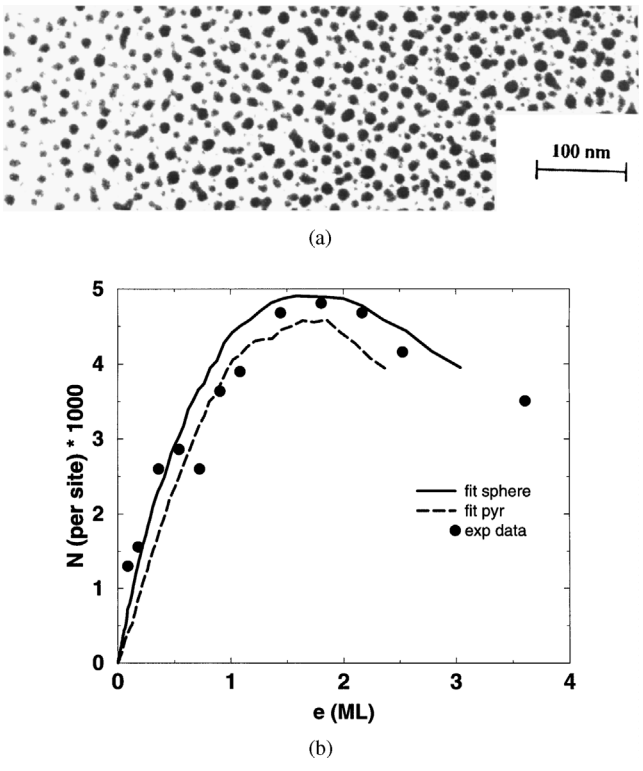

Figure 16. Morphology of a Sb_{36} film at $e = 1.8$ ML. (b) Evolution of the island density (per site) as a function of thickness (ML). The dashed line represents a fit of the data with $F\tau = 10^{-5}$ assuming a pyramidal (half-sphere) shape for the supported islands, while the solid line assumes that islands are spherical and $F\tau = 3 \times 10^{-6}$.

6.2.2. Au_{250} on Graphite

Figure 17 shows the morphology of a gold submonolayer film obtained by deposition of Au_{250} (± 100) clusters

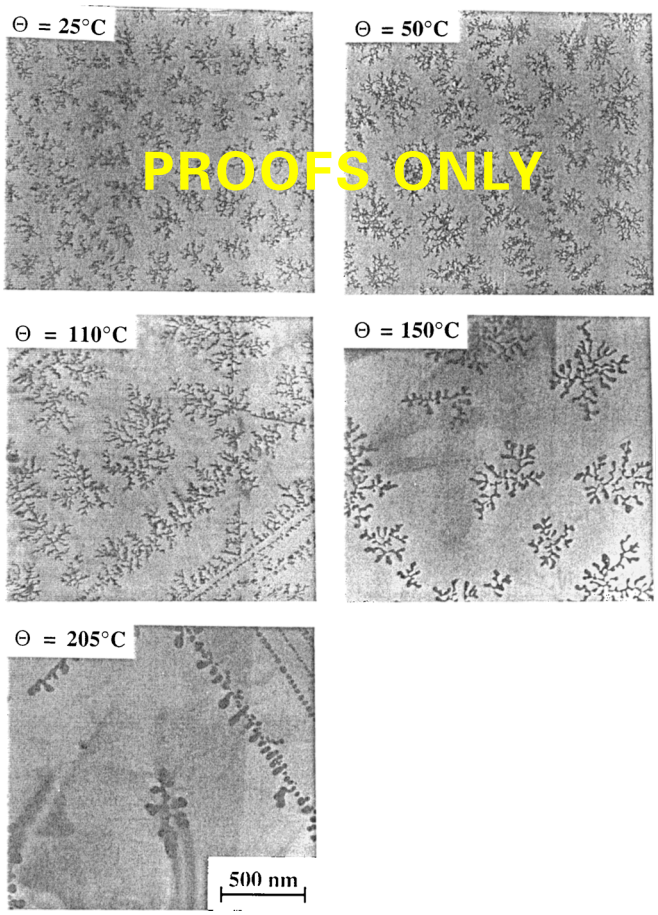

Figure 17. Morphologies of a Au_{250} films at $e = 0.12$ ML and increasing temperatures as indicated in the micrographs. There are less and less islands as the substrate temperature is raised and the islands become more and more compact.

prepared by a laser vaporization source on graphite in an UHV chamber for different substrate temperatures.

The structures are strikingly similar to those obtained in the Sb_{2300} case: large, ramified islands. We can conclude that Au_{250} clusters do move on graphite and that they do not completely coalesce. A more careful examination of the island morphology indicates that the size of the branches is not the same as the size of the incident clusters, as was the case for Sb_{2300}. Here the branches are larger, meaning that there is a partial coalescence, limited by the *kinetics* of the growth. This is a very interesting experimental test for coalescence models that are presented later. We first try to estimate the diffusion coefficient of the gold clusters. We have to be careful here because the incident flux is *chopped* with the laser frequency, roughly 10 Hz. The active portion of the period (i.e., when the flux is "on") is $\simeq 100\,\mu$s.

A general analysis of the growth in presence of a chopped flux has been reported elsewhere [118, 140]. Adapting this analysis to the case of gold clusters, and with the help of MD simulations using realistic potentials, it has been shown [141] that the experimental island densities imply that islands containing as much as 100 clusters are able to diffuse on graphite. The diffusion coefficient for an isolated cluster is estimated to be about 10^{-5} cm^2 s^{-1} at 500 K. The fact that such large islands (containing up to 25000 atoms) are able to diffuse is not as unreasonable as it may appear at first sight since the incident clusters do significantly coalesce, up to those sizes, and we expect spherical islands to move [165].

Very recently, we have shown [142] that substrates presenting ordered defects can be used to grow ordered arrays of nanostructures (Fig. 18).

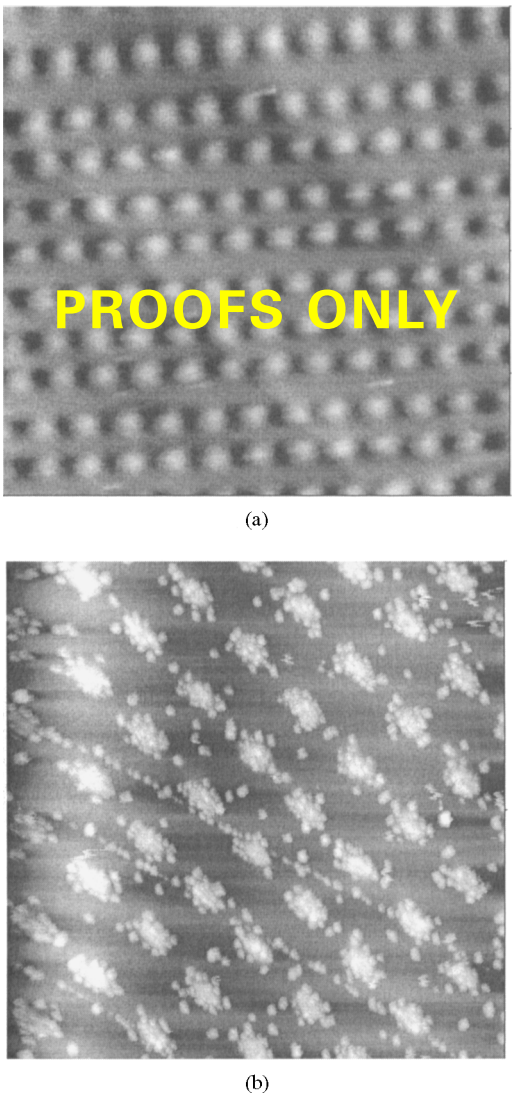

Figure 18. AFM image of an ordered array of defects—separated by 100 nm—on HOPG (a) and of the obtained array of gold nanostructures by cluster deposition (b). The defects are obtained by the focused ion beam technique at the LPN Laboratory (Bagneux, France) using 30 keV Ga^+ ions. The bottom image has been obtained by depositing gold clusters containing 750 atoms (diameter 2.8 nm) at 300 K on a HOPG substrate previously prepared with defects separated by 300 nm.

6.2.3. Au_{250} on NaCl

Given the surprisingly high mobility of Au_{250} ($\pm$100) on HOPG, it was worth testing gold cluster mobility on other substrates. We present here recent results obtained by depositing Au_{250} clusters on NaCl [143]. The high island density (Fig. 19a) shows that gold clusters are not very mobile on this substrate, with an upper limit on the diffusion coefficient of $D \simeq 10^{-15}$ cm^2/s. This is in agreement with the low mobilities observed by other authors [144] in the 1970s. The diffraction pattern (Fig. 19b) is similar to that obtained in Figure 15c and d of [144]. The authors interpreted their results with the presence of multitwinned Au particles with two epitaxial orientations: Au(111)/NaCl(100) and Au(100)/NaCl(100). This is reasonable taking into account the interatomic distances for these orientations: $d_{\mathrm{Au\,Au(111)}} = 0.289$ nm, $d_{\mathrm{NaCl(100)}} = 0.282$ nm, and $d_{\mathrm{Au\,Au(100)}} = 0.408$ nm, $1/2d_{\mathrm{NaCl(100)}} = 0.398$ nm (along the face diagonal). These preliminary results suggest that epitaxy may prevent clusters from moving rapidly on a surface, a result which has also been observed by other groups (see the next section). They also show that, at least in this case, forming the clusters on the surface by atomic aggregation or depositing preformed clusters does not change the orientation nor the diffusion of the clusters on the surface. Work is in progress to determine the precise atomic structure of the clusters, their orientation on the substrate, and their diffusion at higher temperatures [143].

7. TOWARD A PICTURE OF CLUSTER DIFFUSION AND COALESCENCE AT THE ATOMIC SCALE

In the preceding sections we have tried to analyze the growth with the help of two main ingredients: diffusion of the clusters on the surface and their interaction. We have taken the diffusion as just one number quantifying

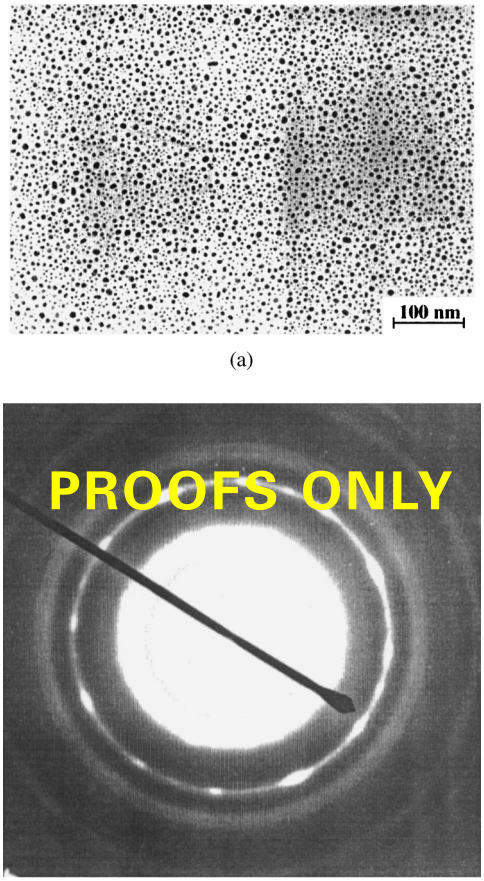

Figure 19. Morphology (a) and diffraction pattern (b) of a Au_{250} submonolayer deposit on NaCl at $e = 0.12$ ML. The supported islands are small (mean diameter $\simeq$ 5nm) and in epitaxy with the substrate as shown by the diffraction pattern.

the cluster motion, without worrying about the microscopic mechanisms which could explain it. For *atomic* diffusion, these mechanisms have been extensively studied [29, 138, 145] and are relatively well known. In the (simplest) case of compact (111) flat surfaces, diffusion occurs by site to site jumps over bridge sites (the transition state). Therefore, diffusion is an activated process and plotting the diffusion constant vs. the temperature yields the height of the barrier, which gives information about the microscopics of diffusion. This kind of simple interpretation is not valid for *cluster* diffusion. It is always possible to infer an "activation" energy from an Arrhenius plot (see Fig. 15c) but the meaning of this energy is not clear since the precise microscopic diffusion mechanism is unknown.

Similarly, cluster–cluster coalescence (Fig. 5) has been supposed to be total or null (i.e., pure juxtaposition) but without considering the kinetics nor the intermediate cases which can arise (see the experimental results for gold on graphite for example).

In this section, we describe some preliminary results which can shed some light on the microscopic mechanisms leading to cluster diffusion or coalescence.

7.1. Diffusion of the Clusters

Before turning to the possible microscopic mechanisms, one must investigate whether cluster diffusion is indeed such a general phenomenon. Let us review now the available experimental data concerning the diffusion of 3D clusters. We already presented in the previous section several examples of high cluster mobilities over surfaces. In the case of Sb_{2300} on graphite, mobilities as high as $D = 10^{-8}$ cm^2 s^{-1} are obtained at room temperature, and similar values can be inferred for Ag cluster deposition [63, 64]. On *a*-C substrates, diffusion is not that rapid but has to be taken into account to understand the growth. More than 20 years ago, a group at Marseille University [133, 144, 146, 147] carefully studied the mobility of nanometer-size gold crystallites on ionic substrates (MgO, KCl, NaCl). By three different methods, they proved that these 3D clusters—grown by atomic deposition at room temperature—are significantly mobile at moderately high temperatures ($T \sim$ 350 K). The three different methods were direct observation under the electron microscope beam [146], comparison of abrupt concentration profiles [144], or the radial distribution functions [133] before and after annealing. All these results are carefully reviewed in [147], which shows that gold clusters move as an entity on KCl(100) at 350 K, since the conservation of the size distribution rules out atomic exchange between islands [the evaporation–condensation (EC) mechanism presented below (Section 7.1.1)]. From the shape of the radial distribution function some features of the cluster–cluster interaction could be derived, mainly that it is a *repulsive* interaction. The detailed interaction mechanisms are not clear [133, 147]. A different study [144] showed that the clusters were mobile only for a limited amount of time (several minutes) and then stopped. It turns out that clusters stop as soon as they reach epitaxial orientation on the substrate. Indeed, the gold(111) planes can orient on the KCl(100) surface, reaching a stable, minimum energy configuration (for more details on the epitaxial orientations of gold clusters on NaCl, see [148, 149]). Therefore, 3D cluster diffusion might be quite a common phenomenon, at least when there is no epitaxy between the clusters and the substrate.

What are the possible microscopic mechanisms? Unfortunately for the field of cluster *deposition*, recent theoretical and experimental work has focused mainly on one atom thick, two-dimensional islands, whose diffusion mechanisms might be different from those of 3D islands. The focus on 2D islands is due to the technological impetus provided by applications of atomic deposition—notably MBE for which one wants to achieve flat layers.

Let us briefly review the current state of the understanding of 2D island diffusion to see what inspiration we can draw for 3D cluster diffusion.

7.1.1. 2D Island Diffusion Mechanisms

There are two main types of mechanisms proposed to account for 2D island diffusion: single adatom motion and collective (simultaneous) atom motion. It should be noted that small islands (less than ~ 15 atoms) are likely to move by specific mechanisms, depending on the details of the island geometry and atomic energy barriers [150–152]. Therefore we concentrate here on larger 2D islands.

Individual Mechanisms The most common mechanism invoked to account for 2D island diffusion has been that of individual atomic motion. By individual we mean that the movement of the whole island can be decomposed in the motion of *uncorrelated* single atom moves. There are two main examples of such a diffusion: evaporation–condensation and periphery diffusion (PD). Theoretical investigations on these individual mechanisms have generated much interest since it was conjectured that this diffusion constant D_{ind} is proportional to the island number of atoms (island mass) to some power which depends on the precise mechanism (EC or PD) causing island diffusion but not on temperature or the chemical nature of the system. If true, this conjecture would prove very useful, for it would allow one to determine experimentally the mechanism causing island migration by measuring the exponent and some details of the atom diffusion energetics by measuring how D_{ind} depends on temperature. Unfortunately, recent studies have shown that this prediction is too simplistic, as we show now for the two different mechanisms.

Periphery Diffusion Figure 20 shows the elementary mechanism leading to island diffusion via atomic motion on the edge of the island (labeled PD). Assuming [107]:

- Each atomic jump displaces the center of mass of the island by a distance of order $1/N$ (where N is the number of atoms of the island).
- Each edge atom (density n_s) jumps with a rate $k \sim \exp(-E_{ed}/k_B T)$ where E_{ed} is the activation energy for jumping from site to site along the border and k_B is Boltzmann constant.

One obtains [107]

$$D_{\text{ind}} \sim k n_s 1/N^2 \sim \exp(-E_{ed}/k_B T) N^{-3/2} \qquad (1)$$

if one postulates that n_s, the mean concentration of edge atoms, is proportional to the perimeter of the island (i.e., to $N^{1/2}$). This equation allows one in principle to determine the edge activation energy by measuring the temperature dependence of D_{ind}.

However, recent experiments [154] and kinetic Monte Carlo simulations [84, 107, 153, 155] have suggested that

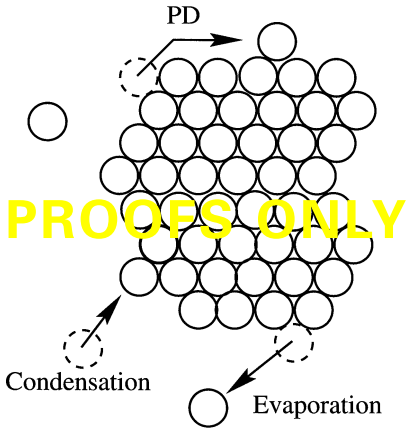

Figure 20. Individual atomic mechanisms leading to island diffusion. PD refers to diffusion of atoms on the periphery of the island, while the exchange of atoms between the island and the atomic 2D gas is shown by the condensation and evaporation labels. The dashed circles represent the old positions of the atoms, while the continuous circles represent the new positions, after the elementary process.

Eq. (1) is wrong. First, the size exponent is not universal but depends on the precise energy barriers for atomic motion (and therefore on the chemical nature of the material) and, second, the measured activation energy does not correspond to the atomic edge diffusion energy. The point is that the limiting mechanism for island diffusion is *corner* breaking, for islands would not move over long distances simply by edge diffusion of the outer atoms [107]. Further studies are needed to fully understand and quantify the PD mechanism.

Evaporation–Condensation An alternative route to diffusion is by exchange of atoms between the island and a 2D atomic gas. This is the usual mechanism leading to Ostwald ripening [156]. Atoms can randomly evaporate from the island and atoms belonging to the 2D gas can condensate on it (Fig. 20). This leads to fluctuations in the position of the island center of mass which are difficult to quantify because of the possible *correlations* in the atomic evaporation and condensation. Indeed, an atom which has just evaporated from an island is likely to condensate on it again, which cannot be accounted by a mean-field theory of island gas exchange of atoms [157]. The latter leads to a diffusion coefficient scaling as the inverse radius of the island [158], while correlations cause a slowing down of diffusion, which scales as the inverse *square* radius of the island [110, 155, 157].

Experimentally, Wen et al. [158] have observed by scanning tunneling microscopy (STM) the movement of Ag 2D islands on Ag(100) surfaces. They measured a diffusivity almost independent of the island size, which rules out the PD mechanism and roughly agrees with their [158] calculation of the size dependence of the EC mechanism. Since this calculation has been shown to be only approximate, further theoretical and experimental work is needed to clarify the role of EC in 2D island diffusion.

However, the work by Wen et al. [158] has convincingly shown that these islands move significantly and that, for silver, island diffusion is the main route to the evolution of the island size distribution, contrary to what was usually assumed (Ostwald ripening exclusively due to atom exchange between islands, via atom diffusion on the substrate).

Collective Diffusion Mechanisms These individual mechanisms lead in general to relatively slow diffusion of the islands (of order $10^{-17}\text{cm}^2/\text{s}$ at room temperature [158]). For small clusters, different (and faster) mechanisms such as dimer shearing, involving the simultaneous displacement of a dimer, have been proposed [159]. More generally, Hamilton et al. [160] have proposed a different mechanism, also involving *collective* motions of the atoms, which leads to *fast* island motion. By collective we mean that island motion is due to a simultaneous (correlated) motion of (at least) several atoms of the island.

Specifically, Hamilton et al. [160] proposed that *dislocation* motion could cause rapid diffusion of relatively small (5 to 50 atoms) *homoepitaxial* islands on face-centered-cubic (fcc)(111) surfaces. The basic idea is that a row of atoms moves simultaneously from fcc to hexagonal close-packed (hcp) sites, thus allowing the motion of the dislocation and consequently of the island center of mass. Alternative possibilities suggested by Hamilton et al. for dislocation mediated island motion are the "kink" mechanism (the same atomic row moves by *sequential* but correlated atomic motion) or the "gliding" mechanism studied below, where *all* the atoms of the island move simultaneously. Molecular dynamics simulations together with a simple analytical approach [160] suggest that for the smallest islands ($N < 20$) the gliding mechanism is favored, for intermediate sizes ($20 < N < 100$) the dislocation motion has the lowest activation energy, while for the largest studied islands ($N > 100$) the preferential mechanism is that of "kink" dislocation motion. It is interesting to quote at this point recent direct observations of cluster motion by field ion microscopy [161]. By a careful study, the authors have ruled out the individual atomic mechanisms discussed above as well as the dislocation mechanism. Instead, they suggest that gliding of the cluster as a whole is likely to explain the observed motion [161].

Hamilton later studied the case of *heteroepitaxial*, strained islands [162]. He has shown that—due to the misfit between the substrate and the island structures—there can exist islands for which introducing a dislocation does not cost too much extra energy. These metastable misfit dislocations would propagate easily within the islands, leading to "magic" island sizes with a very high mobility [162].

7.1.2. 3D Island Diffusion Mechanisms

For 3D clusters, the three microscopic mechanisms presented above are possible in principle. However, as noted above, the individual atom mechanisms lead to a diffusivity smaller than the diffusion of Sb_{2300} on graphite by several orders of magnitude. These mechanisms have also been ruled out for the diffusion of gold crystallites on ionic substrates [147]. Several tentative explanations based on the gliding of the cluster as a whole over the substrate have been proposed [147]. Reiss [163] showed that, for a *rigid* crystallite which is not in epitaxy on the substrate, the activation energy for rotations might be weak, simply because during a rotation, the energy needed by atoms that have to climb up a barrier is partially offset by the atoms going into more stable positions. Therefore, the barrier for island diffusion is of the same order as that for an atom, as long as the island does not reach an epitaxial orientation. Kern et al. [147, 164] allowed for a partial rearrangement of the interface between the island and the substrate when there is a misfit. The interface would be composed of periodically disposed zones in registry with the substrate, surrounded with perturbed ("amorphous") zones, weakly bound to the substrate. This theory—similar in spirit to the dislocation theory proposed by Hamilton [160, 162] for 2D islands—leads to reasonable predictions [147] but is difficult to test quantitatively.

To clarify the microscopic mechanisms of 3D cluster diffusion, we now present in detail MD studies carried out recently [165]. These simulations aimed at clarifying the generic aspects of the question rather than modeling a particular case. Both the cluster and the substrate are made up of Lennard-Jones atoms [166], interacting through potentials of the form

$$V(r) = 4\epsilon\left(\left(\frac{\sigma}{r}\right)^{12} - \left(\frac{\sigma}{r}\right)^{6}\right).$$

Empirical potentials of this type, originally developed for the description of inert gases, are now commonly used to model generic properties of condensed systems. Lennard-Jones potentials include only pair atom–atom interaction and ensure a repulsive interaction at small atomic distances and an attractive interaction at longer distances, the distance scale being fixed by σ and the energy scale by ϵ. For a more detailed discussion of the different interatomic potentials available for MD simulations and their respective advantages and limitations, see [167]. The substrate is modeled by a single layer of atoms on a triangular lattice, attached to their equilibrium sites by weak harmonic springs that preserve surface cohesion. The Lennard-Jones parameters for cluster atoms, substrate atoms, and the interaction between the substrate and the cluster atoms are respectively $(\epsilon_{cc}, \sigma_{cc})$, $(\epsilon_{ss}, \sigma_{ss})$, and $(\epsilon_{sc}, \sigma_{sc})$. ϵ_{cc} and σ_{cc} are used as units of energy and length. ϵ_{sc}, σ_{ss}, and T, the temperature of the substrate, are the control parameters of the simulation. The last two parameters are then constructed by following the standard combination rules: $\epsilon_{ss} = \sigma_{ss}^6$ and $\sigma_{sc} = \frac{1}{2}(\sigma_{cc} + \sigma_{ss})$.

Finally, the unit of time is defined as $\tau = (M\sigma_{cc}^2/\epsilon_{cc})^{1/2}$, where M is the mass of the atoms which is identical for cluster and substrate atoms. The simulation uses a standard molecular dynamics technique with thermostatting of the *surface* temperature [168].

In these simulations, the clusters take the spherical cap shape of a solid droplet (Fig. 21) partially wetting the substrate. The contact angle, which can be defined following reference [169], is roughly independent of the cluster size (characterized by its number of atoms n, for $50 < n < 500$). This angle can be tuned by changing the cluster–substrate interaction. For large enough ϵ_{sc}, total wetting is observed. The results presented below have been obtained at a reduced temperature of 0.3 for which the cluster is solid. This is clearly visible in Figure 21, where the upper and lower halves of the cluster, colored white and grey at the beginning of the run, clearly retain their identity after the cluster *center of mass* has moved over three lattice parameters. Hence the cluster motion appears to be controlled by *collective* motions of the cluster as a whole rather than by single atomic jumps.

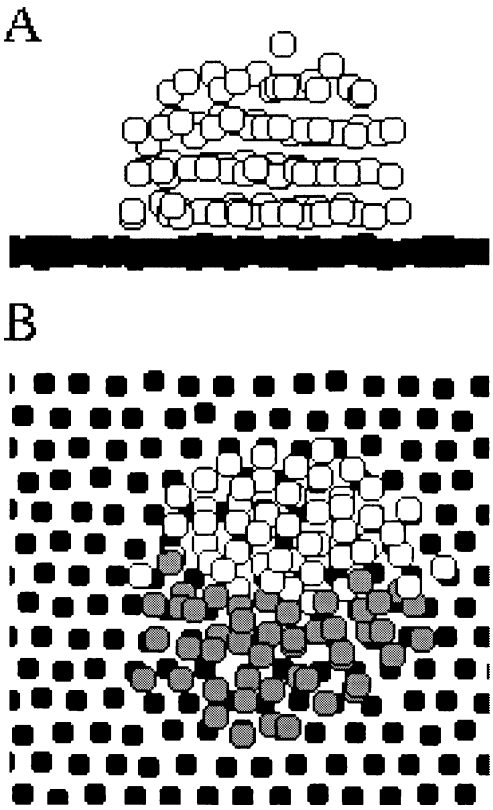

Figure 21. Configuration of the Lennard-Jones cluster on the crystalline surface. (A) Side view: The cluster is partially wetting the surface. (B) Top view: The two halves of the cluster have been colored at the beginning of the run. After the cluster center of mass has moved by roughly three substrate lattice constants from its original position, the two parts of the cluster are still well distinct. Then, the cluster diffusion cannot be explained in terms of single atom mechanisms ($n = 100$, $\sigma_{ss} = 0.7$, $\epsilon_{sc} = 0.4$, $T = 0.3$).

The MD simulations have confirmed that one of the most important parameters for determining the cluster diffusion constant is the ratio of the cluster lattice parameter to the substrate lattice parameter. The results for the diffusion coefficient are shown in Figure 22a. When the substrate and cluster are commensurate ($\sigma_{ss} = \sigma_{cc} \equiv 1$), the cluster can lock into a low energy epitaxial configuration. A global translation of the cluster would imply overcoming an energy barrier scaling as $n^{2/3}$, the contact area between the cluster and the substrate. In that case diffusion will be very slow, unobservable on the time scale of the MD simulations. What is interesting to note is that even small deviations from this commensurate case lead to a measurable diffusion on the time scale of the

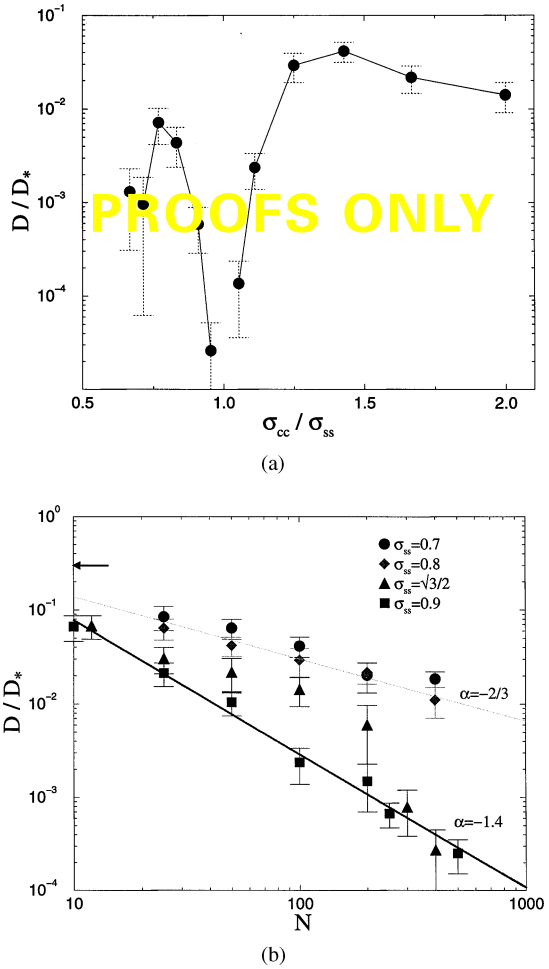

Figure 22. (a) Dependence of the diffusion coefficient on the mismatch between the lattice parameter of the substrate and the cluster. A small change in the lattice parameter of the cluster leads to a huge change in the diffusivity ($n = 100$, $\epsilon_{sc} = 0.4$, $T = 0.3$, run length = 12500 τ). (b) Dependence of the diffusion coefficient of a cluster as a function of its number of atoms. Data correspond to different mismatches between the cluster and the substrate lattice parameters. The diffusion coefficient decreases as a power law with exponent α. The two different slopes correspond to different diffusion regimes: the weaker dependence corresponds to a Brownian trajectory; the stronger correspond to a "hoppinglike" diffusion. For comparison, the arrow indicates the diffusion coefficient of a single adatom with $\sigma_{ss} = 0.9$.

MD runs. This can be understood from the fact that the effective potential in which the center of mass moves is much weaker, as the cluster atoms, constrained to their lattice sites inside the rigid solid cluster, are unable to adjust to the substrate potential (see above, Reiss model [163]). The effect is rather spectacular: a 10% change on the lattice parameter induces an increase of the diffusion coefficient by several orders of magnitude.

Finally, we show in Figure 22b the effect of cluster size on the diffusion constant for different lattice parameter values. As the number n of atoms in the cluster is varied between $n = 10$ and $n = 500$, the diffusion constant decreases, roughly following a power law $D \sim n^{\alpha}$. This power law exponent α depends significantly on the mismatch between the cluster and the substrate lattice parameters. For high mismatches ($\sigma_{ss} = 0.7, 0.8$), α is close to -0.66. As the diffusion constant is inversely proportional to the cluster–substrate friction coefficient, this result is in agreement with a simple "surface of contact" argument yielding $D \sim n^{-2/3}$. On the other hand, when the lattice mismatch is equal to 0.9, one obtains $\alpha \approx -1.4$, although the shape of the cluster, characterized by the contact angle, does not appreciably change. It is instructive to follow the trajectory followed by the cluster center of mass (Fig. 23). In the runs with a large mismatch (Fig. 23a), this trajectory is "Brownianlike," with no apparent influence of the substrate. This is consistent with the simple "surface of contact" argument. Instead, when the mismatch is small (Fig. 23b), the center of mass of the cluster follows a "hoppinglike" trajectory, jumping from site to site on the honeycomb lattice defined by the substrate. When $\sigma_{ss} = \sqrt{3}/2$, there seems to be a transition between the two regimes around $n = 200$.

It is interesting to consider the interpretation of cluster motion in terms of dislocation displacement within the cluster, a mechanism which has been proposed to explain rapid 2D cluster diffusion [160, 162] (see the discussion in Section 7.1.1). For this, one can "freeze" the internal degrees of freedom of the cluster deposited on a thermalized substrate. The center of mass trajectory is integrated using the quaternion algorithm [165, 168]. Surprisingly, the diffusion constant follows the same power law as in the free cluster case [165]. This result proves that the diffusion mechanism in this case cannot be simply explained in terms of dislocation migration within the cluster as proposed to explain the diffusion of 2D islands in [160, 162]. As the substrate atoms are tethered to their lattice site, strong elastic deformations or dislocations within the lattice are also excluded. Hence, the motor for diffusion is here the vibrational motion of the substrate, and its efficiency appears to be comparable to that of the internal cluster modes.

Very recently, U. Landmann performed MD simulations of diffusion of large gold clusters on HOPG substrates [170]. He finds high cluster mobility, in agreement with the preceding simulations. His studies show

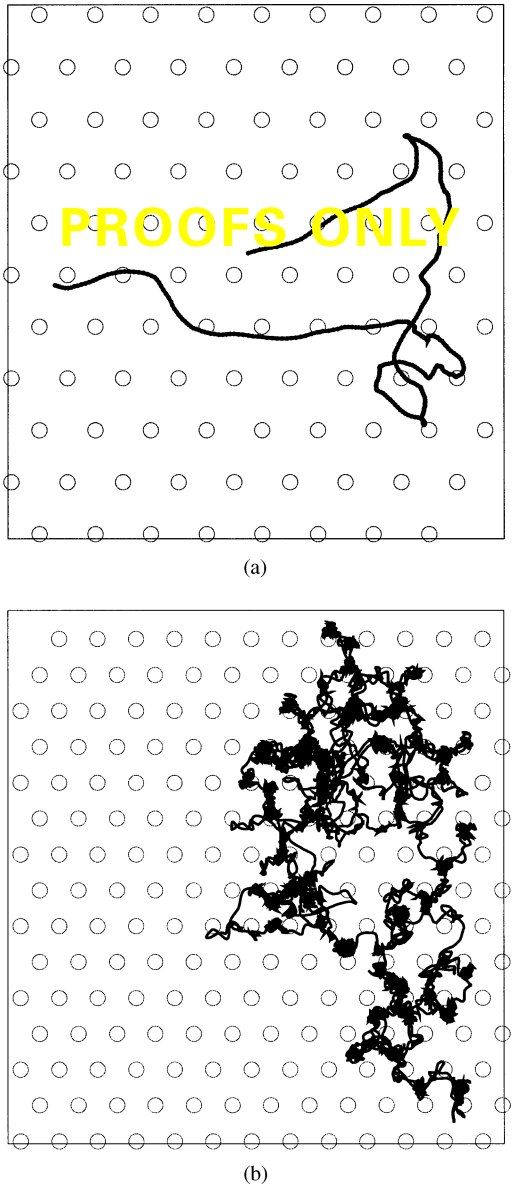

Figure 23. Trajectory of a cluster center of mass diffusing on a substrate. The solid line represents the trajectory and the circles the equilibrium position of the surface atoms. (a) Large mismatch: the motion is "Brownianlike" (i.e., the cluster does not "see" the structure of the surface). The values of the parameters are $\epsilon_{sc} = 0.4$, $\sigma_{ss} = 0.7$, $T = 0.3$, $n = 100$. (b) Small mismatch: the cluster center of mass jumps from one hexagon center to a nearest neighbor one. The values of the parameters are the same as for (a) except for $\sigma_{ss} = 0.9$.

that cluster diffusion in this case proceeds by two different mechanisms: long (several cluster diameters) linear "flights" separated by relatively slow diffusive motion as observed in the preceding simulations. Further work is needed to ascertain the atomic mechanisms leading to this kind of motion.

7.1.3. Discussion

What are the (partial) conclusions which can be drawn from these studies of cluster diffusion? We think that the

main parameter determining the mobility of 3D islands on a substrate is the possible epitaxy of the cluster on the substrate. Indeed, if the island reaches an epitaxial orientation, it is likely to have a mobility limited by the individual atomic movements, which give a small diffusion constant (of order 10^{-17} cm^2 s^{-1} at room temperature). Diffusivities of this magnitude will not affect the growth of cluster films during typical deposition times, and clusters can be considered immobile. The effect of these kind of diffusion rates can only be seen by annealing the substrates at higher temperatures or for long times. According to Hamilton [160], dislocations could propagate even for epitaxial islands, but it is likely that this mechanism is more important in the case of heteroepitaxial islands which we now proceed to discuss. Indeed, if the island is not in epitaxy on the substrate, high mobilities can be observed because the cluster sees a potential profile which is not very different from that seen by a single atom. It should be noted that this nonepitaxy can be obtained when the two lattice parameters (of the substrate and the island) are very different, or also when they are compatible if there is relative misorientation. The latter has been observed for gold on ionic substrates [147] and mobility is relatively high until the crystallites reach epitaxy. The MD simulations presented above show that, for Lennard-Jones potentials, only homoepitaxy prevents clusters from moving rapidly on a surface. It should be noted that relaxation of the cluster or the substrate—which would favor a locking of the cluster in an energetically favorable position at the expense of some elastic energy—has not been observed in these LJ simulations nor has dislocation propagation. This is probably realistic for low interaction energies which correspond to metal clusters on graphite. It could also be argued that dislocation motion is more difficult in 3D clusters than in 2D islands since the upper part of the particle (absent in 2D islands) tends to keep a fixed structure. Another important parameter is the cluster–substrate interaction: one can think that a large attractive interaction (for metal on metal systems for example) can induce an epitaxial orientation and prevent the cluster from diffusing, even in the heteroepitaxial case. The differences between the diffusion of clusters grown on a substrate by atom deposition and aggregation and those previously formed in a beam and deposited must also be investigated. One could anticipate that islands formed by atom aggregation *on* the substrate would accommodate easily to the substrate geometry, whereas preformed clusters might keep their (metastable) configuration. However, it is not at all clear that island nucleation and epitaxy are simultaneous phenomena, for it has been observed that islands can form in a somewhat arbitrary configuration and subsequently orient on the substrate after diffusion and rotation (see [147]).

7.2. Cluster–Cluster Coalescence

What happens when two clusters meet? If they remain simply juxtaposed, morphologies similar to Figure 14a are observed. In this case, the incident clusters have retained their original morphology, and the supported particles are identical to them, even if they are in contact with many others after cluster diffusion. It is clear, by looking for example at Figure 17, that in some experimental situations the supported islands are clearly larger than the incident clusters, indicating that some *coalescence* has taken place. How can one understand and predict the size of the supported particles? Which are the relevant microscopic parameters? This is an interesting question from the fundamental point of view, since it is not clear that the theoretical tools which have been developed to deal with the kinetic evolution of macroscopic objects (size larger than a micrometer) by Herring [191] and Mullins and Nichols [174] can be used at the nanometer scale. These equations, which are based on coarse-grained, continuous equations, lead to an equilibrium time t_{eq} which increases as the fourth power of the object linear size. For example, one could wonder whether sintering of ceramic or metallic nanopowders can be analyzed with these classic tools since it is not clear that macroscopic concepts such as curvature, chemical potential, etc., should retain their relevance when dealing with structures containing only few atoms. Studying the validity of the partial differential equations approach at various length scales and temperatures is important since this formalism is also used by experimentalists to interpret their data and by theoreticians as a black box to calculate the time evolution of different structures [14, 192–195].

We will first briefly examine the classical theory for sphere–sphere coalescence (i.e., ignoring the effect of the substrate) and then review recent molecular dynamics simulations which suggest that this classical theory may not be entirely satisfactory for nanoparticles.

7.2.1. Continuum Theory of Coalescence

The standard analysis of kinetics of sintering is due to Mullins and Nichols [173, 174]. The "motor" of the coalescence is the diffusion of *atoms* of the cluster (or island) surface from the regions of high curvature (where they have less neighbors and therefore are less bound) toward the regions of lower curvature. The precise equation for the atom flux is [174]

$$\vec{J}_s = -\frac{D_s \gamma \Omega \nu}{k_B T} \overrightarrow{\nabla_s K} \tag{2}$$

where D_s is the surface diffusion constant (supposed to be isotropic), γ is the surface energy (supposed to be isotropic too), Ω is the atomic volume, ν is the number of atoms per unit surface area, k_B is Boltzmann's constant, T is the temperature, and K is the surface curvature ($K = 1/R_1 + 1/R_2$) where R_1 and R_2 are the principal radii of curvature). For sphere–sphere coalescence,

an order of magnitude estimation of the shape changes induced by this flux is [174]

$$\frac{\partial n}{\partial t} \sim 2B\frac{\partial^2 K}{\partial s^2} \qquad (y = s = 0) \tag{3}$$

where dn is the outward normal distance traveled by a surface element during dt, s is the arc length, and $B = D_s\gamma\Omega^2\nu/k_BT$ (the z axis is taken as the axis of revolution). For this geometry, Eq. (3) becomes (Fig. 24)

$$\frac{\partial l}{\partial t} \sim \frac{B}{l^3}\left(1 - \frac{l}{R}\right) \tag{4}$$

where we have made an order of magnitude estimation of the second derivative of the curvature: $\partial K/\partial s \sim (K(R) - K(l))/l$ and similarly $\partial^2 K/\partial s^2 \sim (1 - l/R)/l^3$ (see Fig. 24). Integrating Eq. (4) leads to

$$l \sim (r^4 + 4Bt)^{1/4} \qquad \text{for } l \ll R \tag{5}$$

Equation (5) gives an estimation of the coalescence kinetics for two spheres of radius r and R.

7.2.2. *Island Morphology within the Continuum Approximation*

Now we can turn to the prediction of one of the essential characteristics of cluster films: the size of the supported particles. As we have already mentioned in the Introduction, the size of the nanoparticles controls many interesting properties of the films. Therefore, even an approximate result may be useful, and this is what we obtain in this section.

First Stages of Growth: Thin Films The experiments shown above demonstrate that the supported particles can have a variety of sizes, from that of the incident clusters (Sb_{2300}/HOPG, Section 6.1) up to many times this size (for example Au_{250}/HOPG, Section 6.2.2). To understand how the size of the supported particles is determined, one can look at a large circular island to which clusters are arriving by diffusion on the substrate (Fig. 24). There are two antagonist effects at play here. One is given by thermodynamics, which commands that the system should try to minimize its surface (free) energy. Therefore one expects the clusters touching an island to coalesce with it, leading to compact (spherical) domains. The other process, driving the system away from this minimization, is the continuous arrival of clusters on the island edge. This kinetic effect tends to form ramified islands. What is the result of this competition? Since there is a kinetically driven ramification process, it is essential to take into account the *kinetics* of cluster–cluster coalescence, as sketched in the previous section. We will use Eq. (5) even if it is only approximate to derive an upper limit for the size of the compact domains grown by cluster deposition. It is an *upper* limit since, as pointed out in the previous section, coalescence for facetted particles could be *slower* than predicted by Eq. (5), hence diminishing the actual size of these domains.

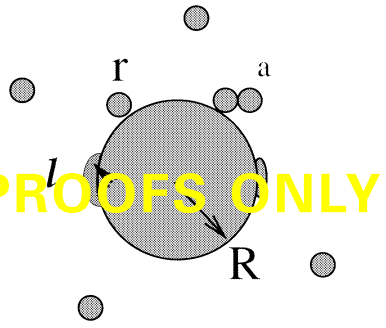

Figure 24. Schematic illustration of the competition between coalescence and kinetic ramification. R is the radius of the largest island, r is that of the incident clusters, and l stands for the typical length of a coalescing cluster. The label "a" refers to the ramification process when a cluster is touched by another one before coalescence can take place.

We first need an estimate of the kinetics of the second process: the impinging of clusters on the big island. A very simple argument is used here (see also [203] for a similar analysis for atomic growth): since the number of clusters reaching the surface is F per unit surface per second and the total number of islands is N_t per unit surface, each island receives on average a cluster every $t_r = N_t/F$.

We are now in a position to quantify the degree of coalescence in a given growth experiment. Let us suppose that a cluster touches a large island at $t = 0$. If no cluster impinges on the island before this cluster completely coalesces [in a time τ_c according to Eq. (5)], then the islands are compact (circular). Instead, if a cluster touches the previous cluster before its total coalescence has taken place, it will almost freeze up the coalescence of the previous cluster. The reason is that now the atoms on the (formerly) outer surface of the first cluster do not feel curvature since they have neighbors on the second cluster. The mobile atoms are now those of the second cluster (see Fig. 24, label a) and the coalescence takes a longer time to proceed (the atoms are farther from the big island). Then, if $t_r \ll \tau_c$, the islands formed on the surface are ramified. For intermediate cases, the size R_c of the compact domains can be estimated from Eq. (5) as $R_c = x(\tilde{t}_r)$ where $\tilde{t}_r$ takes into account the fact that, to freeze the coalescence of a previous cluster, one cluster has to touch the island at roughly the same point, $\tilde{t}_r \simeq t_r 2\pi R/r$, and

$$R_c^4 = r^4 + 4B\frac{2\pi R_c}{r}\frac{N_t}{F} \tag{6}$$

Equation (6) describes the limiting cases ($B \sim \infty$ or $B \sim 0$) correctly. The problem with the intermediate cases is to obtain a reliable estimate of the (average) atomic surface self-diffusion. For gold, Chang and Thiel

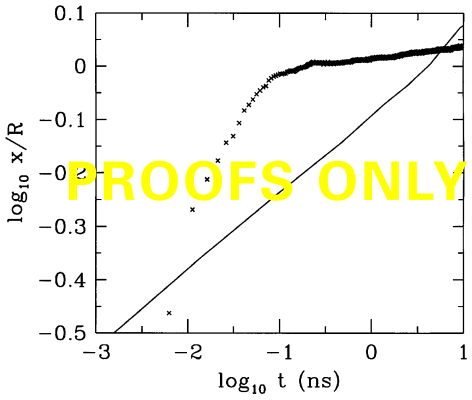

Figure 25. Approximate dependence of the radius of the supported particles R_c as a function of the substrate temperature for submonolayer and thick films. Lines refer to predictions from Eq. (6) with different incident cluster radii while symbols represent experimental results shown. The theoretical predictions for the submonolayer regime were obtained by taking $N_t/F = 0.1$ and using Eq. (7). For the thick film limit, we have taken $F = 10^{-3}$ ML/s and $r = 2.5$ nm [Eq. (8)]. One should consider these theoretical R_c values as an *upper* limit since coalescence may be much slower at these (nano)scales (see the text). As a consequence, it is no surprise that the predicted values are clearly larger than the experimental ones. Concerning Sb, the huge difference can come from a partial oxidation of the clusters on the substrate because of the relatively bad vacuum conditions (pressure $\sim 10^{-7}$ Torr). Even a thin oxide layer can decrease significantly atomic surface diffusion and transport, thus slowing the coalescence process.

[138] give values which vary between 0.02 eV on compact facets and 0.8 eV on more open surfaces. One solution is to go the other way around and estimate D_s from the experimental data and Eq. (6). From Figure 17, estimating R_c from the thickness of the island arms, and using the experimental values for r (0.85 nm) and the fact that since the flux is pulsed (see Section 6.2.2), the time between two successive arrivals of clusters is approximately the time between two pulses (0.1 s), and not N_t/F, one obtains $D_s \simeq 3 \times 10^{-3}\ \mathrm{cm^2\,s^{-1}} \exp(-0.69\ \mathrm{eV}/(k_B T))$, which seems a sensible value.

Despite the difficulty of defining average diffusion coefficients, one can use Eq. (6) to obtain a reasonable guess for the size of the compact domains by assuming that D_s is thermally activated: $D_s(T) = D_0 \exp(-E_a/(k_B T))$ with a prefactor $D_0 = 10^{-3}\ \mathrm{cm^2\,s^{-1}}$ and an activation energy E_a taken as a fraction of the bonding energy between atoms (proportional to $k_B T_f$). One obtains [204]

$$B = 10^{11} \exp(-4.6 T_f/T)\ \mathrm{nm^4/s} \qquad (7)$$

Inserting this value in Eq. (6) leads to Figure 25 where the size of the compact domains is plotted as a function of T/T_f. The important feature is that as long as $T/T_f \leq 1/4$, the incident particles do not merge. Note that this 1/4 is sensitive to the assumed value of D^*, but only via its logarithm. Again, this estimation of R_c/r is an upper limit since coalescence could be slower than predicted by Eq. (5).

What would happen now if the incident clusters were *liquid*? An experimental example of this liquid coalescence is given by the deposition of In_{100} on *a*-C (see above). A rough guess of the coalescence time is given by a hydrodynamics argument [205]: the driving force of the deformation is the surface curvature γ/R^2 where γ is the liquid surface tension and R is the cluster radius. This creates a velocity field which one can estimate using the Navier–Stokes equation: $\eta \Delta v = \gamma/R^2$ where η is the viscosity and v is the velocity of the fluid. This leads to $\tau_c(\mathrm{liquid}) \sim R/v \sim \eta R/\gamma$. Inserting reasonable values for both η (0.01 Pa/s) and γ (1 J/m^{-2}) leads to $\tau_c(\mathrm{liquid}) \sim 0.01R$ which gives $\tau_c(\mathrm{liquid}) = 10$ ps for $R \sim 1$ nm. This is the good order of magnitude of the coalescence times found in simulations of liquid gold clusters ($\tau_c(\mathrm{liquid}) \sim 80$ ps [176]). Now, since $\tau_c(\mathrm{liquid}) \ll t_r$ ($t_r \sim 0.1$ s; see above) cluster–cluster coalescence is almost instantaneous, which would lead to $R_c \sim \infty$. In fact, R_c is limited in this case by *static* coalescence between the big islands formed during the growth. The reason is that the big islands may be solid or pinned by defects leading to a slow coalescence. The analysis is similar here to what has been done for atomic deposition [206].

Thick Films The preceding section has studied the first stages of the growth, the submonolayer regime, which interests researchers trying to build nanostructures on the surface. We attempt here a shorter study of the growth of thick films, which are known to be very different from the bulk material in some cases [4, 7, 13]. The main reason for this is their nanostructuration, as a random stacking of nanometer size crystallites. Therefore, it is interesting to understand how the size of these crystallites is determined and how stable the nanostructured film is. One can anticipate that the physical mechanism for cluster size evolution is, as in the submonolayer case, sintering by atomic diffusion. For thick films, however, surface diffusion can only be effective before a given cluster has been "buried" by the subsequent deposited clusters. Thus, most of the size evolution takes place during growth, for afterward the physical routes to coalescence (bulk or grain boundary diffusion) are expected to be much slower. Studies of compacted nanopowders [4, 208] have shown that nanoparticles are very stable against grain growth. Siegel [4] explains this phenomenon in the following way. The two factors affecting the chemical potential of the atoms, and potentially leading to structure evolutions, are local differences in cluster size or in curvature. However, for the relatively uniform grain size distributions and flat grain boundaries observed for cluster assembled materials [4], these two factors are not active, and there is nothing locally telling the atoms in which direction to migrate to reduce the global energy. Therefore, the whole structure is likely to

be in a deep local (metastable) minimum in energy, as observed in closed-cell foams. The stability of such structures has been confirmed by several computer simulations [209, 210] which have indicated a possible mechanism of grain growth at very high ($T/T_f \sim 0.8$) temperatures: grain boundary amorphization or melting [209].

What determines the size of the supported particles *during* the growth? For thick films, a reasonable assumption is that a cluster impinging on a surface already covered by a layer of clusters does *not* diffuse, because it forms strong bonds with the layer of the deposited clusters. This hypothesis has been checked for the growth of Sb_{2300} on graphite [117] or that of Au_{750} on gold [211]. There are two main differences with submonolayer growth: first, an impinging cluster has more than one neighbor and the sphere–sphere kinetics is not very realistic; second the relevant time for ramification we have used in the preceding section is no longer useful here since clusters do not move. As a first approximation, to obtain an upper limit in the size of the domains, we can use the same coalescence kinetics and take a different "ramification" time: the average time for the arrival of a cluster touching another is roughly $t_f \sim 1/(Fd^2)$ where $d = 2r$ is the diameter of the cluster. If the same formula [Eq. (5)] is used, one finds

$$R_c^4 = r^4 + \frac{B}{Fr^2} \tag{8}$$

The results obtained using the same approximation as in the preceding section for B [Eq. (7)] are shown in Figure 27.

Experimentally, there are observations for deposition of Ni and Co clusters [207]. The size of the crystallites is comparable to the size of the incident (free) clusters. This is compatible with Eq. (8) since the T_f of these elements is very high ($\simeq$ 1800 K). Therefore, Eq. (8) predicts that films grown at $T = 300$ K ($T/T_f \sim 0.17$) should keep a nanostructuration with $R_c \simeq r$, as is observed experimentally [207]. We stress again that a structure obtained with cluster deposition with this characteristic size is not likely to recrystallize in the bulk phase (thereby losing its nanophase properties) unless brought to temperatures close to T_f [4, 209, 210].

7.2.3. Limitations of the Continuum Theory

However, despite its plausibility, Eq. (5) has to be used with care. First, the calculation leading to it from the expression of the flux [Eq. (2)] is only approximate. More importantly, Eq. (2) assumes *isotropic* surface tension and diffusion coefficients. While this approximation may be fruitful for large particles (in the μm range [175]), it is clearly wrong for clusters in the nanometer range. These are generally facetted [176–178] as a result of anisotropic surface energies. This has two important consequences: first, since the particles are not spherical, the atoms do not feel a uniform curvature. For those located on the planar facets, the curvature is even 0, meaning that they will not tend to move away spontaneously. This effect should significantly reduce the atomic flux. Second, the diffusion is hampered by the edges between the facets [179] which induce a kind of "Schwoebel" effect [180]. Then, the effective mass transfer from one end of the cluster to the other may be significantly lower than expected from the isotropic curvatures used in Eq. (2). For these anisotropic surfaces, a more general formula which takes into account the dependence of γ on the crystallographic orientation should be used (see for example [96]). However, this formula is of limited practical interest for two reasons. First, the precise dependence of the surface energy on the crystallographic orientation is difficult to obtain. Second, as a system of two touching facetted clusters does not in general show any symmetry, the solution to the differential equation is hard to find. One possibility currently explored [181] is to assume a simple analytical equation for the anisotropy of 2D islands and integrate numerically the full (anisotropic) Mullins' equations.

Molecular Dynamics Simulations of Coalescence Since continuum theories face difficulties in characterizing the evolution of nanoparticle coalescence, it might be useful to perform MD studies of this problem. Several studies [176, 182, 198] have been performed showing that two distinct and generally subsequent processes lead to coalescence for particles in the nanometer range: plastic deformation [198] and slow surface diffusion [176, 182].

Zhu and Averback [198] have studied the first stages (up to 160 ps) of the coalescence of two single-crystal copper nanoparticles (diameter 4.8 nm). They demonstrate that plastic deformation takes place and that a relative rotation of the particles occurs during this plastic deformation. During the first 5 ps, the deformation is elastic, until the elastic limit (roughly 0.8 nm [198]) is reached: after this, since the shear stress is very high, dislocations are formed and glide on (111) planes in the $\langle 110 \rangle$ direction, as usually seen in fcc systems. After 40 ps the stress on the glide plane is much smaller and dislocation motion is less important: the two particles rotate until a low energy grain boundary is found. This intial stage of the coalescence, where the two particles reorient and find a low energy configuration, is very rapid but does not lead in general to thorough coalescence. An interesting exception might have been found by Yu and Duxbury [182]: their MD simulations showed that for very small clusters (typically less than 200 atoms) coalescence is abrupt provided the temperature is sufficiently close to the melting temperature. They argue that this is due to a (not specified) "nucleation process": plastic deformation is a tempting possibility.

For larger clusters, the subsequent stages are much slower and imply a different mechanism: atom *diffusion* on the surface of the particles. The intial stages of

this diffusion-mediated coalescence have been studied by Lewis et al. [176]. The point was to study if Mullins' (continuum) predictions were useful in this size domain. In the Lewis et al. simulations, the embedded-atom method [171] was used to simulate the behavior of *unsupported* gold clusters for relatively long times (~10 ns). Evidently, an important role of the substrate in the actual coalescence of supported clusters is to ensure thermalization, which is taken care of here by coupling the system to a fictitious "thermostat" [184]. One therefore expects these coalescence events to be relevant to the study of supported clusters that are loosely bound to the substrate (e.g., gold clusters on a graphite substrate). Strong interaction of the clusters with the substrate may be complicated and lead to cluster deformation even for clusters deposited at low energies, for example if the cluster wets the substrate [185, 186].

Figure 26 shows the evolution of the ratio x/R, where x is the radius of the neck between the two particles. After an extremely rapid approach of the two clusters due to the mechanisms studied above (plastic deformation), a slow relaxation to the spherical shape starts (Fig. 27). The time scale for the slow sphericization process is difficult to estimate from Figure 26, but it would appear to be of the order of a few hundred ns or more. This number is substantially larger than one would expect on the basis of phenomenological theories of the coalescence of two soft spheres. Indeed, [174] predicts a coalescence time for two identical spheres, $\tau_c = k_B T R^4/(C D_s \gamma a^4)$, where D_s is again the surface diffusion constant, a is the atomic size, γ is the surface energy, R is the initial cluster radius, and C is a numerical constant ($C = 25$ according to [174]); taking $D_s \sim 5 \times 10^{-10}$ m^2 s^{-1} (the average value found in the simulations; see [176]), $R = 30$ Å, $\gamma \approx 1$ J m^{-2}, and $a = 3$ Å, this yields a coalescence time τ_c of the order of 40 ns. The same theories, in addition, make definite predictions on the evolution of the shape of the system with time. In particular, in the tangent-sphere model, the evolution of the ratio x/R is found [174] to vary as $x/R \sim (t/\tau_c)^{1/6}$ for values of x/R smaller than the limiting value $2^{1/3}$. In Figure 26, the prediction of this simple model (full line) is compared with the results of the present simulations. There is no agreement between model and simulations. The much longer coalescence time observed has been attributed [176] to the presence of facets on the initial clusters, which persist (and rearrange) during coalescence. The facets can be seen in the initial and intermediate configurations of the system in Figure 27; the final configuration of Figure 27 shows that the cluster is more spherical (at least from this viewpoint) and that new facets are forming. That diffusion is slow can in fact be seen from Figure 27: even after 10 ns, at a temperature which is only about 200 degrees below melting for a cluster of this size, only a very few atoms have managed to diffuse a significant distance away from the contact region.

Figure 26. Evolution in time of the ratio of the neck radius, x, to the cluster radius, R. The full line represents the numerical solution obtained by Nichols [174] with an arbitrary time scale, while the crosses are the results of the Lewis et al. [176] simulations.

The precise role of the facets in the coalescence process is a subject of current interest. Experiments have shown that shape evolution is very slow in presence of facets for 3D crystallites (see for example [187]) and recent experiments [188] and computer simulations [189] on 2D islands suggest that the presence of facets can be effective in slowing down the coalescence process. Clearly, more work is needed to get a *quantitative* understanding of nanoparticles coalescence and to evaluate the usefulness of Mullins' approach, especially if one manages to include the crystalline *anisotropy* (see also [190]).

7.2.4. Kinetic Monte Carlo Simulations of Coalescence

To investigate further this point, we have carried out extensive kinetic Monte Carlo simulations of two- and three-dimensional cluster–cluster coalescence. These

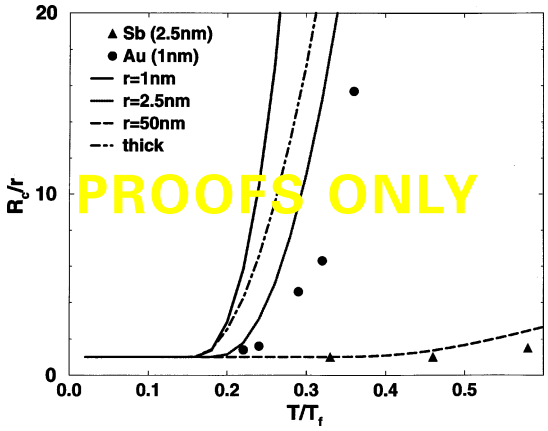

Figure 27. Successive cluster morphologies during the coalescence of a gold 767-atom liquid cluster with another gold 1505-atom solid cluster. The figures represent three stages of the coalescence process after 0, 1, and 10 ns (i.e., times much longer than those studied in [198]).

simulations are not intrinsically limited in the time scales that can be investigated and could therefore help in understanding the role of facets and the limitations of the continuous approach.

We use standard kinetic Monte Carlo simulations to study the equilibration of 2D (3D) crystallites having a triangular (fcc) crystalline structure. Since we are only interested in finding generic laws for the size dependence of $t_{\rm eq}$ (which should not depend on the details of atom–atom interaction), we have chosen a very simple energy landscape for atomic motion [200]. We assume that the potential energy E_p of an atom is proportional to its number i of neighbors, and that the *kinetic barrier* $E_{\rm act}$ for diffusion is also proportional to the number of *initial* neighbors, before the jump, regardless of the *final* number of neighbors, after the jump: $E_{\rm act} = -E_p = i * E$ where E sets the energy scale ($E = 0.1$ eV throughout the chapter). Therefore, the probability p_i per unit of time that an atom with i neighbors moves is $p_i = \nu_0 \exp[-i * E/k_b T]$, where $\nu_0 = 10^{13}\,{\rm s}^{-1}$ is the Debye frequency. Thus, our simple kinetic model includes only *one parameter*, the ratio $E/k_B T$ where k_B is the Boltzmann constant and T is the absolute temperature. The initial configuration of the clusters is elongated, and we stop the relaxation when the crystallites are close to equilibrium, with an aspect ratio of 1.2.

Simulation Results Figure 28a and b shows log–log plots of the relaxation time as a function of the linear dimension of the 2D and 3D islands respectively. The comparison between two and three dimensions reveals, as happens with all comparisons, some similarities and some differences. In both cases, the continuous approach, which predicts a slope of 4, is correct only for the highest temperatures. The physics behind the failure of this macroscopic approach is also similar [200, 201].

At high temperatures, the island perimeter (surface) is rough, full of traps for the diffusing atoms, and the usual

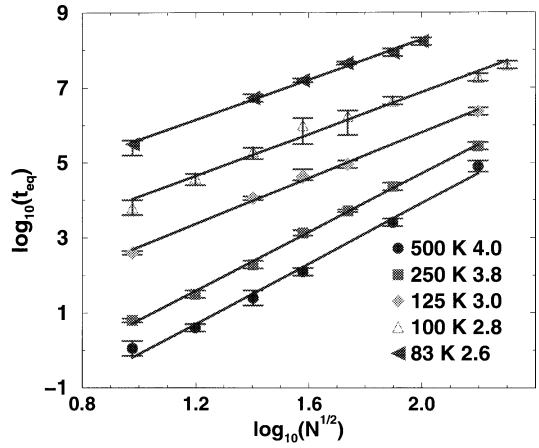

(a)

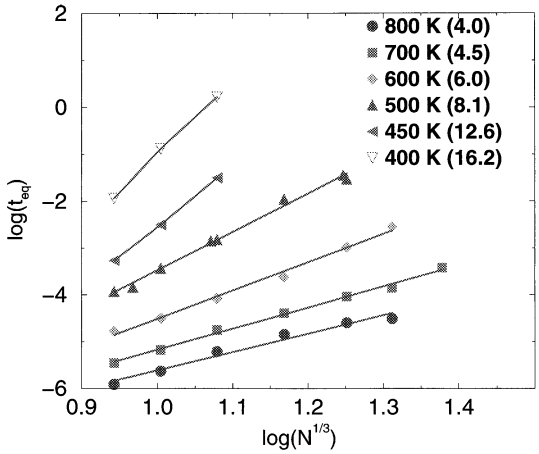

(b)

Figure 28. Evolution of the equilibration time as a function of its characteristic length for (a) two- and (b) three-dimensional islands containing N atoms. The numbers indicate the slope of each linear fit, to be compared to the prediction of the continuous theory (slope = 4).

(individual) atomic surface diffusion is efficient to transfer mass from the high chemical potential regions (the tips of the islands) to the low potential ones (the center of the island). Herring [191] and Nichols and Mullins [174] quantified this physical process long ago: taking the chemical potential as proportional to the local curvature, and using matter conservation and linear response theory, one reaches inevitably the fourth power law, in agreement with our Monte Carlo simulations. This result then validates the use of the concept of curvature at microscopic scales.

At lower temperatures, facets begin to appear, and single atom diffusion can no longer transfer matter from the tips to the center, because these atoms simply wander on top of the facets to become trapped again in the tips. Therefore, a supplementary step has to be overcome for the island to approach equilibrium: the *nucleation* of new atomic lines or terraces. So far, flat and 3D islands behave similarly: now come the differences,

since, after all, when the temperature is lowered, the size-dependence exponent rapidly increases in three dimensions, whereas it slowly decreases in two dimensions (Fig. 28a and b).

In three dimensions, the increase of the size exponent (which is actually due to an exponential behavior) is a consequence of the presence of a nucleation energy barrier which depends on the crystallite size [201]. The nucleation of a germ on a facet is formally similar to the creation of a liquid germ within a gas phase, except that in our case the chemical potential of the atoms in the "gas" depends on the size of the crystallite because these atoms come from the tips, whose curvature (which fixes the chemical potential; see above) is size dependent. Therefore, as the crystallite size increases, an ever larger nucleation barrier has to be overcome, which induces an exponential increase in the relaxation time. In two dimensions, a careful analysis [200] shows that the decrease of the exponent leads to a N dependence of the relaxation time at very low temperatures. Due to the presence of facets, the diffusion is not at all a limiting process, and the limiting step of the relaxation is the nucleation of a germ of the size of the smallest facet on a larger facet [202]. The average time $\tau_{2\,\text{particles}}$ needed to create a two-particle germ on a facet can be shown to be independent on the size of the facet: $\tau_{2\,\text{particles}} \propto \tau_3^2/\tau_2$ (where $\tau_i = 1/p_i$, p_i defined in Section 7.2.4). This step is the most difficult one of the creation of the critical germ: it imposes its activation energy on the limiting step duration. Once a two-particle germ has been created, the germ has a probability $1/(l-2)$ to grow up to the critical size l without disappearing [202]. The duration of the whole limiting step of the relaxation is then about $\tau_{\text{limiting}} \propto \tau_3^2(l-2)/\tau_2 \propto \tau_3^2 l/\tau_2$. It is important to note that τ_{limiting} is the time to transport ***l* particles** from a facet to another. If L is the size of the largest facet, the nucleation of a critical germ has to be repeated about $L-l$ times so that the crystallite goes back to its equilibrium shape. The relaxation time then scales as $\tau_{\text{relaxation}} \propto (L-l)\tau_3^2 l/\tau_2 \propto \tau_3^2 N/\tau_2$.

8. PROPERTIES OF CLUSTER ASSEMBLED FILMS

8.1. Optical Nanostructures from Noble Metal Clusters

Noble metal particles exhibit specific optical properties mainly due to the multipolar collective excitations arising from the dielectric confinement [224]. In the nanometer range the photoabsorption spectra are dominated by an absorption band whose position and width are ruled by the intrinsic properties of the clusters and the surrounding medium (surface plasmon or Mie resonance). These features appear to be size dependent, although no size effect is predicted by the classical Mie theory in the quasistatic limit, except for a mere volume scaling factor. These measured size effects which reflect those of the electronic structure indeed have a quantum origin. In contrast with alkali clusters for which plasmon frequency exhibits a noticeable redshift with decreasing cluster size due to the spill-out phenomenon [225], this trend is reversed in the case of free Ag_N^+ and Au_N^+ clusters [226, 227]; namely a slight blueshift is observed, reflecting the influence of the d-electrons. The understanding of the optical properties of pure metal particles makes the extension of this study to bimetallic clusters in the small size domain very interesting. Bimetallic particles can form either alloys or segregated (referred to as coated, or core-shell, particles) systems [228, 229, 233]. Up to now, most of the experiments on alloyed and coated Ag/Au systems were realized for particles larger than 5 nm in diameter [229, 234]. Here we report on the size evolutions of the optical properties of alumina-embedded mixed silver–gold clusters ($Au_xAg_{(1-x)}$, with x = 0, 0.25, 0.50, 0.75, and 1) with mean optical diameters between 1.5 and 7 nm, prepared by LECBD.

Clusters and alumina matrix are co-deposited on a substrate at room temperature as described in Section 2. The metal volumic fraction is chosen to be less than 5% by controlling both deposition rates, in order to reduce the cluster coalescence effect and to deduce the optical properties of noninteracting isolated particles. Optical absorption spectra displayed in Figure 29 a–e for respectively Au_N,

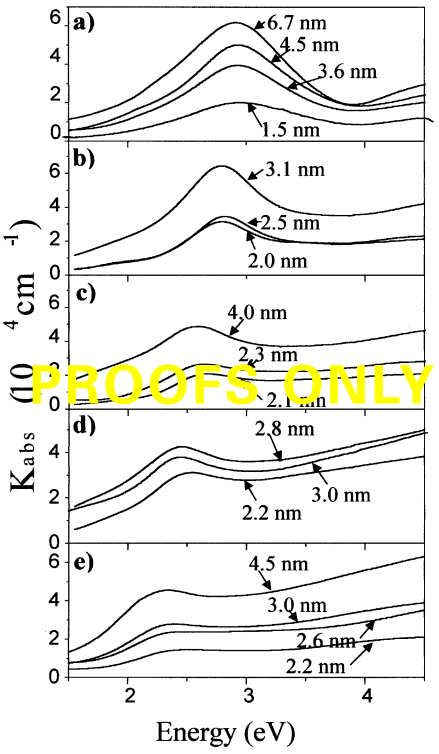

Figure 29. Optical absorption spectra of $Au_xAg_{1-x}N$ clusters in alumina films for various relative compositions x and size distributions (a) AgN; (b) $(Au_{0.25}\ Ag_{0.75})N$; (c) $(Au_{0.5}\ Ag_{0.5})N$; (d) $(Au_{0.75}\ Ag_{0.25})N$; and (e) AuN. The mean optical diameter of clusters (defined as $D_{\text{opt}} = \langle D^3 \rangle^{1/3}$) is indicated for each sample.

$(Au_{0.25}Ag_{0.75})_N$, $(Au_{0.5}Ag_{0.5})_N$, $(Au_{0.75}Ag_{0.25})_N$, and Ag_N-clusters/alumina films, for various cluster-size distributions, exhibit a more or less pronounced absorption band (between 2 and 3 eV) due to the surface plasmon resonance and an increasing absorption in the ultraviolet region due to interband transitions. Comparison of our spectra (for mixed clusters) with those of alloyed and segregated Au–Ag clusters reported in the literature [235–237] highly suggests an alloying of the two metals inside the clusters. One can notice a large broadening and damping of the surface plasmon band as the cluster size decreases, especially for gold-rich clusters [221]. These effects are more pronounced with increasing x, indicating a more important coupling between intra- and interband transitions. Moreover a noticeable blueshift of the resonance with decreasing cluster size is observed for $x = 1$, $x = 0.5$, and $x = 0.75$. This blueshift trend weakens steadily with increasing concentration of silver atoms inside the clusters and is completely quenched for $x = 0.25$ and $x = 0$ [222, 223, 238]. Such quantum size effects can be reproduced in the frame of a quantum/classical theoretical approach where the conduction electrons are quantum-mechanically treated (TDLDA), whereas the optical properties of the matrix and the ionic core background (interband transitions from the d band toward the s–p conduction band, and polarization effects) are classically described through bulklike dielectric functions. The model includes the inner surface skin of ineffective screening by the ionic cores [240], and the local porosity at the particle–matrix interface [222, 223, 238, 239]. The frequency dependence of the real component of $\epsilon_d(\omega)$ [where $\epsilon_d(\omega)$ is the interband contribution in the dielectric function of the metal] is found to be the key feature ruling the competition between the blueshift trend induced by the skin regions of reduced polarizability, and the redshift trend induced by the spill-out phenomenon, the net result of which leads to the quenching of the size effects in silver clusters and the increasing blueshift with gold concentration.

The internal thermalization dynamics of the conduction electrons has been investigated in silver nanoparticles. These measurements based on femtosecond laser spectroscopy [241, 242] lead to the determination of electron–electron thermalization times [243]. The establishment of an electron temperature is taking place on a few hundred femtosecond time scale. An acceleration of the conduction electron thermalization is observed with decreasing silver cluster size. This observed thermalization fastening is ascribed to an increase of electron–electron scattering in small particles. The size dependence of the thermalization time is in good agreement with the model mentioned above and described in detail in [222].

8.2. Magnetic Nanostructures from Transition Metal Clusters and Mixed Transition Metal–Rare Earth Clusters

The preparation of original magnetic nanostructures and the study of their specific properties are playing an increasingly important role directly related with the large number of potential applications in various fields such as information storage and magnetoelectronic devices [213, 215, 244–246]. From the fundamental point of view, the magnetic behavior of individual isolated nanoscale systems was mainly theoretically approached while complementary experimental investigations concerned nanoparticles assemblies because of the sensitivity limitation of the magnetic characterization techniques. More recently, the development of novel original magnetometers based on microSQUID [231, 245] with sensitivity approaching 10^{-17} emu which are capable of detecting a magnetization reversal of one single nanoparticle (i.e., a few cubic nanometers of cobalt) [232] has opened a promising window in this field of "experimental nanomagnetism." For example, in bulk magnetic materials (3D), magnetostatic and bulk magnetocrystalline energies are the main sources of anisotropy whereas in lower dimensionality systems such as thin films (2D), wires (1D), or clusters (0D), strong surface effects are expected, emphasizing the necessity of studying one single nanoobject to provide information on the different contributions to the magnetic anisotropy. Investigations on the sources of magnetic anisotropy in nanoscale systems is of particular importance for future applications with regard to the superparamagnetic limit characteristic of such small systems [246]. In fact, when decreasing the size of the particle down to the nanometric range, the anisotropy energy KuV (where Ku is the anisotropy constant and V is the volume of the particle) which acts to fix the magnetization along an easy axis is counterbalanced by the thermal energy kT responsible for magnetization fluctuations between easy axes. For isolated nanosize particles of conventional magnetic materials, the blocking temperature T_B indicating the upper limit above which the particles behave superparamagnetically is of the order of 10 K to a few tens of K. Consequently, a first challenge prior to applications consists of developing novel magnetic materials in the form of nanosize particles with a rather high anisotropy in order to remain magnetically oriented up to room temperature or above [246]. In the particular case of recording at high area densities, based on the simple extrapolation of the continuous density increase in the last two decades directly connected with bit dimension decrease, one can expect that fundamental physics limitations and especially those related to the superparamagnetic limit will begin to predominate typically around the year 2005. Thus, in this general context of quite fast evolution the effort to understand the physics of ever smaller structures has been paralleled by

attempts to synthesize magnetic nanoparticles with controlled size, morphology, structure, and composition, to reach optimum values of various key parameters: coercivity Hc', remanent magnetization Mr', etc.

For the first time, thin 20 nm Co-cluster/Nb-matrix films were prepared using the co-deposition technique described in Section 2 and subsequently e-beam microlithographed to pattern a large number of microSQUID loops (Fig. 30a). The concentration of Co-clusters is low enough (<0.1) to avoid any interaction between them. Moreover, only the magnetic flux coupling of a cluster located in a microbridge (Fig. 30a) is high enough to allow the detection of its individual magnetization reversal and the measurement of the corresponding spatial switching field distribution. Three-dimensional angular dependence of the switching field was measured by rotating the external magnetic field in and out of the microSQUID plane (Fig. 30b). This last diagram is evidence of one easy magnetization direction along the Hz' axis and one hard magnetization direction along the Hy' axis. Assuming that $T = 0$ K (the experimental temperature being 35 mK) and a uniform rotation process of the particle magnetization, we use the Stoner and Wohlfarth model generalized in three dimensions [247] to perform a rather good fit of this spatial distribution. We deduce a second order anisotropy energy: $E(\mathbf{m})/\mathbf{v} = -\mathbf{K}_1\mathbf{m}_z{}^2 + \mathbf{K}_2\mathbf{m}_y{}^2$, where $\mathbf{v}$ is the magnetic volume of the particle, $\mathbf{m}$ is a unit vector in the magnetization direction, and $K_1 = 2.1 \times 10^5\,\mathrm{J/m^3}$, $K_2 = 0.5 \times 10^5\,\mathrm{J/m^3}$ are the anisotropy constants along the easy and hard axes, respectively. Finally, we can conclude that a Co nanoparticle embedded in a niobium matrix mainly behaves as a macrospin with a biaxial anisotropy corresponding to a second order anisotropy energy. Let us discuss the physical origin of such anisotropy. First we can rule out the usual cubic magnetocrystalline anisotropy for fcc cobalt [219, 230] since this fourth order term is one order of magnitude larger than the experimental one. Second, by considering the nearly spherical shape of the Co clusters, the shape anisotropy term can also be neglected. Moreover, because the elastic constants of the base-centered-cubic (bcc) niobium are smaller than the fcc cobalt ones, the contribution of the magnetoelastic anisotropy energy resulting from the matrix induced isotropic stresses on the particle should be small. Consequently, the experimental anisotropy measured for our individual Co clusters is probably related to an interface anisotropy resulting from the symmetry breaking at the cluster surface. Further theoretical developments and macroscopic experiments on Co/Nb bilayers are in progress to test this last assumption. However, this emphasizes the dominant role of interface in the nanosize range which must be controlled for future applications.

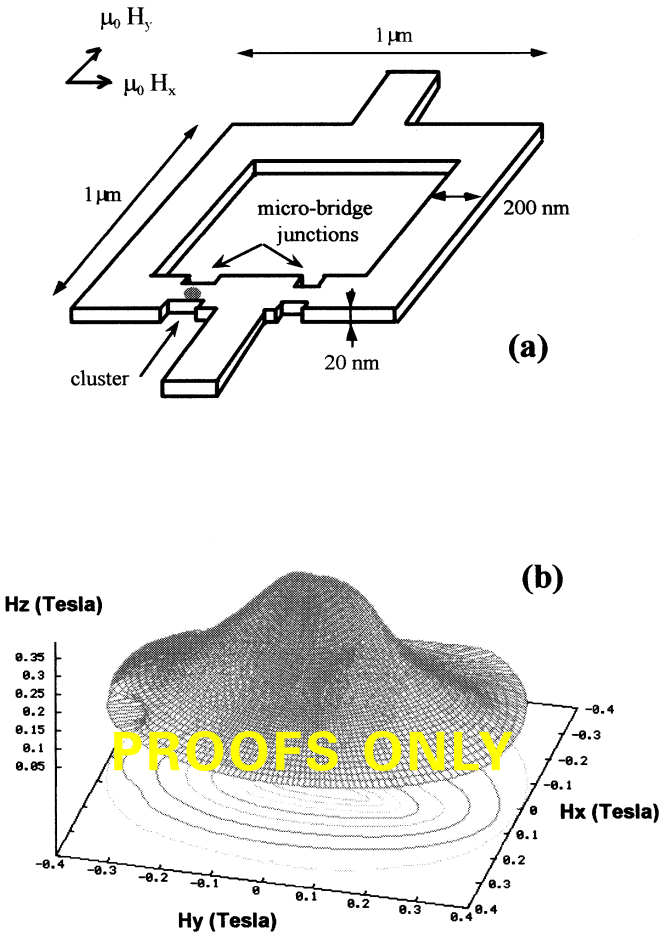

Figure 30. (a) Schematic view of a microSQUID loop patterned out of a 20 nm thick Co clusters/Nb-matrix film by electron beam lithography. The highest detection sensitivity is obtained for nanoclusters located in the microbridges as shown in the figure. (b) 3D distribution of the switching field for an individual Co cluster (diameter $\simeq$ 3 nm, $\simeq$ 1000 Co atoms) embedded in the microbridge.

For a second time, we prepared thick samples consisting of Co-cluster assemblies diluted in a niobium matrix (Co-volumic concentration 5%) in view to perform structural and complementary magnetic characterizations. Structural studies [219, 230] using high resolution transmission electron microscopy, X-ray diffraction, and absorption (performed at the French National Synchrotron Laboratory Facility, LURE, Orsay) indicate that the deposited Co clusters in the bcc Nb matrix can be described as fcc-truncated octahedrons containing about 1000 atoms (diameter 3 nm) distributed as follows: 36% are in the pure Co core of the grain, 27% participate to a Co_4Nb phase in the subsurface layer, and 37% participate to a Co_6Nb7 phase in the surface layer. Moreover, from vibrating sample magnetometry (VSM) measurements on the same Co-clusters/Nb-matrix films, we can conclude that the Co–Nb alloyed interface is a "magnetically dead" layer which is probably at the origin of the reduced "magnetic size" distribution observed with respect to the TEM one [230]. Additional X-ray magnetic circular dichroism (XMCD) experiments were performed at the European Synchrotron Radiation Facilities (ESRF, Grenoble,

France). XMCD is used in our case as a local magnetometry technique operating in the low temperature range (i.e., $T = 8$ K), where the superconducting fluctuations due to the Nb matrix prevent any conventional magnetization measurements. Finally, from the hysteresis loops measured in the temperature range 5–50 K, we deduce the remanent magnetization (Fig. 31) and an effective anisotropy constant $K_{\text{eff}} = 2 \cdot 10^5$ J/m^3 for the Co clusters. Note that K_{eff} is of the same order of magnitude as K_1 previously found from the microSQUID measurements on an individual Co nanpoparticle.

The Co-clusters/Pt-matrix system which is also a miscible couple has been studied in the same conditions [248] to verify the validity of the core-shell model suggested above to account for the magnetic properties in such nanogranular films. Finally, from both Co/Nb and Co/Pt samples we found that cluster magnetization can be written in the form $Ms(T) = xMs'_{\text{core}}(T) + (1-x)Ms'_{\text{shell}}(T)$ [230]. For Co/Pt, one atomic layer is expected to diffuse at the interface, giving $x = 0.63$. In addition, we assume that $Ms'_{\text{core}}(T) = Ms'_{\text{bulk}}(T)$ leading to a magnetization enhancement at the interface, $Ms'_{\text{shell}}(0) = 1900$ kA m^{-1} [to compare with $Ms'_{\text{core}}(0) = 1430$ kA m^{-1}). On the contrary, in the Co/Nb case, Ms_{shell} (0) is found to equal zero and $x = 0.36$, because of the presence of two "magnetically dead" alloyed monolayers at the cluster–matrix interface, leading to the very low experimental value observed $Ms(0) = 515$ kA m^{-1}.

Since the superparamagnetic limit prevents the use of pure transition metal particles with sizes lower than 10 nm to prepare high density storage media [246], intermetallic compounds with strong magnetocrystalline anisotropy such as rare earth–transition metal alloys have been tested. For that purpose, $SmCo_5$ nanoclusters prepared from a bulk $SmCo_5$ targets mounted in the laser vaporization source have been embedded in niobium co-deposited films [220]. Due to the segregation of samarium atoms at the cluster surface, a loss of magnetization is observed in the as-deposited nanostructured samples compared to the bulk phase. However, postannealing treatments in UHV up to 570 °C lead to an improvement of the crystallinity of the Sm–Co nanoparticles and consequently to a significant increase of their magnetic anisotropy at the origin of a blocking temperature T_B of the order of 300 K or larger [249]. This is illustrated in Figure 32 showing the characteristic evolution of the magnetization loops with an increase of Hc as a function of the annealing temperature for a $SmCo_5$-clusters/Nb-matrix film.

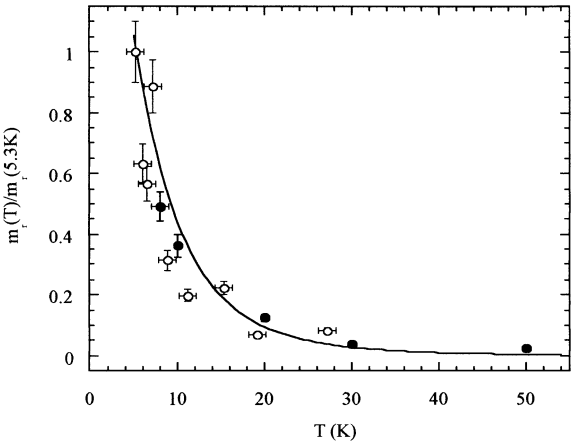

Figure 31. Remanent magnetic moment plotted versus temperature. The signal is first normalized taking $m_r(8\text{ K})_{\text{VSM}} = m_r(8\ K)_{\text{XMCD}}$. One can see that the continuous line curve fits both VSM (full dots) and XMCD (open dots) measurements. From this fit, one can deduce the anisotropy constant $K_{\text{eff}} = 2.0 \pm 0.310^5$ J/m^3.

8.3. Semiconducting Nanostructures from Silicon/Carbon Cagelike Clusters

Both carbon and silicon are tetrahedrally covalent materials but exhibiting different behaviors related to their own electronic structures. In the case of carbon, since the $2p$ orbital is as compact as the $2s$ one, this element presents a wide variety of sp-mixing called hybridization. In pure bulk carbon, the most stable configuration corresponds to four independent bonds (graphite). Another

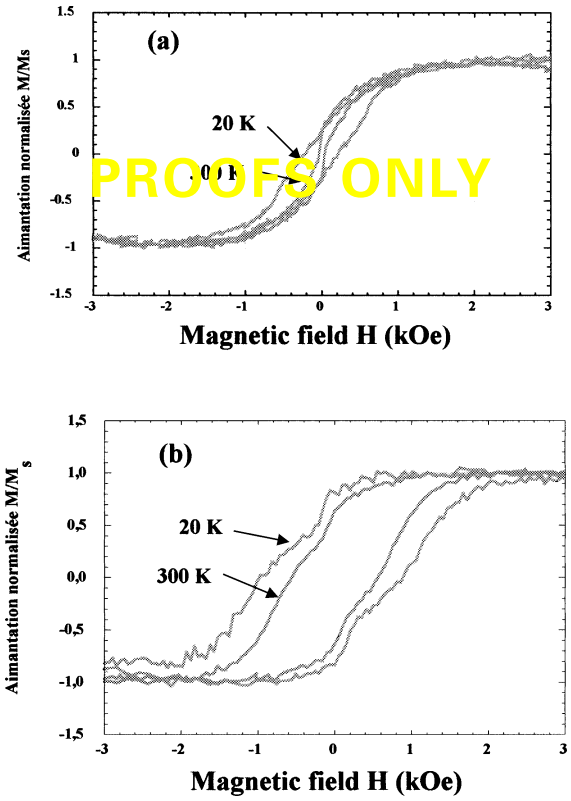

Figure 32. Hysteresis loops obtained by conventional SQUID magnetometry measurements at 20 and 300 K for films of $SmCo_5$ clusters embedded in Nb matrix. The volumic concentrations of $SmCo_5$ clusters were low enough (<5%) to avoid cluster coalescence effects. (a) As-deposited film; (b) film subsequently annealed *in situ* in UHV at 570 °C for 30 minutes.

structure is formed by four orthogonal hybrids leading to the sp^3-hybridization (diamond phase). Silicon presents two main differences with carbon: first, the main stable configuration corresponds to sp^3-hybridization. Second, Si atoms can promote electrons in the $3d$ shell (carbon has no $2d$ shell). Thus, the d-state allows a mean coordination greater than four. This corresponds to the insulator–metallic transition observed in the high pressure phase of silicon. Consequently, the structure of carbon clusters is dominated by a mean hybridization labelled sp^n with $1 < n < 3$, roughly related to the carbon basal plan curvature, while silicon clusters tend to have rather compact structures. Fourfold bondings exist in both carbon and silicon, but carbon clusters promote preferentially two- and threefold bondings corresponding to linear chains and cyclic or cage structures (fullerenes). It is generally admitted that C_N clusters with $N < 10$ atoms consist of linear or planar geometries with low coordination, and above $N = 20$ atoms a possible transition between two- and three-dimensional geometry occurs. Cagelike ion–fullerene structures become the most stable isomers above $N = 32$ atoms, the dodecahedron C_{20} being the first fullerene (Ih symmetry) having the 12 pentagons required by Euler's rules. For silicon, the sp^2-hybridization being highly unfavorable, the fullerenelike structures with an empty core are unstable for large Si_N ($N = 28$ atoms) clusters. For example, Si_{45} looks like a fullerene but with an inner core. However, structures including a large amount of fivefold rings, and especially Si_N with $N = 20, 24, 28$, which are nearly purely sp^3-hybridized, are predicted. It is interesting to mention that these small fullerenes (Si_{20} and Si_{24}) exist in certain polymorph phases called clathrates (i.e., Na_8Si_{46}). These structures consist of a cubic arrangement of Si_{20} dodecahedra with Si_{24} in between. The electronic exchange with alkaline atoms located inside each polyhedron increases the stability of such structure. On the basis of the above-mentioned structures and properties of carbon and silicon neutral free clusters, LECBD experiments of size controlled distributions on various substrates at room temperature have been performed [21]. In the particular case of carbon, distributions centered around C_{20}, C_{60}, and C_{900} were chosen for their strong sp^3, intermediate sp^2–sp^3, and sp^2 characters, respectively. The corresponding films ($\simeq 100$ nm thick) were systematically analyzed using various complementary techniques such as Raman spectroscopy, electron energy loss spectroscopy, and X-ray absorption near edge structure. All these measurements converged to confirm the sp^3, sp^2, and intermediate characters of the C_{20}, C_{900} and C_{60} films, respectively. This is good evidence of a memory effect of the free cluster structures in the films. Moreover, the properties of the films (electrical conductivities, optical absorption spectra, hardnesses) are in agreement with the more or less diamond or graphite characters predicted, emphasizing the capability of the LECBD technique to produce materials with adjustable structures and properties. AFM observations of the deposits and density measurements confirm the highly porous nanostructured morphologies resulting from the nearly random stacking process of incident clusters characteristic of the LECBD technique. Among various carbon films obtained, the most fascinating is the C_{20} film because of its sp^3 character. In fact, metastable structures such as small fullerenes may be produced in the laser vaporization source taking into account the high sursaturation ratio involving a great number of cluster–helium gas collisions. Comparable sets of deposition experiments have been performed with silicon clusters the size distribution of which was centered around Si_{50} since interesting structures are predicted for materials in this size range (Si_{20}, Si_{33}, Si_{45}, ...). As mentioned above, an interesting feature of these structures is the presence of a large number of pentagonal rings on the surface at the origin of a rehybridization of Si, and subsequent changes of the electronic structure with respect to the bulk material. As for carbon, the Si films prepared by LECBD are granular and highly porous. However, the Raman spectra are comparable to that of conventional amorphous silicon (a-Si), despite a strong visible luminescence in red which does not exist in a-Si [13]. We believe that silicon obtained by the LECBD technique constitutes a novel metastable form which could be considered for future optoelectronic applications because of its intense red luminescence.

More recently, we have started studying Si–C clusters. Si–C materials in crystalline and amorphous forms have been extensively studied for 20 years [250]. Such structures are good candidates for large bandgap electronic devices as well as being very hard materials. In all SiC polytypes, the lattice is formed by a periodic arrangement of silicon and carbon atoms in a sp^3 tetrahedrally bonded network with a perfect chemical ordering. Si_xC_{1-x} compounds with $x = 0.5$ are more complex and still debated since compositional disorder introduces homonuclear (i.e., C–C or Si–Si bonds) and heteronuclear bonds (i.e., Si–C bonds). The tendency to chemical ordering into a sp^3 network prevails in Si-rich films. Conversely, the disorder increases in C-rich films. However, most of the samples prepared are more or less described in terms of local tetrahedral environment with additional sp^2 fused rings for rich carbon samples. In this context, original silicon carbide films were prepared by the LECBD technique (from clusters preformed in the gas phase using a combined laser vaporization–inert gas condensation source) [218]. These films exhibited a nanostructured morphology characteristic of the LECBD technique with a large porosity. The minimization of the dangling bonds due to the presence of a large number of atoms at the surface of the nanograins involves a rearrangement of the classical "diamond" tetrahedral structure. This is achieved if silicon and carbon form a compact structure close to the so-called "fullerenes"

structure. In the case of carbon, the fullerenes have an empty core leading to a threefold configuration [251], while silicon cages are "stuffed" with additional silicon atoms inside the cage [216]. This last configuration allows a fourfold structure which is more stable for silicon. For SiC heterofullerenes, competition between threefold and fourfold configurations is expected. In this case, it has been established that empty core fullerenes are stable up to 12 silicon atoms (i.e., Si_xC_{60-x} with $x = 12$ is isostructural to C_{60}).

Figure 33 displays the mass distributions measured in the TOF mass spectrometer of the free ionized clusters $Si_xC^+_{1-x}$ for various values of x. For $x = 0$, pure carbon clusters formed by even numbers of atoms are present (Figure 33a). This is one of the signatures of the fullerene family (i.e., cages with an empty core). Increasing x up to 0.12 reveals additional peaks corresponding to the heterofullerene family as observed in Figure 33b for

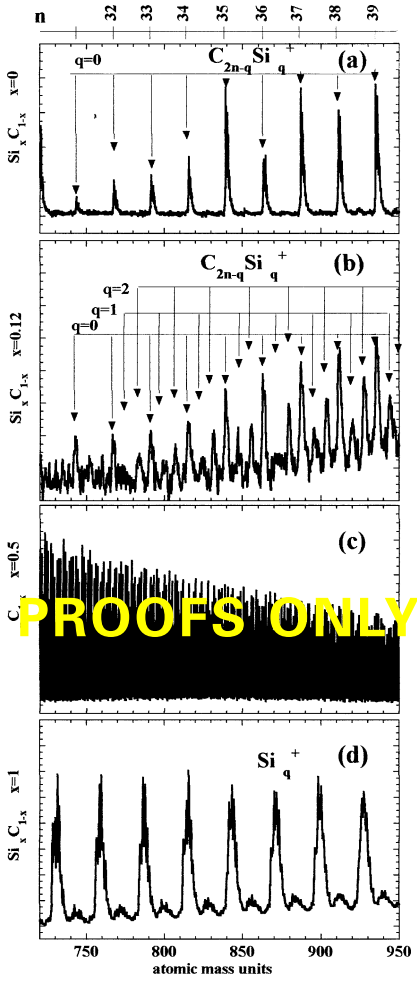

Figure 33. Abundance mass spectra in selected windows of ionized Si_xC_{1-x} clusters for different x values, measured using the high resolution TOF mass spectrometer associated with the laser vaporization cluster source. (a) Pure carbon clusters ($x = 0$, fullerenes); (b) heterofullerenes ($x = 0.12$); (c) mixed SiC clusters ($x = 0.5$); and (d) pure silicon clusters ($x = 1$).

$C_{2n-q}Si_q^+$ clusters with $q = 1$ and $q = 2$ [252]. The mass spectrum for $x = 0.5$ (Figure 33c) corresponds to the stoichiometric compound with all the combinations between carbon and silicon (clusters with odd or even numbers of atoms).

The cluster assembled films resulting from the depositions of various distributions mentioned above have been analyzed by several complementary techniques: plasmon losses, scattering enhanced Raman spectroscopy, X-ray photoelectron spectroscopy (XPS), and Auger-electron spectroscopy (AES). Plasmon loss measurements are summarized in Table 1. These values are strongly dependent on the electron density in the films. For pure silicon cluster films, the plasmon frequency measured (17.2 eV) is close to the value for bulk silicon (17 eV). This is in agreement with the idea of stuffed fullerenes based materials having a density close to the diamond structure one. However, this is not the case for pure carbon cluster films having a structure with an empty core. Moreover, the plasmon frequency for the sample Si_xC_{1-x} with $x = 0.12$ (21 eV) is close to the pure carbon cluster film one (22 eV), since heterofullerenes exhibit a structure comparable to the pure fullerenes structure. For $x = 0.5$, we expect a combination between pure silicon clusters, pure carbon clusters, and SiC clusters with a tetrahedral structure as mentioned below, leading to an intermediate value of the plasmon frequency (19.5 eV).

Figure 34 displays the Raman spectra measured on the Si_xC_{1-x} cluster films. For $x = 0.5$ three types of bonding in the supported clusters were revealed: C–C, Si–Si, and Si–C. The latter corresponds to the chemical ordering part. One has to mention that no noticeable signal is observed during the measurements at low laser fluence ($P < 1$ mW with a spot diameter of about 2–4 μm) for the sample with $x = 0.12$, near the 500–1000 cm^{-1} region corresponding to the phonon density of states in SiC compounds. In this case, the Raman signal appears clearly by increasing the laser power up to

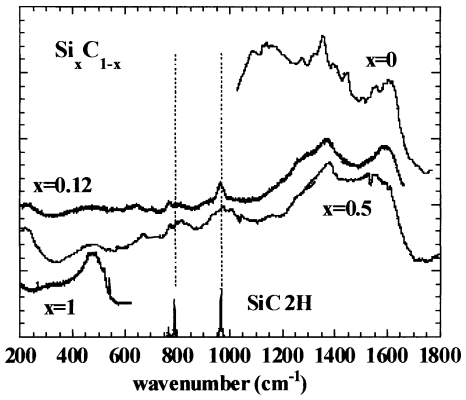

Figure 34. Raman spectra of various Si_xC_{1-x} cluster films for different x values (the same as those in Fig. 8). For comparison, SiC Raman lines in the bulk crystalline phase (SiC 2H-4) are also displayed.

10 mW (Fig. 34). This signal is related to the phototransformation of the sample under laser irradiation (darkening of the irradiated zone). The peaks at high energy are attributed to the "graphitization effect" leading to the formation of amorphous carbon phase with the two characteristic bands labelled G (near 1580 cm^{-1}) and D (disorder) near 1300 cm^{-1} [214]. We also observe bands at 766–815 and 965 cm^{-1} that characterize Si–C vibrational modes. For comparison, the Raman allowed peaks in SiC 2H-4 crystal are given in Figure 34.

The specific electronic structures of the mixed silicon–carbon cluster assembled films are probed by XPS and Auger spectroscopies. Figure 35a shows the Si 2*p* core level line observed in the Si_xC_{1-x} film with $x = 0.12$. For comparison, the lines for bulk silicon (labelled Si-2) and SiC 2H-4 are reported in Figure 35a. The line in $Si_{0.12}C_{0.88}$ is located between the Si-2 and the SiC crystalline phase ones. Figure 10b displays the C 1*s* core level line observed in the $Si_{0.12}C_{0.88}$ film. In this case, the line just coincides with the line of HOPG

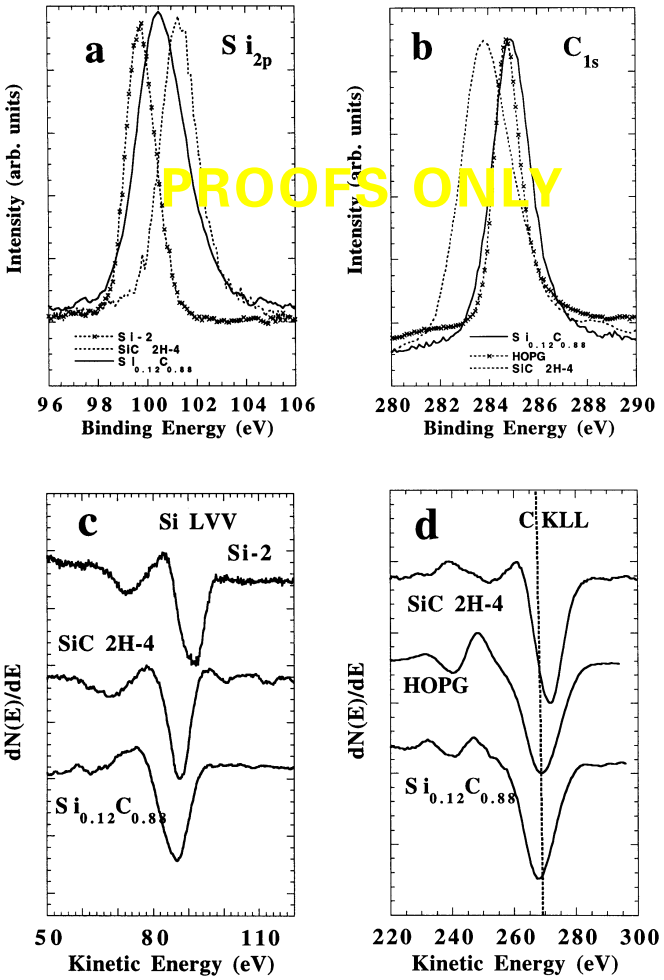

Figure 35. Si 2p core level lines (a) and Si *LVV*-lines (c) measured by XPS and AES, respectively, in Si-2, SiC 2H-4, and $Si_{0.12}C_{0.88}$ samples. C 1*s* core level lines (b) and C *KLL* lines (d) measured in HOPG, SiC 2H-4, and $Si_{0.12}C_{0.88}$ samples.

(threefold hybridization). Figure 35c shows the Si *LVV* lines observed in Si-2, SiC 2H-4, and $Si_{0.12}C_{0.88}$ samples, respectively. It is well known that the Auger shift is enhanced compared to XPS due to the strong extra-atomic relaxation effects in the Auger process. The main band observed in the cluster film at 86.4 eV is slightly shifted with respect to the SiC reference (87.1 eV) and significantly differs from the one in Si-2 (91.3 eV). This result corroborates the expected Si–C bonding in our film. In Figure 35d are reported the carbon *KLL* lines measured in SiC 2H-4, HOPG, and $Si_{0.12}C_{0.88}$, respectively. The *KLL* line in the cluster film presents striking similarities with the HOPG line even for the satellite peaks at low energy. The shoulder labelled s in Figure 35d is partially attributed to the π-component in the electron density of states. In addition, Si *LVV* fine structure is similar to a sp^3-like configuration as expected in heterofullerenes [217].

Although the AES and XPS analyses of the cluster films reveal some striking similarities with SiC 2H-4, we point out some discrepancies that could be the signature of a new SiC phase. The amplitude of the Si 2*p* core level shift (Si-2 being the reference) is larger in SiC 2H-4 than in $Si_{0.12}C_{0.88}$. Conversely, the amplitude of the shift is larger in the cluster film for the *LVV* line. To explain such effects one has to consider that the core level shift has two origins: the chemical bonding and the extra-atomic relaxation due to the electron–core hole interaction during the ejection of the photoelectron. This latter (final) state is described in terms of dielectric medium [253]. Auger lines are more sensitive to the extra-atomic relaxation. A complete analysis reveals that the chemical shift between Si and C is less efficient in $Si_{0.12}C_{0.88}$ than the one observed in SiC 2H-4. Since carbon atoms surround silicon, the carbon ones replace the dielectric constant of the SiC lattice. Even though we have no available information about this term, its value ranges between that of graphite and C_{60}. Consequently, the extra-atomic relaxation will be less efficient in $Si_{0.12}C_{0.88}$ as compared to SiC 2H-4, explaining the larger shift in the $Si_{0.12}C_{0.88}$ *LVV* line (we recall that the Auger process involving two core holes is very sensitive to the relaxation energy). Nevertheless, the lower shift observed in the Si 2*p* core level line reveals a small chemical shift in $Si_{0.12}C_{0.88}$ as compared to SiC 2H-4. This is emphasized since extra-atomic relaxation shift counterbalances the pure chemical shift. This latter result supports the idea of a SiC bonding in $Si_{0.12}C_{0.88}$ films different from those in the bulk SiC phase. In particular, the chemical shift is strongly sensitive to the electron transfer from silicon toward other elements. For example, the presence of dangling bonds in heterofullerenes will be a plausible explanation of the low chemical core level shift in $Si_{0.12}C_{0.88}$ films. Unfortunately, we have no available information about Si–C bonding in the cluster films from Raman spectra due to the low stability of the films under laser irradiation. For

the cluster films with $x = 0.5$, XPS, Auger, and Raman spectroscopies reveal a combination between Si, C, and SiC clusters having a tetrahedral structure. In this case, no heterofullerenes have been pointed out.

9. CONCLUSIONS, PERSPECTIVES

What are the principal ideas presented in this chapter?

First, useful models to analyze the first stages of thin film growth by cluster deposition have been presented in detail (Section 3). These models are useful at a fundamental level, and we have shown in Section 4 how many experimental results concerning *submonolayer* growth can be interpreted by combining these few simple processes (deposition, diffusion, evaporation, ...). Specifically, by comparing the experimental evolution of the island density as a function of the number of deposited particles to the predictions of computer simulations, one can obtain *quantitative* information about the relevant elementary processes.

Second, the quantitative information on diffusion has shown that large clusters can move rapidly on the surface, with diffusion constants comparable to the atomic ones. A first attempt to understand this high diffusivity at the atomic level is given in Section 7: the conclusion is that rapid cluster diffusion might be quite common, provided the cluster and the substrate do not find an epitaxial arrangement. Concerning cluster–cluster coalescence, it has been suggested that this process can be much slower than predicted by the usual sintering theories [174], probably because of the cluster *facets*.

Third, despite all the approximations involved in its derivation, Figure 27 gives important information on the morphology of the film: an *upper* limit for the ratio of the size of the compact domains over the size of the incident clusters. This helps in understanding why cluster deposition leads to nanostructured films provided the deposition temperature is low compared to the fusion temperature of the material deposited ($T_s \leq T_f/4$). Clearly, further experimental and theoretical work is needed in order to confirm (or invalidate) Figure 27.

Finally, we have shown that nanostructured materials obtained from clusters preformed in the gas phase exhibit original structures and properties interesting for the developments of both fundamental studies in the field of nanophysics and various applications in nanooptics, magnetism, electronics, etc. The low energy cluster beam deposition technique especially developed for the preparation of such materials offers some unique potentialities to stabilize new nanostructured phases with properties directly related to those of the incident free clusters. Metallic as well as covalent systems are investigated using this technique. Moreover, pure or mixed clusters are synthesized in all cases for prospects in a wide range of nanostructured materials science. The main aspects attached to the preparation and characterization of cluster assembled materials have been described in this chapter, complemented by some specific examples of cluster based systems with original optical, magnetic, or electronic properties. In the field of optical nanostructures, pure or mixed noble metal clusters (Au, Ag, and Au_xAg_{1-x}) embedded in transparent media have been studied for a better understanding of their optical responses related to plasmon excitations. The studies of magnetic nanostructures from pure transition metal clusters (Co) or mixed transition–rare earth clusters (Co–Sm) have demonstrated capabilities for increasing the magnetic anisotropy and consequently the blocking temperature of nanosystems in view of future applications of high density memory devices and spin electronics. In this case enhanced surface effects combined with magnetocrystalline anisotropy effects are at the origin of a blocking temperature as large as room temperature for nanoparticles with diameters as low as a few nanometers. In the field of semiconducting nanostructures, cagelike silicon and mixed silicon–carbon clusters (fullerenes, stuffed fullerenes, heterofullerenes) are successfully used to produce nanostructured thin fims with electronic structures and properties quite different from those of the corresponding bulk crystalline phases. In the future, electronic bandgap and/or photoluminescence efficiency controls will be the positive results of such studies on covalent semiconducting cluster assembled materials. Finally, further studies to control the nucleation and growth process of the low energy cluster deposits on functionalized substrates to form 2D-organized cluster arrays could be the ultimate step to realizing original quantum devices.

It is clear that we still need to understand many aspects of the physics of cluster deposition. Possible investigation directions include the following, given in an arbitrary order. First, the coalescence of nanoparticles has yet to be understood and quantified. This is a basic question for both submonolayer and thick materials. Second, one has to characterize better the interaction between clusters and the substrate, and especially its influence on the cluster diffusion. It is also important to investigate the possible interactions between the clusters, which could dramatically affect the growth. Obtaining *ordered* arrays of nanoparticles is a hot topic at this moment. A possibility is the pinning of the clusters on ordered surface "defects" which demands a better understanding of cluster interaction with them. Another idea is to use the self-organization of some bacteria to produce an ordered array on which one could arrange the clusters (see [212], especially Chap. 5). Clearly, investigating the interaction of clusters with biological substrates is not an easy task, but it is known that practical results are not always linked to a clear understanding of the underlying mechanisms.

ACKNOWLEDGMENTS

The authors are indebted to G. Guiraud, O. Boisron, and C. Clavier for their technical assistance during the

cluster film preparation using the laser vaporization generator. Thanks to our colleagues from (i) the Laboratoire de Magnetisme Louis Néel, CNRS, Grenoble, France (W. Wernsdorfer, B. Barbara et al.) for fruitful collaborations in the field of magnetic nanostructures; (ii) the Centre de Physique Moléculaire, Optique et Hertzienne, University of Bordeaux, France (F. Vallé, N. Del Fatti, and C. Voisin) for femtosecond spectroscopy measurements on gold and silver cluster films; (iii) the Laboratoire de physicochimie des materiaux luminescents, University of Lyon, France (B. Champagnon et al.) for the active collaborations in the field of Raman and IR spectroscopies of Si and Si–C cluster films; (iv) Jean-Jacques Métois and Claude Henry (CRMC2, Marseille) for interesting discussions. This chapter could never be written without all the theoretical work carried out in collaboration with Pierre Deltour and Muriel Meunier (DPM, Lyon), and my friends Hernán Larralde (Instituto de Física de Cuernavaca, Mexico), Laurent Lewis (Université de Montréal, Canada), and Alberto Pimpinelli (Université Blaise Pascal Clermont-2, France).

REFERENCES

1. H. Gleiter, *Nanostruct. Mater.* 1, 1 (1992).
2. R. E. Palmer, *New. Sci.* 2070, 38 (1997).
3. Special issue on clusters, *Science* 271, 920 (1996).
4. R. W. Siegel, Cluster assembly of nanophase materials, in "Materials Science and Technology" (R. W. Cahn, Ed.), Vol. 15, p. 584. VCH, Weinheim, 1991; see also R. W. Siegel for a more recent contribution to [7].
5. "Cluster Assembled Materials" (Sattler, Ed.), Materials Science Forum Vol. 232. Trans Tech, Zürich, 1996.
6. J. H. Fendler, Ed., "Nanoparticles and Nanostructured Films." Wiley–VCH, Weinheim, 1998.
7. "Nanomaterials: Synthesis, Properties and Applications" (A. S. Edelstein and R. C. Cammarata, Eds.). IOP, Bristol, UK, 1996.
8. S. S. Schweber, *Phys. Today* (November 1993), p. 34.
9. For a short and clear introduction to this enormous field, see for example J. R. Arthur, Thin-film deposition, in "Encyclopedia of Applied Physics" (G. L. Trigg, Ed.), Vol. 21, p. 409. Wiley–VCH, Weinheim, 1997 and references therein. For more complete information, see R. F. Bunshah, "Handbook of Deposition Technologies for Films and Coatings," 2nd ed. Noyes, Park Ridge, NJ, 1994 and D. A. Glocker, "Handbook of Thin Film Process Technology." IOP, Philadelphia, 1995.
10. C. C. Koch, Mechanical milling and alloying, in "Materials Science and Technology" (R. W. Cahn, Ed.), Vol. 15, p. 584. VCH, Weinheim, 1991.
11. "Nanostructured Materials: Clusters, Composites and Thin Films," ACS Symposium Series 679 (V. M. Shalaev and M. Moskovits, Eds.). Am. Chem. Soci., Washington DC, 1997.
12. C. G. Granqvist and R. A. Buhrman, *J. Appl. Phys.* 47, 2200 (1976).
13. P. Melinon et al., *Internat. J. Modern Phys. B* 9, 339 (1995); A. Perez et al., *J. Phys. D* 30, 709 (1997).
14. P. Jensen, *Rev. Modern Phys.* 71, 1695 (1999).
15. W. de Heer, *Rev. Modern Phys.* 65, 611 (1993).
16. P. Joyes, "Les agrégats inorganiques élémentaires." Ed. de Physique, Paris, 1990.
17. "Microclusters," Springer Series in Materials Science 4 (S. Sugano, Y. Nishina, and S. Ohnishi, Eds.) Springer-Verlag, Berlin, 1987.
18. Averback, Ed., "Cluster and Cluster-Assembled Materials," MRS Proceedings, Vol. 206, 1991; *Mater. Sci. Eng. A* 217/218 (1996); Proceedings of ISSPIC 7, *Surf. Rev. Lett.* 3 (1996); *Z. Phys. D* 40, (1997).
19. G. Fuchs, P. Mélinon, F. Dos Santos Aires, M. Treilleux, B. Cabaud, and A. Hoareau, *Phys. Rev. B* 44, 3926 (1991).
20. C. Bréchignac, Ph. Cahuzac, F. Carlier, M. de Frutos, A. Masson, C. Colliex, C. Mory, and B. Yoon, *Z. Phys. D* 40, 515 (1997); B. Yoon, Ph.D. Thesis, University of Orsay, France, 1997; C. Bréchignac, Ph. Cahuzac, F. Carlier, C. Colliex, C. Mory, M. de Frutos, A. Masson, and B. Yoon, *Phys. Rev. B* 57, R2084 (1998).
21. V. Paillard, P. Melinon, J. P. Perez, V. Dupuis, A. Perez, and B. Champagnon, *Phys. Rev. Lett.* 71, 4170 (1993).
22. V. P. Zhdanov and P. R. Norton, *Appl. Surf. Sci.* 81, 109 (1994); M. C. Bartelt, L. S. Perkins, and J. W. Evans, *Surf. Sci. Lett.* 344, L1193 (1995); C. Ratsch, P. Smilauer, A. Zangwill, and D. D. Vvedensky, *Surf. Sci. Lett.* 329, L599 (1995).
23. *Nanostructured Materials* (Pergamon Press); *Physica E* (Elsevier Science).
24. http://www.msel.nist.gov/structure/metallurgy/techactv95/nanostruc.html; http://nanoweb.mit.edu/http://www.eas.asu.edu/nano/nano2.html.
25. *Europhys. News* 28, 89 (1997).
26. Special edition of *Phys. Today*, February 1990.
27. Special edition of *Phys. Today*, June 1993;
28. M. A. Herman and H. Sitter, "Molecular Beam Epitaxy." Springer-Verlag, Berlin, 1989; A. Y. Cho, "Molecular Beam Epitaxy." Am. Inst. of Phys., Woodbury, NY, 1994.
29. M. Lagally, *Phys. Today* 46, 24 (1993) and references therein.
30. "Nanophase Materials: Synthesis—Properties—Applications," NATO Advanced Study Series, Series E, Vol. 260 (C. Hadjiapanayis and R. W. Siegel, Eds.). Nijhoff, Dordrecht, 1994.
31. P. Jena et al., in "Cluster Assembled Materials" (Sattler, Ed.), Materials Science Forum Vol. 232, p. 1. Trans Tech, Zürich, 1996. See also P. Jena and S. N. Khanna, *Mater. Sci. Eng. A* 217/218, 218 (1996).
32. R. Turton, "The Quantum Dot." Freeman, New York, 1995.
33. A. P. Alivisiatos, *Science*, 271, 933 (1996); L. Banyai and S. W. Koch, "Semiconductor Quantum Dots." World Scientific, Singapore, 1993; *Mater. Res. Soc. Bull.* 23 (1998); C. Weisbuch and B. Binter, "Quantum Semiconductor Structures." Academic Press, New York, 1991.
34. H. J. Freund, *Angew. Chem. Int. Ed.* 36, 452 (1997); P. L. J. Gunter, J. W. H. Niemantsverdriet, T. H. Ribeiro, and G. A. Somorjai, *Catal. Rev. Sci. Engine* 39, 77 (1997); C. R. Henry, C. Chapon, S. Giorgio, and C. Goyhenex, in "Chemistry and Reactivity of Clusters and Thin Films" (R. M. Lambert and G. Pacchioni, Eds.), NATO ASI Series E, Vol. 331, p. 117. Kluwer, Dordrecht, 1997.
35. C. R. Henry, *Surf. Sci. Rep.* 31, 231 (1998).
36. M. Che and C. O. Benett, *Adv. Catal.* 36, 55 (1989).
37. G. Pacchioni and N. Roesch, *Surf. Sci.* 306, 169 (1994).
38. P. W. Jacobs, S. J. Wind, F. H. Ribeiro, and G. A. Somorjai, *Surf. Sci.* 372 L249 (1997).
39. D. M. Schaefer, A. Patil, R. P. Andres, and R. Reifenberger, *Phys. Rev. B* 51, 5322 (1995).
40. H. Brune, *Surf. Sci. Rep.* 31 121 (1998).
41. G. Springholz, V. Holy, M. Pinczoltis, and G. Bauer, *Science*, 282, 734 (1998).
42. D. J. Eaglesham and M. Cerullo, *Phys. Rev. Lett.* 64, 1943 (1990).
43. For a review, see H. Ibach, *Surf. Sci. Rep.* 29, 193 (1997) and *Mater. Res. Soc. Bull.* 21, (1996); D. Leonard et al., *Appl. Phys. Lett.* 63, 23 (1993); J. M. Moison et al., *Appl. Phys. Lett.* 64, 196 (1994); H. Brune and K. Kern, Heteroepitaxial metal growth: The effects of strain, in "Growth and Properties of Ultrathin Epitaxial Layers" (D. A. King and D. P. Woodruff, Eds.), The Chemical Physics of Solid Surfaces, Vol. 8, p. 149. Elsevier, Amsterdam, 1997; H. Brune et al., *Phys. Rev. B* 52, R14380 (1995).
44. J. L. Vialle et al., *Rev. Sci. Instrum.* 68, 2312 (1997).

45. J. L. Rousset et al., *J. Chem. Phys.* 102, 8574 (1995); J. L. Rousset et al., *Surf. Sci.* 352–354, 583 (1996).
46. C. Ray et al., *Phys. Rev. Lett.* 80, 5365 (1998).
47. T. Michely, M. Hohage, M. Bott, and G. Comsa, *Phys. Rev. Lett.* 70, 3943 (1993).
48. M. Kalff, G. Comsa, and T. Michely, *Phys. Rev. Lett.* 81, 1255 (1998).
49. R. P. Andres et al., *Science* 273, 1690 (1996).
50. J. Schiotz, T. Rasmussen, K. W. Jacobsen, and O. H. Nielsen, *Philos. Mag. Lett.* 74, 339 (1996).
51. E. M. Chudnowski, *J. Appl. Phys.* 64, 5570 (1988).
52. V. Dupuis et al., *J. Appl. Phys.* 76 6676 (1994).
53. I. Yamada and G. H. Takakoa, *Japan J. Appl. Phys.* 32, 2121 (1993) and references therein; I. Yamada, *Mater. Sci. Eng. A* 217/218, 82 (1996).
54. I. Yamada, H. Inokawa, and T. Takagi, *Japan. J. Appl. Phys.* 56, 2746 (1984).
55. R. Biswas, G. S. Grest, and C. M. Soukoulis, *Phys. Rev. B* 38, 8154 (1988).
56. Z. Insepov and I. Yamada, *Nucl. Instrum. Methods. B* 99, 248 (1995).
57. D. Turner and H. Shanks, *J. Appl. Phys.* 70, 5385 (1991).
58. R. L. McEachern, W. L. Brown, M. F. Jarrold, M. Sosnowski, G. Takaoka, H. Usui, and I. Yamada, *J. Vac. Sci. Technol. A* 9, 3105 (1991).
59. H. Haberland, M. Karrais, M. Mall, and Y. Thurner, *J. Vac. Sci. Technol. A* 10, 3266 (1992).
60. H. Haberland, Z. Insepov, and M. Moseler, *Phys. Rev. B* 51, 11061 (1995).
61. C. Massobrio and B. Nacer, *Z. Phys. D* 40, 526 (1997) and references therein.
62. S. J. Carroll, S. G. Hall, R. E. Palmer, and R. Smith, *Phys. Rev. Lett.* 81, 3715 (1998).
63. I. M. Goldby, L. Kuipers, B. von Issendorff, and R. E. Palmer, *Appl. Phys. Lett.* 69, 2819 (1996).
64. G. M. Francis, I. M. Goldby, L. Kuipers, B. von Issendorff, and R. E. Palmer, *J. Chem. Soc. Dalton Trans.* 1, 665 (1996).
65. G. H. Wang, H. Q. Zhang, M. Han, J. X. Ma, and Q. Wang, *Phys. Lett. A* 189, 218 (1994).
66. J. X. Ma, M. Han, H. Q. Zhang, Y. C. Gong, and G. H. Wang, *Appl. Phys. Lett.* 65, 1513 (1994).
67. E. Ganz, K. Sattler, and J. Clarke, *Surf. Sci.* 219, 33 (1989); O. F. Hagena, *Rev. Sci. Instrum.* 63, 2374 (1992); O. F. Hagena, G. Knop, R. Fromknecht, and G. Linker, *J. Vac. Sci. Technol. A* 12, 282 (1994); A. Wawro, R. Czajka, A. Kasuya, and Y. Nishina, *Surf. Sci.* 365, 503 (1996).
68. J. F. Roux et al., *Appl. Phys. Lett.* 64, 1212 (1994).
69. C. L. Kelchner and A. E. De Pristo, *Nanostruct. Mater.* 8, 253 (1997).
70. A. Canning, G. Galli, and J. Kim, *Phys. Rev. Lett.* 78, 4442 (1997).
71. J. F. Roux, L. Bardotti, B. Cabaud, M. Treilleux, P. Jensen, and A. Hoareau, *Mater. Sci. Eng. B* 49, 110 (1997). See also E. Kay, *Z. Phys. D* 3, 251 (1986).
72. K. Sattler, J. Muhlbach, and E. Recknagel, *Phys. Rev. Lett.* 45, 821 (1980).
73. D. Rayane, P. Melinon, B. Tribollet, B. Cabaud, A. Hoareau, and M. Broyer, *J. Chem. Phys.* 91, 3100 (1989).
74. M. Samy El-Shall and A. S. Edelstein, Chap. 2 of Ref. [7].
75. P. Milani and W. A. de Heer, *Rev. Sci. Instrum.* 61 147 (1990).
76. G. Vandoni, C. Felix, R. Monot, J. Buttet, and W. Harbich, *Chem. Phys. Lett.* 229, 51 (1994).
77. H.-P. Cheng and U. Landman, *Science* 260, 1304 (1993).
78. I. M. Vitomirov, C. M. Aldao, G. D. Waddill, C. Capasso, and J. H. Weaver, *Phys. Rev. B* 41, 8465 (1990).
79. W. D. Luedtke and U. Landman, *J. Vac. Sci. Technol. B* 9, 414 (1991).
80. J. J. Pascual, J. Méndez, J. Gómez-Herrero, A. M. Baró, N. García, and V. T. Binh, *Phys. Rev. Lett.* 71, 1852 (1993).
81. Z. Zhang and M. G. Lagally, *Science* 276, 377 (1997).
82. P. Jensen, *La Recherche* 283, 42 (1996).
83. P. Meakin, *Phys. Rev. Lett.* 51, 1119 (1983); M. Kolb, R. Botet, and R. Jullien, *Phys. Rev. Lett.* 51, 1123 (1983); for a comprehensive review, see H. J. Herrmann, *Phys. Rep.* 136, 153 (1986).
84. A. F. Voter, *Phys. Rev. B* 34, 6819 (1986).
85. M. Schroeder, P. Smilauer, and D. E. Wolf, *Phys. Rev. B* 55, 10814 (1997).
86. T. Shitara et al., *Phys. Rev. B* 46, 6815 (1992); 46, 6825 (1992).
87. T. R. Linderoth et al., *Phys. Rev. Lett.* 77, 87 (1996).
88. J. W. Evans and M.C. Bartelt, *J. Vac. Sci. Technol. A* 12, 1800 (1994).
89. C. Mottet, R. Ferrando, F. Hontinfinde, and A. C. Levi, *Surf. Sci.* (1998).
90. G. Zinsmeister, *Vacuum* 16, 529 (1966); *Thin Solid Films* 2, 497 (1968); *Thin Solid Films* 4, 363 (1969); *Thin Solid Films* 7, 51 (1971).
91. M. Smoluchovsky, *Phys. Z.* 17, 557 (1916).
92. J. A. Venables, *Philos. Mag.* 27, 697 (1973).
93. J. A. Venables, G. D. T. Spiller, and M. Hanbücken, *Rep. Progr. Phys.* 47, 399 (1984).
94. S. Stoyanov and D. Kaschiev, "Current Topics in Materials Science." (E. Kaldis, Ed.). North-Holland, Amsterdam, 1981.
95. J. Villain, A. Pimpinelli, L.-H. Tang, and D. E. Wolf, *J. Phys. I France* 2, 2107 (1992); J. Villain, A. Pimpinelli, and D. E. Wolf, *Comments Cond. Mater. Phys.* 16, 1 (1992).
96. J. Villain and A. Pimpinelli, "Physique de la Croissance Cristalline." Eyrolles, 1995; English edition to be published by Cambridge Univ. Press, Cambridge, UK, 1998.
97. A. Pimpinelli, P. Peyla, P. Jensen, and H. Larralde, in "Directions in Condensed Matter Physics" (Z. Zhang and M. Lagally, Eds.). World Scientific, Singapore, 1997.
98. G. S. Bales and D. C. Chrzan, *Phys. Rev. B* 50, 6057 (1994).
99. N. Metropolis et al., *J. Chem. Phys.* 21, 1087 (1953).
100. K. Binder, Ed., "Monte Carlo Methods in Statistical Physics." Springer-Verlag, Berlin, 1986.
101. K. Binder, Mechanics: Classical to Monte Carlo methods, in "Encyclopedia of Applied Physics" (G. L. Trigg, Ed.), Vol. 10. Wiley, London, 1994; K. Binder, *Rep. Progr. Phys.* 60, 487 (1997).
102. L.-H. Tang, *J. Phys. I France* 3, 935 (1993).
103. J. W. Evans and M. C. Bartelt, in "Directions in Condensed Matter Physics" (Z. Zhang and M. Lagally, Eds.). World Scientific, Singapore, 1997. For a review, see [96, 105].
104. P. Jensen, A.-L. Barabási, H. Larralde, S. Havlin, and H. E. Stanley, *Nature* 368, 22 (1994); *Phys. A* 207, 219 (1994); *Phys. Rev. B* 50, 15316 (1994).
105. A.-L. Barabasi and H. E. Stanley, "Fractal Concepts in Surface Growth." Cambridge Univ. Press, Cambridge, UK, 1995.
106. K. Binder, p. 1 of [100].
107. A. Bogicevic, S. Liu, J. Jacobsen, B. Lundqvist, and H. Metiu, *Phys. Rev. B* 57, R9459 (1998).
108. H. C. Kang and W. H. Weinberg, *J. Chem. Phys.* 90, 2824 (1989).
109. S. V. Khare et al., *Phys. Rev. Lett.* 75, 2148 (1995).
110. S. V. Khare and T. L. Einstein, *Phys. Rev. B* 54, 11752 (1996).
111. A. B. Bortz, M. H. Kalos, and J. L. Lebowitz, *J. Comp. Phys.* 17, 10 (1975).
112. C. Ratsch, A. Zangwill, and P. Smilauer, *Surf. Sci.* 314, L937 (1994).
113. B. Z. Nosho, V. Bressler-Hill, S. Varma, and W. H. Weinberg, *Surf. Sci.* 364, 164 (1996); M. Schroeder and D. E. Wolf, *Surf. Sci.* 375, 129 (1997).
114. J. C. Hamilton, *Phys. Rev. B* 55, R7402 (1997).
115. J. Frenkel and T. Kontorova, *Phys. Z. Sowj.* 13, 1 (1938).
116. P. Jensen, *Comments At. Mol. Phys.* (1998).

117. L. Bardotti, P. Jensen, M. Treilleux, A. Hoareau, and B. Cabaud, *Phys. Rev. Lett.* 74, 4694 (1995); *Surf. Sci.* 367, 276 (1996).
118. P. Jensen and B. Niemeyer, *Surf. Sci. Lett.* 384, 823 (1997).
119. P. Jensen, H. Larralde, and A. Pimpinelli, *Phys. Rev. B* 55, 2556 (1997): note that in this paper, a mistake was made in the normalization of the island size distributions (Fig. 9).
120. P. Jensen, L. Bardotti, A.-L. Barabási, H. Larralde, S. Havlin, and H. E. Stanley, "Disordered Materials and Interfaces [Proc. Symposium of Materials Research Society, 1995]" (H. Z. Cummins, D. J. Durian, D. L. Johnson, and H. E. Stanley, Eds.), p. 391. Materials Research Society, Pittsburgh, 1996.
121. C. Ratsch, P. Smilauer, A. Zangwill, and D. D. Vvedensky, *Surf. Sci. Lett.* 329, L599 (1995).
122. P. Jensen, A.-L. Barabási, H. Larralde, S. Havlin, and H. E. Stanley, *Fractals* 4, 321 (1996).
123. J. A. Stroscio and D. T. Pierce, *J. Vac. Sci. Technol. B* 12 1783 (1994).
124. J. Evans and M. C. Bartelt, *Phys. Rev. B* 54, R17359 (1996).
125. D. Stauffer and A. Aharony, "Introduction to Percolation Theory," 2nd ed. Taylor & Francis, London, 1992.
126. P. Melinon, P. Jensen, J. Hu, A. Hoareau, B. Cabaud, and D. Guillot, *Phys. Rev. B* 44, 12562 (1991).
127. B. Lewis and J. C. Anderson, in "Nucleation and Growth of Thin Films." Academic Press, New York, 1978; J. L. Robins and T. N. Rhodin, *Surf. Sci.* 2, 346 (1964); H. Larralde, P. Jensen, M. Meunier, and A. Pimpinelli, in "Proceedings of the Materials Research Society, Fall Meeting," Boston, December 1996.
128. S. Liu, L. Bönig, and H. Metiu, *Phys. Rev. B* 52 2907 (1995).
129. L. Kuipers and R. E. Palmer, *Phys. Rev. B* 53, R7646 (1996).
130. I. Furman and O. Biham, *Phys. Rev. B* 55, 7917 (1997)
131. M. Meunier, Ph.D. Thesis, Université Aix-Marseille, 1995; M. Meunier and C. R. Henry, *Surf. Sci.* 307, 514 (1994).
132. M. Harsdorff, *Thin Solid Films* 116, 55 (1984).
133. J. C. Zanghi, J. J. Métois, and R. Kern, *Philos. Mag.* 31, 743 (1975).
134. X. Xiao, Y. Xie, C. Jakobsen, and Y. R. Shen, *Phys. Rev. B* 56, 12529 (1997) and references therein; K. Haug, Z. Zhang, D. John, C. F. Walters, D. M. Zehner, and W. E. Plummer, *Phys. Rev. B* 55, R10233 (1997); S. Liu, L. Bönig, J. Detch, and H. Metiu, *Phys. Rev. Lett.* 74, 4495 (1995) and references therein.
135. C. R. Henry, C. Chapon, and B. Mutaftschiev, *Thin Solid Films* 33, 1 (1976).
136. P. Jensen, M. Meunier, H. Larralde, and A. Pimpinelli, *Surf. Sci.* 412–13, 458 (1998).
137. H. Brune, H. Röder, C. Boragno, and K. Kern, *Phys. Rev. Lett.* 73, 1955 (1994).
138. S.-L. Chang and P. A. Thiel, *Critical Revi. Surf. Chemi.* 3, 239 (1994).
139. F. Dos Santos Aires, Ph.D. Thesis, University of Lyon, 1990.
140. N. Combe and P. Jensen, *Phys. Rev. B* 57, 15553 (1998).
141. L. Lewis, P. Jensen, N. Combe, and J. L. Barrat, *Phys. Rev. B* 61, 16084 (2000).
142. L. Bardotti et al., in preparation.
143. M. Treilleux et al., unpublished.
144. A. Masson, J. J. Métois, and R. Kern, *Surf. Sci.* 27, 463 (1971).
145. R. Gomer, *Rep. Progr. Phys.* 53, 917 (1990).
146. J. J. Métois, K. Heinemann, and H. Poppa, *Philos. Mag.* 35, 1413 (1977).
147. R. Kern, G. Le Laye, and J. J. Métois, "Current Topics in Materials Science," Vol. 3, Chap. 3, North-Holland, Amsterdam, 1979.
148. J. W. Matthews and E. Grünbaum, *J. Vac. Sci. Technol.* 3, 133 (1966).
149. L. Y. Kuo and P. Shen, *Surf. Sci. Lett.* 373, L350 (1997).
150. G. L. Kellogg, *Phys. Rev. Lett.* 73, 1833 (1994).
151. G. L. Kellogg, *Surf. Sci. Rep.* 21, 1 (1994).
152. S. Liu, Z. Zhang, J. Norskov, and H. Metiu, *Surf. Sci.* 321, 161 (1994).
153. H. Shao, P. C. Weakliem, and H. Metiu, *Phys. Rev. B* 53, 16041 (1996).
154. W. W. Pai, A. K. Swan, Z. Zhang, and J. F. Wendelken, *Phys. Rev. Lett.* 79, 3210 (1997).
155. D. S. Sholl and R. T. Skodje, *Phys. Rev. Lett.* 75, 3158 (1995).
156. M. Zinke-Allmang, L. C. Feldman, and M. H. Grabow, *Surf. Sci. Rep.* 16, 377 (1992).
157. J. M. Soler, *Phys. Rev. B* 53, R10540 (1996); C. deW. Van Siclen, *Phys. Rev. Lett.* 75, 1574 (1995).
158. J. M. Wen, S. L. Chang, J. W. Burnett, J. W. Evans, and P. A. Thiel, *Phys. Rev. Lett.* 73, 2591 (1994); J. M. Wen, S. L. Chang, J. W. Burnett, J. W. Evans, and P. A. Thiel, *Phys. Rev. Lett.* 76, 562 (1996).
159. Z. P. Shi, A. K. Swan, Z. Zhang, and J. F. Wendelken, *Phys. Rev. Lett.* 76, 4927 (1996).
160. J. C. Hamilton, M. S. Daw, and S. M. Foiles, *Phys. Rev. Lett.* 74, 2760 (1995).
161. S. C. Wang and G. Ehrlich, *Phys. Rev. Lett.* 79, 4234 (1997).
162. J. C. Hamilton, *Phys. Rev. Lett.* 77, 885 (1996); J. C. Hamilton, *Phys. Rev. B* 55, R7402 (1997).
163. H. Reiss, *J. Appl. Phys.* 39, 5045 (1968).
164. A. Masson, J. J. Metois, and R. Kern, *Surf. Sci.* 27, 483 (1971).
165. P. Deltour, P. Jensen, and J.-L. Barrat, *Phys. Rev. Lett.* 78, 4597 (1997).
166. J. E. Lennard-Jones, *Proc. Roy. Soc. London Ser.* A 106, 463 (1924).
167. *Mater. Res. Soc. Bull.* 21 (1996).
168. M. P. Allen and T. E. Tidesley, "Computer Simulation of Liquids." Oxford Univ. Press, London, 1987.
169. J. Hautman et al., *Phys. Rev. Lett.* 67, 1763 (1991).
170. U. Landmann (unpublished): oral presentation at ISSPIC9, Lausanne, Switzerland, 1998.
171. S. M. Foiles, M. I. Baskes, and M. S. Daw, *Phys. Rev. B* 33, 7983 (1986).
172. E. Ruckenstein and B. Pulvermacher, *J. Catal.* 29 224 (1973); D. B. Dadybujor, S. P. Marsh, and M. E. Glicksman, *J. Catal.* 99, 358 (1986); S. A. Stevenson, J. A. Dumesic, R. T. K. Baker, and E. Ruckenstein, "Metal–Support Interactions in Catalysis, Sitering and Redispersion." Van Nostrand Reinhold, New York, 1987.
173. W. W. Mullins, *J. Appl. Phys.* 28, 333 (1957).
174. F. A. Nichols and W. W. Mullins, *J. Appl. Phys.* 36, 1826 (1965); F. A. Nichols, *J. Appl. Phys.* 37, 2805 (1966).
175. J. C. Heyraud, J. J. Métois, and J. M. Bermond, *J. Cryst. Growth* 98, 355 (1989).
176. L. Lewis, P. Jensen, and J.-L. Barrat, *Phys. Rev. B* 56, 2248 (1997).
177. M. Flüelli, P. A. Buffat, and J. P. Borel, *Surf. Sci.* 202, 343 (1988).
178. Ph. Buffat and J.-P. Borel, *Phys. Rev. A* 13, 2287 (1976).
179. S. Valkealahti and M. Manninen, *Phys. Rev. B* 57, 15533 (1998).
180. R. L. Schwoebel, *J. Appl. Phys.* 40, 614 (1969); R. L. Schwoebel and E. J. Shipsey, *J. Appl. Phys.* 37, 3682 (1966); J. Villain, *J. Phys. I* 1, 19 (1991).
181. N. Combe, P. Jensen, A. Pimpinelli, and C. Misbah, unpublished.
182. X. Yu and P. M. Duxbury, *Phys. Rev. B* 52, 2102 (1995).
183. H. Zhu and R. S. Averback, *Philos. Mag. Lett.* 73, 27 (1996).
184. See for instance D. Frenkel and B. Smit "Understanding Molecular Simulation." Academic Press, San Diego, 1996; M. P. Allen and D. J. Tildesley, "Computer Simulation of Liquids." Clarendon, Oxford, 1987.
185. W. D. Luedtke and U. Landman, *Phys. Rev. Lett.* 73, 569 (1994).
186. M. Hou, *Nucl. Instrum. Methods B* 135, 501 (1998).
187. M. Dreschler, J. J. Métois, and J. C. Heyraud, *Surf. Sci.* 108, 549 (1981); J. J. Métois and J. C. Heyraud, *Thin Solid Films* 75, 1 (1981); C. R. Henry and M. Meunier, *Mater. Sci. Eng. A* 217/218, 239 (1996).
188. C. R. Stoldt, A. M. Cadilhe, C. J. Jenks, J.-M. Wen, J. W. Evans, and P. A. Thiel, *Phys. Rev. Lett.* 81, 2950 (1998).
189. P. Jensen, N. Combe, H. Larralde, J. L. Barrat, C. Misbah, and A. Pimpinelli, *Eurropean Phys. J. B,* in press.

190. W. Selke and P. M. Duxbury, *Z. Phys. B* 94, 311 (1994); E. Adam, A. Chame, F. Lancon, and J. Villain, *J. Phys. I France* 7, 1455 (1997).
191. C. Herring, *Phys. Rev.* 82, 87 (1951).
192. M. Drechsler et al., *J. Phys.* 50, Colloque C8, 223 (1989).
193. H. P. Bonzel and E. E. Latta, *Surf. Sci.* 76, 275 (1978).
194. G. Jeffers, M. A. Dubson, and P. M. Duxbury, *J. Appl. Phys.* 75, 5016 (1994).
195. J. Eggers, *Phys. Rev. Lett.* 80, 2634 (1998).
196. L. Lewis, P. Jensen, and J.-L. Barrat, *Phys. Rev. B* 56, 2248 (1997).
197. X. Yu and P. M. Duxbury, *Phys. Rev. B* 52, 2102 (1995).
198. H. Zhu and R. S. Averback, *Philos. Mag. Lett.* 73, 27 (1996).
199. J. J. Métois and J. C. Heyraud, *J. Crystal Growth* 57, 487 (1982).
200. P. Jensen et al., *European Phys. J. B* 11, 497 (1999).
201. N. Combe, P. Jensen, and A. Pimpinelli, *Phys. Rev. Lett.* 85, 110 (2000).
202. N. Combe and H. Larralde, *Phys. Rev. B* 62, 16074 (2000).
203. A. Pimpinelli, J. Villain, and D. E. Wolf, *J. Phys. I (France)* 3, 447 (1993); G. S. Bales and D. C. Chrzan, *Phys. Rev. Lett.* 74, 4879 (1995).
204. P. Jensen, unpublished.
205. J. L. Barrat, private communication.
206. G. Jeffers, M. A. Dubson, and P. M. Duxbury, *J. Appl. Phys.* 75, 5016 (1994).
207. J. Tuaillon, Ph.D. Thesis, Université de Lyon, 1995; J. Tuaillon et al., *Philos. Mag. A* 76, 493 (1997).
208. G. W. Nieman, J. R. Weertman, and R. W. Siegel, *J. Mater. Res.* 6, 1012 (1991).
209. H. Zhu and R. S. Averback, *Mater. Sci. Eng. A* 204, 96 (1995).
210. M. Celino, G. D'Agostino, and V. Rosato, *Mater. Sci. Eng. A* 204, 101 (1995); *Phys. Rev. B* 48, 22 (1993).
211. L. Bardotti, B. Prével, P. Mélinon, A. Perez, Q. Hou, and M. Hou, *Phys. Rev. B* 62, 2835 (2000); L. Bardotti, B. Prevel, M. Treilleux, P. Mélinon, and A. Perez, *Appl. Surf. Sci.* 164, 52 (2000).
212. "Biomimetic Materials Chemistry" (S. Mann, Ed.). VCH, New York, 1996.
213. S. Sun and C. B. Murray, *J. Appl. Phys.* 85, 4325 (1999).
214. K. Sattler, "Cluster Assembled Materials," Materials Science Forum, Vol. 232. Trans Tech, Aedermannsdorf, 1996.
215. C. Binns, *Surf. Sci. Rep.*, in press.
216. P. Mélinon, P. Keghelian, B. Prével, A. Perez, G. Guiraud, J. Le Brusq, J. Lermé, M. Pellarin, and M. Broyer, *J. Chem. Phys.* 107, 10278 (1997).
217. C. Ray, M. Pellarin, J. L. Lermé, J. L. Vialle, M. Broyer, X. Blase, P. Melinon, P. Kéghélian, and A. Perez, *Phys. Rev. Lett.* 80, 5365 (1998).
218. P. Melinon, P. Kéghélian, A. Perez, C. Ray, J. Lermé, M. Pellarin, M. Broyer, M. Boudeulle, B. Champagnon, and J. L. Rousset, *Phys. Rev. B* 58, 16481 (1998).
219. J. Tuaillon, V. Dupuis, P. Mélinon, B. Prével, M. Treilleux, A. Perez, M. Pellarin, J. L. Vialle, and M. Broyer, *Philos. Mag. A* 76, 493 (1997).
220. M. Negrier, J. Tuaillon-Combes, V. Dupuis, A. Perez, M. Pellarin, and M. Broyer, *European Phys. J. D* 9, 475 (2000).
221. B. Palpant, B. Prével, J. Lermé, E. Cottancin, M. Pellarin, M. Treilleux, A. Perez, J. L. Vialle, and M. Broyer, *Phys. Rev. B* 57, 1963 (1998).
222. J. Lermé, B. Palpant, B. Prevel, M. Pellarin, M. Treilleux, J. L. Vialle, A. Perez, and M. Broyer, *Phys. Rev. Lett.* 80, 5105 (1998).
223. J. Lermé, B. Palpant, B. Prevel, E. Cottancin, M. Pellarin, M. Treilleux, J. L. Vialle, A. Perez, and M. Broyer, *European. Phys. J. D* 4, 95 (1998).
224. U. Kreibig and M. Vollmer, "Optical Properties of Metal Clusters." Springer-Verlag, Berlin, 1995.
225. V. V. Kresin, *Phys. Rep.* 220, 1 (1992).
226. J. Tiggesbaümker, L. Köller, K. H. Meiwes-Broer, and A. Liebsch, *Phys. Rev. A* 48, R1749 (1993).
227. M. Lindinger, K. Dasgupta, G. Dietrich, S. Krückeberg, S. Kuznetsov, K. Lützenkirchen, L. Schweikhard, C. Walther, and J. Ziegler, *Z. Phys. D* 40, 347 (1997).
228. A. Henglein and M. Giersig, *J. Phys. Chem.* 98, 6931 (1994).
229. L. M. Liz-Marzan and A. P. Philipse, *J. Phys. Chem.* 99, 15120 (1995).
230. M. Jamet, V. Dupuis, P. Mélinon, G. Guiraud, A. Perez, W. Wernsdorfer, A. Traverse, and B. Baguenard, *Phys. Rev. B* 62, 493 (2000).
231. W. Wernsdorfer, K. Hasselbach, A. Benoit, D. Mailly, J. Tuaillon, J. P. Perez, V. Dupuis, J. P. Dupin, G. Guiraud, and A. Perez, *J. Appl. Phys.* 78, 7192 (1995).
232. M. Jamet, V. Dupuis, C. Thirion, W. Wernsdorfer, P. Mélinon, and A. Perez, "Proc. 5th Int. Conf. on Nanostructured Materials," *Scripta Mater.*, in press.
233. J. L. Rousset, A. Renouprez, and A. M. Cadrot, *Phys. Rev. B* 58, 2150 (1998).
234. S. Link, Z. L. Wang, and M. A. El-Sayed, *J. Phys. Chem.* 103, 3529 (1999).
235. G. C. Papavassiliou, *J. Phys. F* 6, L103 (1976).
236. J. Sinzig, U. Radtke, M. Quinten, and U. Kreibig, *Z. Phys. D* 26, 242 (1993).
237. B. K. Teo, K. Keating, and Y. H. Kao, *J. Amer. Chem. Soc.* 109, 3494 (1987).
238. E. Cottancin, J. Lermé, M. Gaudry, B. Prével, M. Treilleux, M. Pellarin, M. Broyer, and P. Mélinon, *Phys. Rev. B* 62, 5179 (2000).
239. J. Lermé, B. Palpant, E. Cottancin, M. Pellarin, B. Prével, J. L. Vialle, and M. Broyer, *Phys. Rev. B* 60, 16151 (1999).
240. A. Liebsch, *Phys. Rev. B* 4, 11317 (1993).
241. N. Del Fatti, C. Voisin, M. Achermann, S. Tzortzakis, D. Christophilos, and F. Vallée, *Phys. Rev. B* 61, 16956 (2000).
242. C. Voisin, N. Del Fatti, D. Christofilos, and F. Vallée, *J. Phys. Chem B*, in press.
243. C. Voisin, D. Christofilos, N. Del Fatti, F. Vallée, B. Prével, E. Cottancin, J. Lermé, M. Pellarin, and M. Broyer, *Phys. Rev. Lett.* 85, 2200 (2000).
244. S. Sun, C. B. Murray, D. Weller, L. Folks, and A. Moser, *Science* 287, 1989 (2000).
245. W. Wernsdorfer, Magnetism of nanometer-sized particles and clusters in "Metal Clusters at Surfaces: Structure, Quantum Properties, Physical Chemistry." (K. H. Meiwes-Broer, Ed.), Springer Series in Cluster Physics, pp. 211–236. Springer-Verlag, Berlin, 2000.
246. D. J. Sellmyer, M. Yu, and R. D. Kirby, *Nanostruct. Mater.* 12, 1021 (1999).
247. A. Thiaville, *Phys. Rev. B* 61, 12221 (2000).
248. M. Jamet, M. Négrier, V. Dupuis, J. Tuaillon-Combes, P. Mélinon, A. Pérez, W. Wernsdorfer, B. Barbara, J. Voguel, and B. Baguenard, submitted for publication.
249. M. Negrier, Ph.D. Thesis, University Claude Bernard Lyon 1, France, 2000.
250. For an overview see, *Mater. Res. Soc. Bull.* 22, 19 (1997).
251. H. W. Kroto, J. E. Fischer, and D. E. Cox, "The Fullerenes." Pergamon Press, Oxford, 1993.
252. M. Pellarin, C. Ray, J. Lermé, J. L. Vialle, M. Broyer, X. Blase, P. Kéghélian, P. Mélinon, and A. Perez, *J. Chem. Phys.* 110, 6927 (1999).
253. F. Bechstedt, *Phys. Status Solidi B* 112, 9 (1982) and references therein.